I. ISOLATION OF *LAC* OPERATOR DNA

II. XPS INVESTIGATION OF THE GaAs/NATIVE OXIDE AND Si/METAL INTERFACES

Thesis by

Paula J. Grunthaner

In Partial Fulfillment of the Requirements

for the Degree

Master of Science

1980

California Institute of Technology

Pasadena, California

(submitted February 15, 1980)

TABLE OF CONTENTS

ABSTRACT

Chapter I

A procedure is presented for the large scale isolation of cloned 29 base-pair *lac* operator DNA from plasmid DNA. The methodology is general and may be used to isolate other cloned DNA fragments as well.

Initial ultraviolet difference experiments with *lac* repressor protein are also presented. Solvent perturbation is used to locate the tyrosine and tryptophan residues.

Chapter II

The chemical structure of the thin native oxide of GaAs (30 - 40 Å) has been investigated using x-ray photoelectron spectroscopy. Both wet chemical and argon ion bombardment techniques have been used to depth profile the oxide structure. The composition of the oxide is found to be quite complex and the distribution of the various species as a function of oxide thickness is discussed.

A Fouries transform data reduction technique based on linear prediction has been used to develop possible explanations for the experimentally observed chemical shifts and composition layers. Evidence is found for the presence of As_2O_3, Ga_2O_3, and the mixed oxide $GaAsO_4$.

Chapter III

A systematic investigation of the bonding properties of selected transition metal silicides on single crystal Si substrates is proposed. $^4He^+$ backscattering, XPS, and x-ray excited AES will be used to characterize both the bulk and interfacial bonding properties. Initial experiments are presented to demonstrate the feasibility of the approach.

ACKNOWLEDGMENTS

I wish to thank Professor Richard E. Dickerson for his support and guidance throughout the course of the work reported in Chapter I. Special thanks also go to Art Riggs, John Rosenberg, Richard Scheller, Mary Kopka, and Olga Kallai for their thoughtful advice and contributions.

The work reported in chapters II and III was performed at the Jet Propulsion Laboratory, Pasadena, California. The patient support of the JPL management and scientists is very gratefully acknowledged. In particular, I owe a debt of gratitude to the following people:

Rick Vasquez-- for his many contributions to the GaAs/oxide study.

John Barton and Jeff Klein-- for their development of the Fourier techniques used in Chapter II.

Jim Wurzbach, Blair Lewis, and Joe Maserjian-- for many helpful technical discussions.

Chuck Zachman, Frank Lombardi, and Malcolm Rayfield-- for their excellent technical assistance.

My husband, Frank- for his support, encouragement, and patience through it all.

A very special thanks goes to Professor James W. Mayer for his guidance, enthusiam, and creative ideas throughout the work reported in chapter III.

To Mom and Dad, who made it all possible....

I. ISOLATION OF *LAC* OPERATOR DNA

ISOLATION OF LAC OPERATOR DNA

ABSTRACT

A procedure is presented for the large scale isolation of cloned 29 base-pair *lac* operator DNA from plasmid DNA. The methodology is general and may be used to isolate other cloned DNA fragments as well.

Initial ultraviolet difference experiments with *lac* repressor protein are also presented. Solvent perturbation is used to locate the tyrosine and tryptophan residues. The results suggest that many of the UV difference studies concerned with the conformational changes of repressor need to be reexamined.

INTRODUCTION

A fundamental mechanism for the control of gene expression depends on the interaction between protein molecules with specific regions of DNA. The recognition of this molecular basis for the control of enzyme activity and regulation of protein and nucleic acid synthesis is perhaps the greatest milestone in modern biology. One particular class of the regulatory proteins known as *repressors* inhibits gene transcription by binding to specific DNA regions called *operators*. The existence of repressor proteins was first hypothesized by Jacques Monod and Francois Jacob in 1961[1] and since this time a variety of repressors have been demonstrated *in vitro*.

The molecular basis of gene regulation is best understood for the case of the lactose operon of *Escherichia coli*. The *lac* operon consists of a cluster of three genes which code for the enzymes necessary for the fermentation of lactose. The genetic map of this operon in shown in figure 1. The structural *z* gene codes for the enzyme β-galactosidase, which is responsible for the cleavage of lactose into galactose and glucose. The *y* gene codes for the synthesis of a membrane permease which directs the transport of lactose into the cell. The third *a* gene is responsible for the synthesis of thiogalactoside transacetylase, which has no

known role in lactose metabolism. These three structural genes are classified as an operon because they are transcribed into a single polycistronic messenger RNA (mRNA).

The Lac Control Region

The synthesis of the *lac* repressor protein is coded by the structural *i* gene. In its active form, repressor controls the production of the enzymes described above by binding to the operator region of the *lac* operon. This blocks the transcription of the genes into mRNA. The repressor may be inactivated by a variety of small molecules known as inducers. These molecules bind reversibly to the repressor protein and decrease its binding affinity for DNA by inducing a conformational change in the protein. In the presence of the inducers, repressor "falls off" the DNA, allowing transcription of the *lac* operon. These inducers are by-products of lactose fermentation and therefore establish a feed-back loop for the production of the necessary enzymes. After the lactose supply has been exhausted, the repressor is freed of its sugar inducer and it once again binds to the operator DNA to prevent the genes from being transcribed.

Though it has been determined that the repressor protein physically binds to the DNA operator site, little is known about the detailed mechanisms of the binding. Understanding how the repressor (150,000 molecular weight) selects and binds to the ~25 base pair operator region out of the 10^6 base pairs of *E. coli* DNA is of fundamental importance. Equally important is understanding how the induced conformational changes of the repressor affect its ability to recognize and bind to this region of DNA. Answers to these fundamental questions will help to elucidate the basic mechanisms of gene control at the molecular level.

Unfortunately, physical chemical studies of the details of the repressor-operator interaction have been hampered by inadequate supplies of operator DNA. Moreover, most operator containing DNA is not suitable for spectroscopic studies because of interferences from the unavoidably large excess of non-operator DNA. For example, in λplac DNA (from a phage carrying the *E. coli lac* operon), the *lac* operator region constitutes only 0.042% of the total DNA. Physical studies are simply not possible with this concentration.

LARGE SCALE DNA ISOLATION

The recent advances in molecular biology and synthetic chemistry have reversed this situation by providing the means to obtain large amounts of small DNA fragments by cloning techniques. To clone the operator DNA segment, a chemically synthesized octanucleotide containing the recognition site for *Eco* RI endonuclease was ligated to each end of a synthetic *lac* operator sequence.[2] The resulting RI-operator DNA fragment was inserted into the pMB9 plasmid to produce an easily excisable DNA fragment. This plasmid provides a convenient source of *lac* operator DNA fragments since *E. coli* bacteria containing the RI-operator plasmids can be inexpensively grown in large quantities and the operator DNA excised.

In principle, any quantity of pure operator DNA may be isolated in this manner. Methods for the isolation of plasmid DNA exist for small preparations from ∿1 gram bacterial paste. Spectroscopic studies of operator-repressor interactions, however, will require several milligrams of operator DNA. This corresponds to approximately one kilogram of cell paste with the currently available strains. A direct scale up by three orders of magnitude of the existing isolation procedures is not possible since volumes become impossibly large for existing equipment. The development of a procedure for large scale isolation of small fragment DNA is necessary.

The DNA isolation procedure reported here is the result of an ∿8 month effort to develop large scale procedures for the isolation of plasmid DNA and excision of the operator DNA segment. An outline of the procedure is as follows:

Detergent Lysis
↓
Centrifugation
↓
Removal of RNA
↓
Removal of Proteins
↓
DNA Precipitation
↓
A50 Gel Filtration
↓

Pressure Dialysis
↓
Endonuclease Treatment
^{32}P labeling of DNA
↓
A50 Gel Filtration
↓
Lyophilization
↓
Sephadex G-100 Gel Filtration

The method is general and may be used to isolate other excisably cloned DNA fragments as well. Approximately 1-2 months are required to grow and process one kilogram of cells. The details of the procedure are presented below.

Amplification of Plasmid DNA

A bacterial strain containing the RI-operator pMB9 plasmid was grown in M9 medium[3] supplemented with L-proline, L-leucine, and thiamine (2×10^{-4} M). An overnight five liter started culture also in M9 medium was used to innoculate a 350 liter fermenter culture. At a culture density of $\sim 10^8$ cells/ml, chloroamphenicol was added to a concentration of 250 μg/ml. Incubation was continued at 37°C with vigorous aeration for ~24 hours. During the incubation period in the antibiotic chloramphenicol, the chromosomal DNA does not replicate, but the plasmid DNA is amplified to yield several thousand copies per cell. The cells were harvested by centrifugation and stored at -20°C. The typical yield obtained was 750-800 grams of cell paste.

Cell Lysis

Cells were lysed in units of 90 grams for convenience. The cells were carefully resuspended in 500 ml of cold Tris-sucrose solution (0.05 M Tris-HCl, pH 8.0, 25% sucrose). After complete resuspension (cell clumps will not lyse efficiently), 100 ml of 5 mg/ml hen egg white lysozyme in 0.250 M Tris-HCl, pH 8.0, was added. The suspension was left on ice for 5 minutes. 50 ml of 0.250 M EDTA (ethylene diamine tetraacetic acid), pH 8.0, was then added and the mixture allowed to sit on ice an additional 5 minutes. 500 ml of Triton lytic mix (15 ml Triton X100; 375 ml 0.250 M EDTA, pH 8.0; 75 ml 1 M Tris-HCl, pH 8.0; 35 ml H_2O) was added and the now extremely viscous suspension was mixed gently to avoid any shearing of the DNA. The suspension was kept on ice for 30

minutes to insure complete lysis.

Centrifugation

After the cell lysis was completed, the suspension was transfered to a Type 19 (Beckman) rotor and centrifuged at 19,000 rpm at 4°C for 3-5 hours. Approximately 1100 ml of cleared supernatant was obtained. At this stage, the lysate should contain the RI-operatore pMB9 plasmid DNA, RNA, chromosomal DNA, proteins, and various cellular components. The pellet resulting from the centrifugation was discarded as it contains unlysed cells, cell walls, and nucleoprotein complexes.

RNase Treatment

In earlier attempts to isolate the plasmid DNA, we found the extreme viscosity of the lysate was the greatest contributor to most of the difficulties encountered in the various purification steps. This viscosity was attributed to a large amount of RNA being present in the cleared lysate. To denature and eliminate the RNA, the lysate was treated with RNase at this stage in the purification. 10 mg/ml RNase in 0.050 M NaOAc, pH 4.8, was boiled for 2 minutes to removed any DNase activity. This was then added to the cleared lysate to a final concentration of 0.050 mg/ml.

Phenol Extraction

An extraction with buffered phenol was used to separate the various proteins from the nucleic acids. Phenol crystals were liquified by adding 8% H_2O and then buffered by extracting three times with 0.050 M Tris-HCl, pH 8.0, 0.1 M NaCl, 0.02% sodium azide. The buffering step is necessary since acid pH degrades DNA. The DNA in the cleared lysate was then extracted twice with equal volumes of the buffered phenol. The aqueous phase containing the nucleic acids was separated from the phenol phase with a GS-3 rotor for 10 minutes at 5000 rpm.

Ethanol Precipitation

NaCl was added to the aqueous phase from the phenol extraction to a final concentration of 0.2 M. A two-fold volume of cold ethanol was added and the suspension stored overnight in a refrigerator. The resulting white precipitate, which contains the RI-operator plasmid DNA, chromosomal DNA, Triton X100, and degraded RNA, was collected by centrifugation in a GS-3 rotor at 5000 rpm for one hour at $4^{o}C$. The pellet obtained was resuspended in the minimum required volume of cold 0.05 M Tris-HCl, pH 7.5. NaCl and NaN_3 were added to 0.1 M and 0.02%, respectively.

A50 Gel Filtration

The DNA solution was applied to an A50 agarose (BioRad) column (10 X 70 cm) that had been equilibrated with 0.05 M Tris-HCl, pH 7.6, 0.1 M NaCl, 0.02% NaN_3. The DNA was eluded with the same buffer at a flow rate of ∿5 ml/minute. Absorbtion of the effluent at 260 nm was monitored and the elution profile is shown in figure 2. The RI-operator plasmid DNA and chromosomal DNA elute in the exclusion volume (peak I), while the degraded RNA, Triton X100, phenol, and various other small cellular components are retained by the agarose network (peak II). A small aliquot was removed from the DNA elution peak and set aside for later 5' terminal end labeling with ATP^{32}.

Pressure Dialysis

The DNA fractions obtained from the above procedure were combined to yield ∿1750 ml. This volume was concentrated to a more manageable volume of 185 ml using an Amicon pressure dialysis apparatus with membrane type pM-30.

Isolation of 5' ^{32}P-labeled Operator DNA

At this point, the DNA solution is pure enough to digest with *Eco* RI endonuclease to remove the operator segment from the plasmid DNA. However, because the operator DNA fragment is only 29 base pairs in length, the DNA concentration in later purification steps will be too dilute to detect with optical absorbance.

Thus, the small aliquot set aside above was digested with *Eco* RI endonuclease and the resulting operator fragments were labeled with $AT^{32}P$. This 5' ^{32}P-labeled operator DNA is to be used as a "spike" for locating the remaining operator fragments in later purification steps. The endonuclease digestion and subsequent labelling procedures are detailed below.

500 µl of the DNA solution (containing ∿175 µg DNA as determined by its optical density) was dialyzed against a solution of 0.1 M Tris-HCl, pH 7.5, 0.005 M $MgCl_2$, 0.1 M NaCl. 2 µl of *Eco* RI endonuclease was added (the enzyme as well as the assay of its activity was kindly supplied by A. Riggs, City of Hope) and the solution was placed in a 37°C H_2O bath for 2½ hours. Immediately thereafter, the DNA fragments were concentrated by precipitation in cold isopropanol. The precipitate was redissolved in 50 µl of 0.05 M Tris-HCl, pH 7.6.

30 µl of the *Eco* RI endonuclease digested fragments were forced over chellex with 0.05 M Tris-HCl, pH 7.6. The DNA was reprecipitated by the addition of a two-fold volume of cold ethanol. Complete precipitation was insured by cooling the solution to -70°C for 10 minutes. The DNA precipitate was collected by centrifugation at 10,000 rpm for 30 minutes in a SM34 rotor at 4°C. The ethanol was decanted off and the excess ethanol was removed with a mechanical pump. The precipitate was redissolved in 100 µl 0.010 M Tris-HCl, pH 8. The DNA was then treated with Bovine alkaline phosphatase for 30 minutes at 37°C. The enzyme was extracted from the solution with 24:1 chloroform : iso-amyl alcohol. The DNA was once more precipitated with ethanol as described above and finally redissolved in 75 µl of 0.1 M glycine-NaOH, pH 9.5, 0.010 M spermadine, 0.001 M EDTA. The solution was heated to 100°C for 3 minutes and then chilled in ice water. 10 µl of 0.5 M glycine-NaOH, pH 9.5, 0.1 M $MgCl_2$, and 0.05 M DTT was added followed by 5 µl of $AT^{32}P$ (0.57 µmoles/ml, 114.6 Ci/mole) and 2 µl Kinase. The Kinase and its activity assay was kindly provided by A. Riggs, City of Hope.

The 5' ^{32}P-labeled DNA was collected via ethanol precipitation and redissolved in 300 µl 0.05 M Tris-HCl, pH 7.6. Excess $AT^{32}P$ was separated from the labeled DNA with a G75 gel fitration column. The DNA collected in the G75

exclusion volume was flash evaporated to concentrate. The ^{32}P-operator DNA fragment was separated from ^{32}P-plasmid fragments with a Sepharose 2B-300 column. 0.1 M triethylamine carbonate, pH 8, was used as the running buffer. The elution progress was monitored via a scintillation counter. The pure ^{32}P-operator DNA obtained from this procedure is used as a "spike" to follow the remaining operator DNA below.

Isolation of the Remaining Operator DNA

The 185 ml of DNA solution obtained after the pressure dialysis step was dialyzed against 0.1 M Tris-HCl, pH 7.5, 0.005 M $MgCl_2$, 0.1 M NaCl. Triton X100 was added to 0.02%. 400 µl of *Eco* RI endonuclease (1 µl will digest ∿1 mg of the plasmid DNA) was added and the solution maintained at 37°C for 5 hours. The ^{32}P-labeled operator obtained in the previous section was then added and the entire solution loaded onto an A50 agarose column with a running buffer of 0.01 M Tris-HCl, pH 7.5, 0.01 M NaCl. The elution was followed both by optical absorbtion at 260 nm and by scintillation counter. The profile obtained is shown in figure 3. The large plasmid DNA fragments elute in the exclusion volume while the operator DNA is retarded by the agarose network. The volumes containing the operator DNA were combined and lyophilyzed to concentrate. The solution was loaded onto a Sephadex G-100 (fractionation range 4,000 - 150,000 MW) as a final purification step with a running buffer of 0.01 M Tris-HCl, pH 7.5, 0.010 M NaCl, 0.1 mM EDTA. The elution diagram is shown in figure 4. The operator DNA was found to be present in peak I, as determined by its absorbtion characteristics at 260, 280, and 230 nm. Peak II was determined to be primarily Triton X100. Peak I volumes were combined and stored at -20°C for later activity assays and experiments.

COMPETITION EXPERIMENTS

In order to verify that the isolated DNA contains a functional *lac* operator site, equilibrium experiments were performed. The competition assay is based on the fact that DNA containing a repressor-operator complex is retained by nitrocellulose filters, whereas DNA free of protein is not. The membrane filter technique has been shown to be an extremely sensitive assay for repressor-operator complexes, allowing the detection of less than 10^{-16} mole of the

complex.[4-6] Most importantly, extensive studies have shown that the filter technique does not perturb the reaction equilibrium, which allows one to calculate binding constants if desired.[7]

The competition experiments for assaying DNA functionality were performed by mixing varying amounts of the isolated operator DNA with 0.05 μg ^{3}H-labeled λplac (an operator containing DNA). Repressor protein was then added to be approximately equimolar with the operator concentration (3.4×10^{-12} M). Final reaction volumes were held constant at 400 μl. After one hour of incubation at 25°C, 500 μl samples were filtered through nitrocellulose in duplicate. Filters were counted for ^{3}H in a scintillation counter. This directly measures the concentration of repressor-^{3}H λplac DNA complex in solution.

Figure 5 displays the competition curve that was obtained. Clearly the isolated DNA completes with the ^{3}H λplac for the repressor protein. In the presence of isopropylthiogalactoside (IPTG), a known inducer of the *lac* operon, the binding of repressor to DNA is eliminated. The lack of competition observed when RV180wt DNA (a non-operator containing DNA) is mixed with the ^{3}H λplac eliminates the possibility that non-specific binding of repressor to the isolated DNA is responsible for the observed competition.

From figure 5, 2×10^{-3} μg/ml of the isolated operator DNA is required to reduce the fraction of operator saturation to 50%. Using the established procedure for calculating binding constants for repressor binding to DNA,[8] it is found that the affinity of the isolated 29 base pair operator DNA for repressor is on the order of 10^{10} M^{-1}. This affinity is several orders of magnitude less than the affinity of natural operator for repressor. This is not unexpected for several reasons. Most association and dissociation rate calculations for repressor binding to the natural operator suggest that non-specific binding to the DNA adjacent to the operator site is responsible for at least a 10-fold increase in the association rate.[9-10] Without the adjacent DNA, the dissociation rate is expected to be faster in addition. Moreover, the binding affinity of repressor for synthetic 21 base pair operator DNA was found to be approximately 10^{10} M^{-1}.[11]

This observation of a binding affinity of 10^{10} M^{-1} for the binding of repressor to the 29 base pair operator DNA, along with the inducing affect of IPTG on the equilibrium competition curve, firmly demonstrates that functional *lac* operator has been isolated.

UV DIFFERENCE EXPERIMENTS WITH REPRESSOR

Solvent perturbation difference spectroscopy was used to locate the tyrosine and tryptophan amino acid residues in the repressor protein. Ultimately, this technique was to be expanded to investigate the conformational changes of repressor that occur upon binding to operator DNA. This project was terminated before the expanded investigation was begun. Nevertheless, the initial study of the location of the chromophoric residues of repressor will be reported here since the results disagree with the values in the literature and suggest that many of the UV difference studies concerned with conformational changes of *lac* repressor need to be reexamined.

Solvent Perturbation Method

The ultraviolet absorption spectrum of a protein in the 250-300 mμ region is due almost entirely to the aromatic amino acid side chains tyrosine and tryptophan. The wavelength of maximum absorption and the molar absorptivity of these residues are sensitive to changes in environment. This may be utilized to gain information concerning their location in the protein by using the solvent perturbation technique of difference spectroscopy. In this method, the UV absorbtion characteristics of the tyrosine and tryptophan residues on the surface of a protein are perturbed by changing the physical properties of the solvent. The chromophoric residues located in the interior of the protein will be shielded from these solvent effects. The fraction of exposed residues can be determined by comparing the spectral shift produced by a given perturbant to the total spectral shift produced by the same perturbant with the fully exposed protein. The major assumption in this technique is that the perturbant does not alter the conformation of the protein under investigation. In this study, glycerol was

used as the perturbant since it has been demonstrated that it will stabilize the native conformation of proteins.[12]

Experimental

All spectra were obtained on a Cary 17 spectrophotometer. Matched tandem double-compartment cells were used to correct for solvent absorbance and reflectance. The matched cells were checked with a tryptophan solution of absorbancy of 2-3 and found to produce deviations from the baseline less than ±0.001 absorbance units.

Lac repressor protein isolated from the *E. coli* strain M96 was obtained from R. E. Dickerson. The activity of the repressor was measured by a membrane filtration technique[7] using the procedure of Lin and Riggs.[8] It was found to be 100% ±10% active.

Spectral measurements were made by running a 50:50 mixture of repressor (or model compound) and 40% glycerol in both compartments of one tandem cell in the sample beam of the spectrometer. This was run against the unmixed repressor (or model compound) and glycerol in the reference beam. Strict volumetric manipulations were used in all solution preparations.

Results and Discussion

The ultraviolet difference spectrum of repressor in the presence of glycerol is shown in figure 6. There are several methods for determining the fraction of exposed tyrosines and tryptophans. One procedure is to compare the results to the perturbation spectrum of the totally denatured or unfolded protein. The advantage to this approach is that any possible perturbation of the side groups by the polypeptide chain itself is automatically taken into account. It has several disadvantages however: 1) one cannot be assured the protein is fully unfolded and 2) denatured proteins are generally not soluble in aqueous solutions.

A second approach, which is used in this study, involves the use of tyrosine and tryptophan model compounds to estimate the fraction of perturbed surface residues. This approach has been used successfully in solvent perturbation studies of several other protein systems.[13,14] In principle, since the character-

istic maxima of tryptophan compounds appear at 292-294 mμ and 281-284 mμ while the maxima of tryrosine compounds appear in the tryptophan trough at 286-288 mμ and at 278-281 mμ, one can estimate the number of exposed tyrosines and tryptophans by solving two simultaneous equations: [15]

$$\Delta\varepsilon_{286-288}(\text{protein}) = a \times \Delta\varepsilon_{286-288}(\text{tyr}) + b \times \Delta\varepsilon_{286-288}(\text{trp})$$

$$\Delta\varepsilon_{292-294}(\text{protein}) = a \times \Delta\varepsilon_{292-294}(\text{tyr}) + b \times \Delta\varepsilon_{292-294}(\text{trp})$$

Here $\Delta\varepsilon_{\lambda}$ is the experimentally determined molar absorbtivity differences in the model complexes and protein. In practice, however, a more reliable approach is to fit the observed protein spectrum with a combination of the tyrosine and tryptophan difference curves. This yields a more accurate estimation since the polypeptide backbone of the protein produces a slight red shift in the absorbtion of the residues. Thus, the model compound maxima need not correspond to the protein residue maxima. Using difference spectra from the model complexes N-acetyl-L-tyrosine ethyl ester and N-acetyl-L-tryptophanamide to fit the protein data by least squares, it was found that the perturbation spectrum of repressor could be approximated with ∿3 tyrosines and ∿1 tryptophan. The calculated curve is compared to the protein spectrum in figure 6. It should be emphasized that difference spectroscopy measures only the average exposure of residues.

These results disagree with the work of Mathews,[16] et.al, which concluded that 8 tyrosines and 1 tryptophan were exposed on the surface of repressor protein. Since the repressor monomer monomer contains a total of 8 tyrosines and 2 tryptophans, their value appears to be high. In addition, they report a DNA binding activity of only 10% for their repressor. These facts suggest that a large fraction of the protein used in their experiments was no longer in its native conformation and was possible denatured. The results reported here of 3 tyrosines and 1 tryptophan surface residues are more characteristic of values found for other high molecular weight proteins. Mathews, et.al, draw additional conclusions concerning conformational rearrangment of repressor upon inducer and anti-inducer binding based on changes in the aromatic residue surface exposure. In light of the results presented here, these experiments and conclusions need to be reexamined.

REFERENCES

1. Jacob, F., Monod, J., J. Mol. Biol. 3 (1961) 318
2. Heyneker, H.L., Shine, J., Goodman, H.M., Boyer, H.W., Rosenberg, J., Dickerson, R.E., Narang, S.A., Itakura, K., Lin, S., Riggs, A.D., Nature, 263 (1976) 748
3. Boyer, H., private communication
4. Riggs, A.D., Bourgeois, S., J. Mol. Biol., 34 (1968) 361
5. Riggs, A.D., Bourgeois, S., J. Mol. Biol., 53 (1970) 401
6. Riggs, A.D., Newby, R.F., Bourgeois, S., J. Mol. Biol., 51 (1970) 303
7. Riggs, A.D., Suzuki, H., Bourgeois, S., J. Mol. Biol., 48 (1970) 67
8. Lin, S., Riggs, A.D., J. Mol. Biol., 72 (1972) 671
9. Goad, W., Biophys. Soc. Abst., 12 (1972) 248a
10. Berg, O.G., Blomberg, C., Biophys. Chem, in press
11. Lin, S., Itakura, K., Rosenberg, J., Wilcox, G., Dickerson, R.E., Riggs, A.D., Molecular Mechanisms in the Control of Gene Expression, 17 (1976) 143
12. Simpson, R.B., Kauzmann, W., J. Am. Chem. Soc., 75 (1953) 5139
13. Donovan, J.W., Biochemistry, 3 (1964) 67
14. Williams, E. J., Herskovits, T.T., Laskowski, M., J. Biol. Chem., 240 (1965) 3574
15. Herskovits, T.T., in Methods in Enzymology, vol. XI, 749
16. Matthews, K.S., Matthews,H.R., Thielmann, H.W., Jardetzky, O., Biochem. Biophys. Acta., 295 (1973) 159

FIGURE CAPTIONS

Figure 1. Genetic map of the lac operon

Figure 2. Elution profile for the initial A50 agarose purification step. The absorbtion was monitored at 260 nm.

Figure 3. Elution profile for the second A50 agarose filtration. Left hand scale is absorbtion at 260 nm. Right hand scale is counts/min.

Figure 4. Final Sephadex G-100 elution profile. Operator DNA is located in peak I.

Figure 5. Equilibrium competition between the isolated 29 base-pair operator DNA and ^{3}H-labeled lambda plac DNA. The lambda plac DNA concentration was 0.125 μg/ml.

Figure 6. Solvent perturbation difference spectrum for repressor protein. 20% glycerol was used as the perturbant. The dashed curve is the calculated curve based on model complexes.

Figure 1

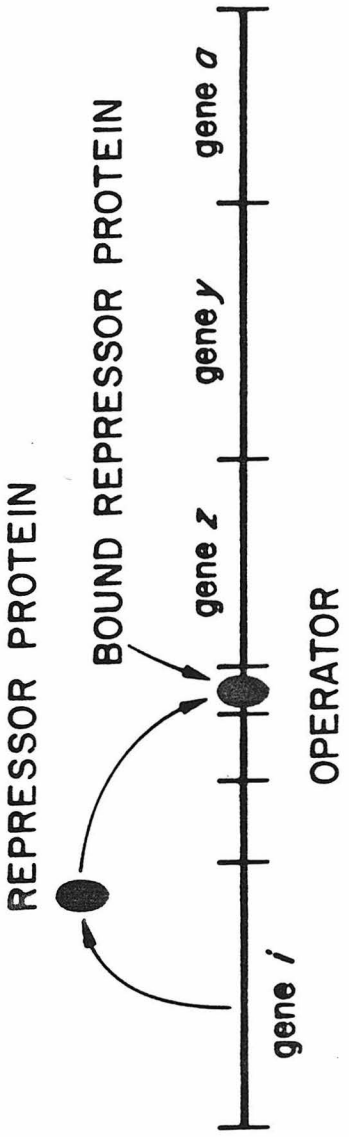
REPRESSOR PROTEIN
BOUND REPRESSOR PROTEIN
gene z
gene y
gene a
OPERATOR
gene i

Figure 2

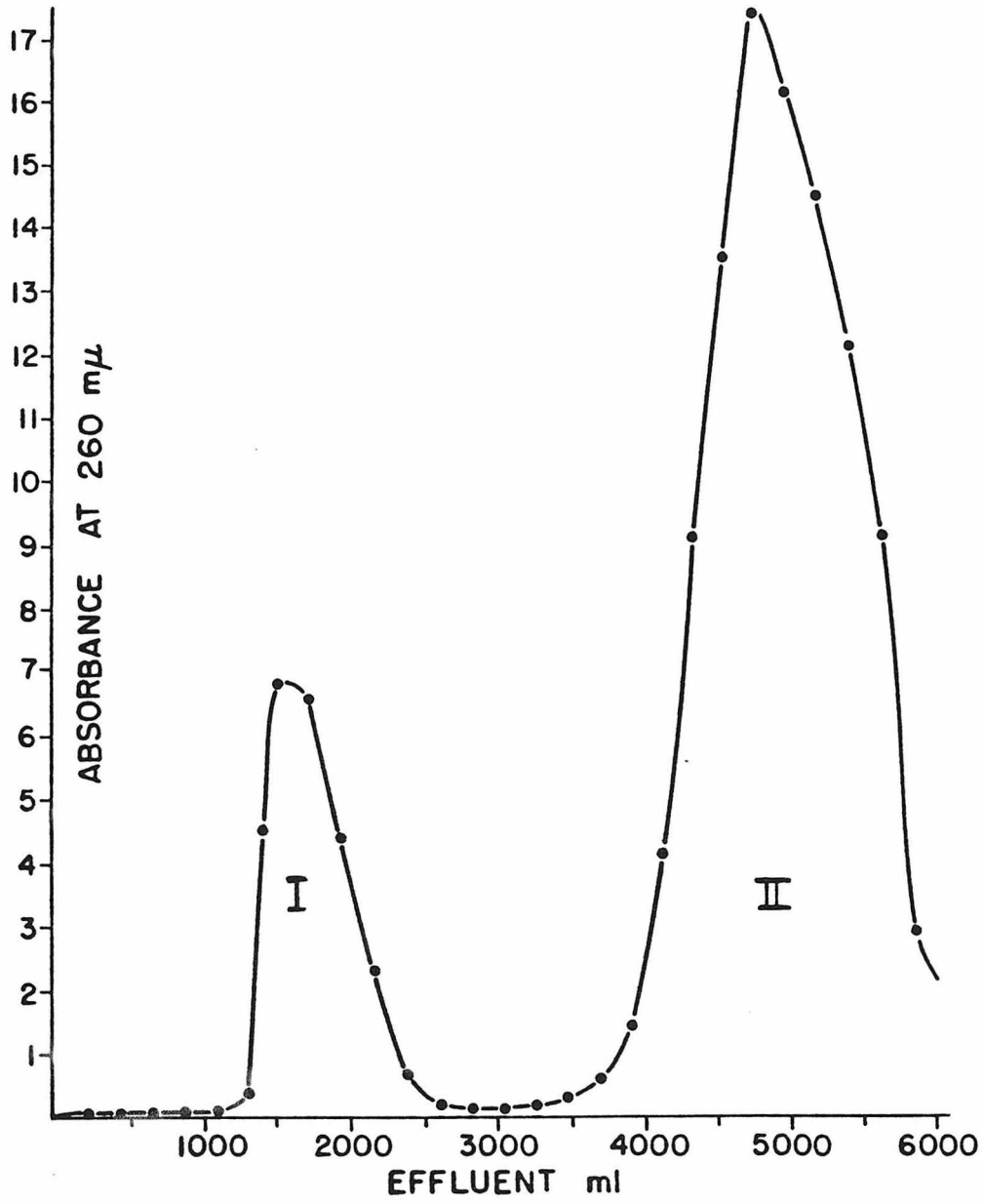
ABSORBANCE AT 260 mμ
17
16
15
14
13
12
11
10
9
8
7
6
5
4
3
2
1
I
II
1000
2000
3000
4000
5000
6000
EFFLUENT ml

Figure 3

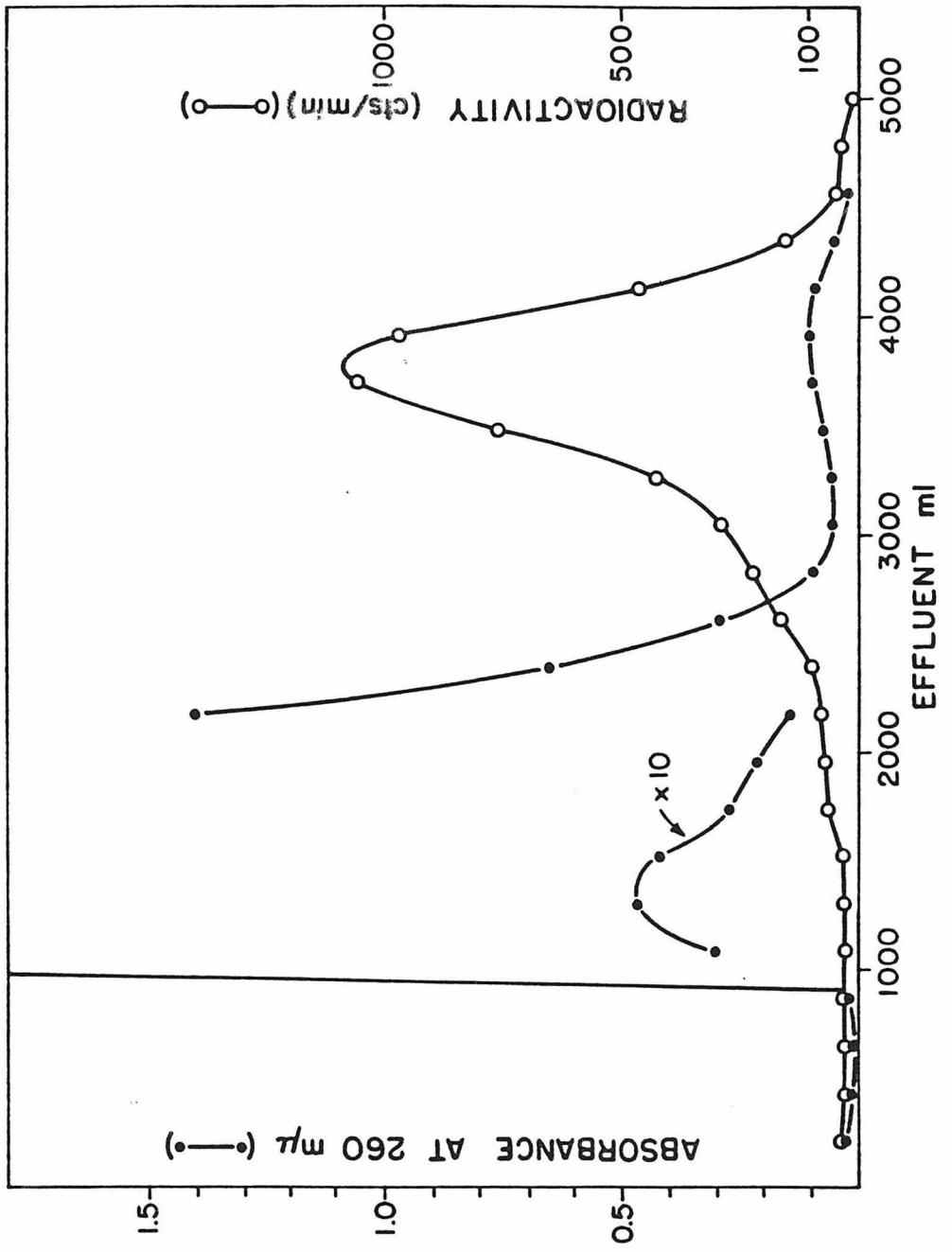
ABSORBANCE AT 260 mμ (•—•)
RADIOACTIVITY (cts/min)(o—o)
EFFLUENT ml
x10
1.5
1.0
0.5
1000
500
100
1000
2000
3000
4000
5000

Figure 4

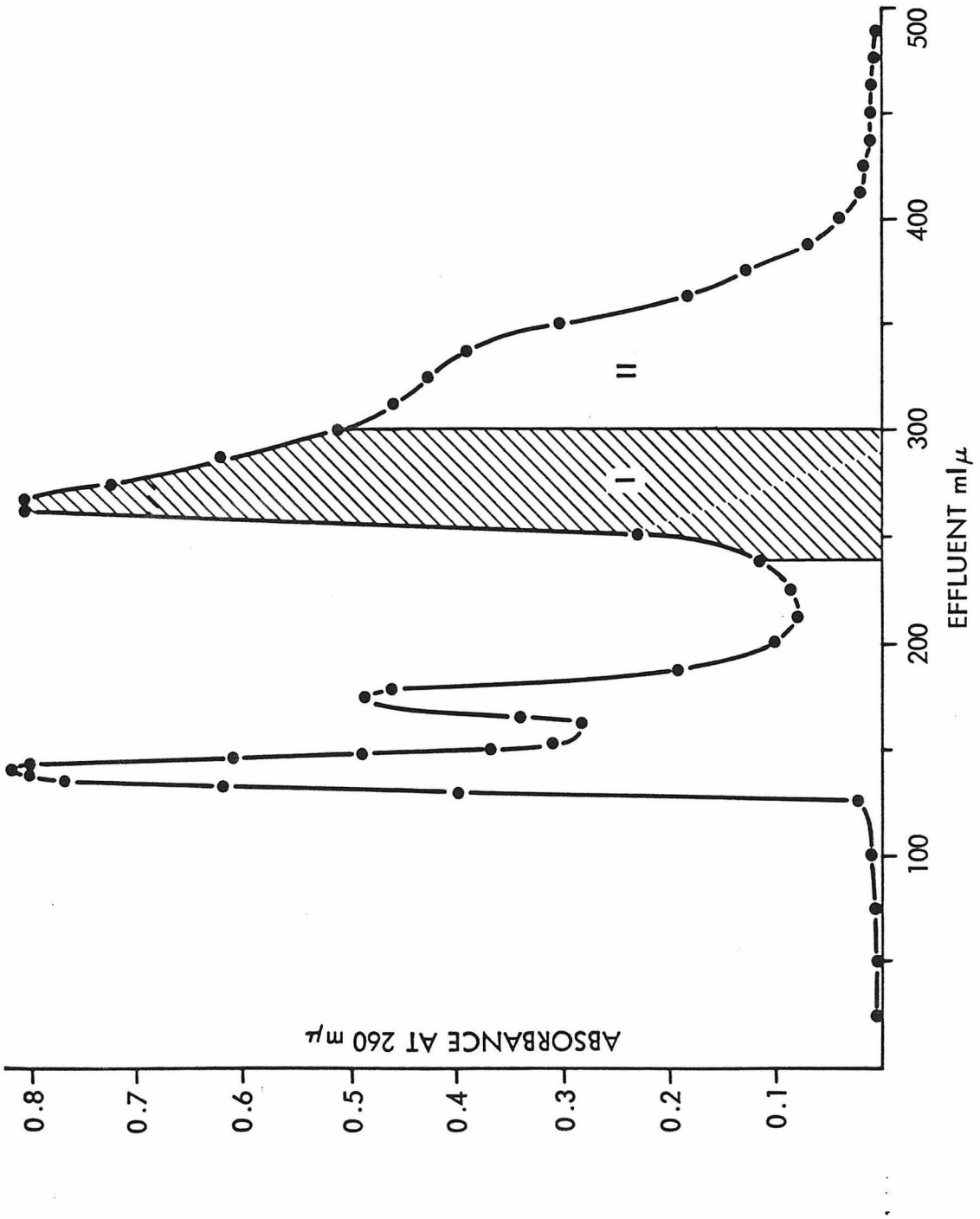
ABSORBANCE AT 260 mμ
0.8
0.7
0.6
0.5
0.4
0.3
0.2
0.1
100
200
300
400
500
EFFLUENT mlμ
I
II

Figure 5

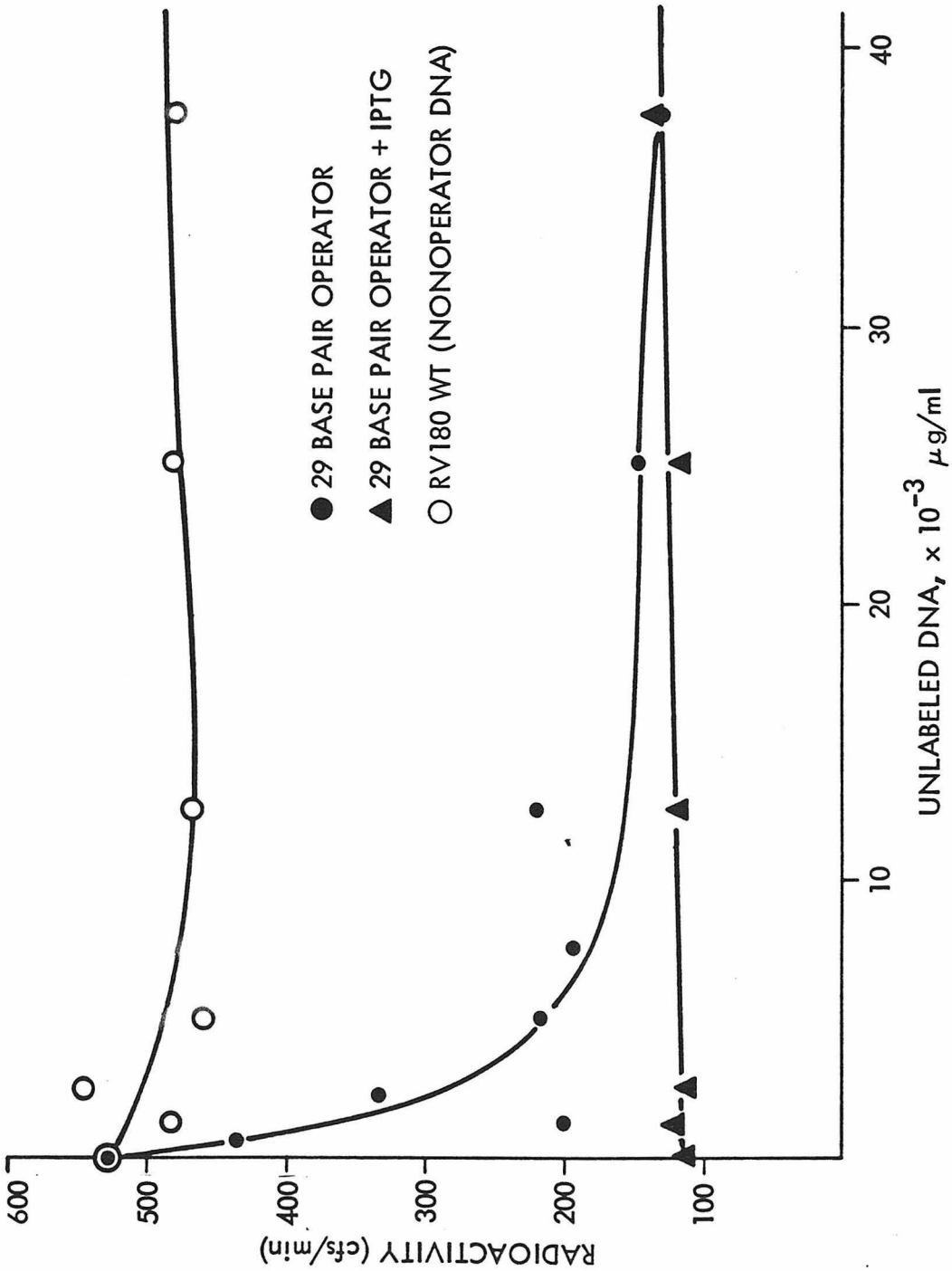
RADIOACTIVITY (cfs/min)
600
500
400
300
200
100
10
20
30
40
UNLABELED DNA, x 10^{-3} μg/ml
● 29 BASE PAIR OPERATOR
▲ 29 BASE PAIR OPERATOR + IPTG
○ RV180 WT (NONOPERATOR DNA)

Figure 6

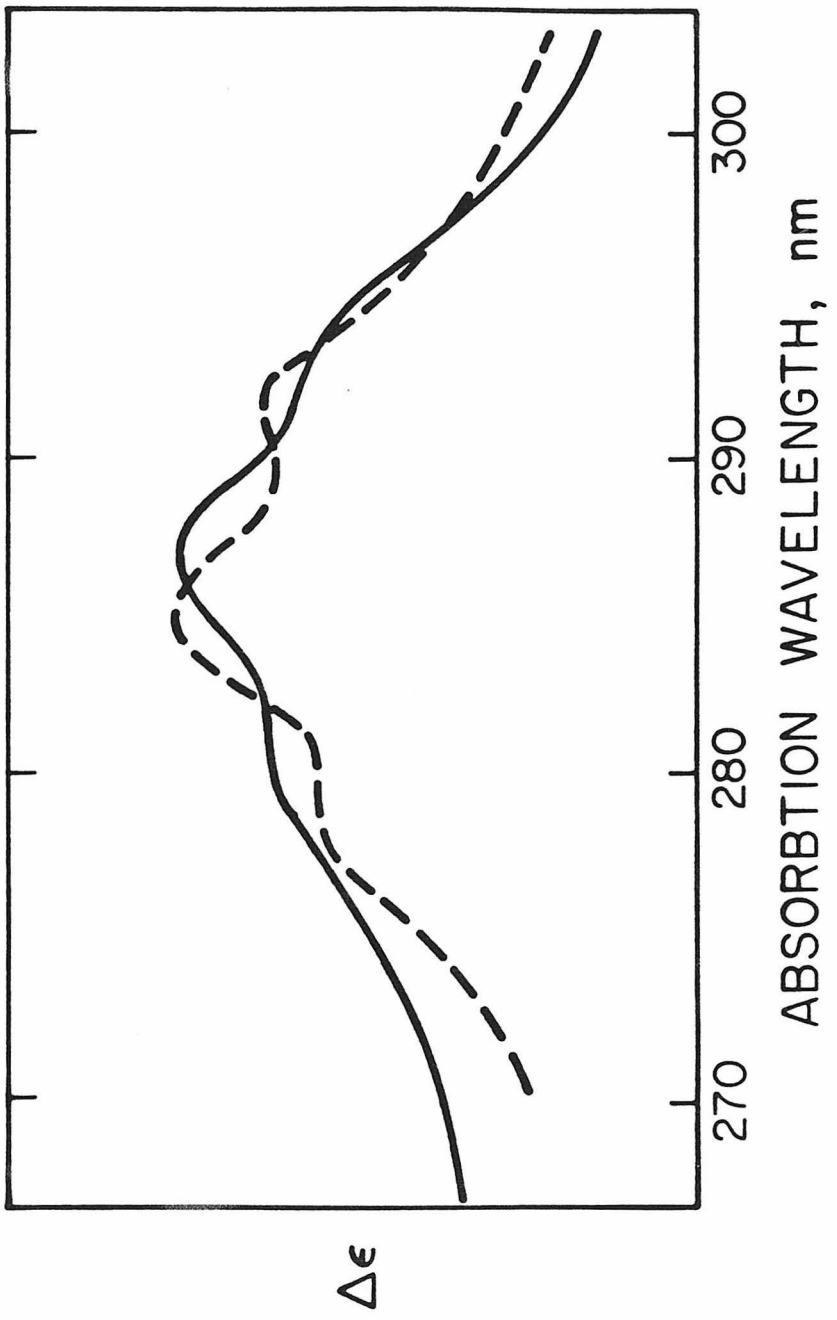

II. THE CHEMICAL NATURE OF THE NATIVE GaAs/OXIDE INTERFACE

THE CHEMICAL NATURE OF THE NATIVE GaAs/OXIDE INTERFACE

ABSTRACT

The chemical structure of the thin native oxide of GaAs (30-40 Å) has been investigated using x-ray photoelectron spectroscopy. Both wet chemical etchning and argon ion bombardment techniques have been used to depth profile the oxide structure. The composition of the oxide is found to be quite complex and the distribution of the various species as a function of oxide thickness is discussed.

A Fourier transform data reduction method based on linear prediction has been used to develop possible explanations for the experimentally observed chemical shifts and composition layers. The method is demonstrated with a test spectrum that illustrates its important features.

Evidence is found for the presence of As_2O_3, Ga_2O_3, and the mixed oxide $GaAsO_4$. Several additional species are found and their assignments discussed.

THE CHEMICAL NATURE OF THE NATIVE GaAs/OXIDE INTERFACE

I. INTRODUCTION

The ability to prepare reproducible, chemically stable dielectric films with highly uniform lateral composition on semiconductor surfaces is of fundamental importance in microelectronic technology. The phenomenal success of silicon device technology is due in large part to the ability to thermally grow high quality amorphous native oxides on the surface of silicon. For the III-V compound semiconductors, such adventitious oxides are generally not available because of the complexities introduced by the compound nature of the semiconductors and, hence, their varied surface chemistry. In the case of GaAs, early workers[1-5] found that high temperature thermal oxidation of GaAs resulted in porous, brittle, and polycrystalline films. Anodically grown oxides were shown to be amorphous, but nonuniform and inhomogeneous. More recently, various techniques based on chemical[6], galvanic[7,8], and plasma[9,10] oxidation in addition to the thermal[11-13] and anodic[14-19] oxidation have been attempted. A few of these methods appear promising, but much effort is still needed to improve the film properties. This will require more information regarding the nature of the oxidation reaction products formed during the growth of native oxides on compound semiconductors and their subsequent distribution in the oxide.

Several studies in the literature have examined the initial steps of oxidation on <110> GaAs by following the photoemission chemical shifts as a function of oxygen exposure. Such studies are important for understanding the fundamental nature of the initial oxidation of a compound semiconductor. However, because of the varied chemistry of As and Ga, these studies will not lend insight into the final equilibrium oxidation products or their distributions within the oxide. It is this final state which determines the utility of the oxide as a dielectric film for device technology.

The study presented here examines these final state oxidation products and their distribution in thin native oxides on GaAs using a chemical depth profiling method in conjunction with XPS. Extended room temperature oxidation conditions have been chosen to permit the native oxide to attain its equilibrium composition and structure. It is this equilibrium structure that is important to understand since with time all GaAs native oxides, regardless of the method of oxidation, will approach this state.

A. Experimental

The XPS experiments were performed using a modified HP 5950A ESCA spectrometer. The details of the spectrometer have been described elsewhere.[26] For these experiments, the spectrometer was operated at a resolution of ~0.35 eV FWHM and at channel sampling densities of 0.040 eV/channel. The analyzer pressure was typically less than 2×10^{-9} Torr. The S/N ratio of all data reported is greater than 200:1 as measured by the power spectral density of the Fourier transform. All deconvolutions reported were performed on data with a S/N ratio in excess of 800:1. All GaAs and GaAs/oxide spectra were recorded at 200K. This temperature is necessary to prevent desorption of the relatively volatile arsenic oxide. Elemental analysis of the samples was obtained by using a 0-1280 eV scan followed by close examination of the As 3d, Ga 3d, O 1s, C 1s, Ga_{LMM} and As_{LMM} photoemission lines.

All sample preparations were carried out in a high purity N_2 dry box connected to the spectrometer inlet port. This dry box, which is continually flushed with N_2 from a liquid source, typically operates at less than 5 ppm O_2 and 1-2 ppm H_2O. The furnace used for sample oxidations is connected via interlock to this N_2 dry box. Thus, all sample manipulations could be carried out without exposure to ambient contaminations.

<100> Te-doped samples grown by CVD on Czochralski substrates were used in all experiments. Samples were polished with Lustrox and cleaned in hot methanol with ultrasonic agitation, followed by 15 seconds in $NH_4OH : H_2O_2 : H_2O$ (10:1:1) and 60 seconds in $H_2SO_4 : H_2O_2 : H_2O$ (10:1:1).[27] Samples were given a final rinse in deionized H_2O, flow-dried with N_2 from a LN_2 source, and placed immediately in the N_2 dry box connected to the spectrometer. The samples were then cleaned with high purity ethanol using the spinning procedure described

below. Samples were finally etched with 100 μl 10:1 ethanol:HCl (transistor grade) with the same procedure, placed in the "in situ" oxidation chamber and exposed at room temperature to high purity O_2 (from LO_2 source) passed through a deionized H_2O bubbler at 25°C. Sample oxidation times ranged from 50 to 200 hours. An oxide thickness of approximately 30-40Å was typically obtained.

An initial etching and chemical depth profiling were conducted using a spinning technique. Samples (9.5mm x 9.5mm) were mounted on a Teflon holder and spun at 3600 rpm. Etchant and rinse solutions were added dropwise to the spinning sample. Samples were spun to dryness and introduced immediately into the spectrometer. The sample etch rate could be controlled by varying the etchant concentration, the amount of etchant added and the velocity at which the sample was rotated.

The ion milling experiments utilized a 3M minibeam ion gun mounted in a pretreatment chamber isolated from the XPS analysis chamber. To perform the experiment, the chamber (with a base pressure of 10^{-8} - 10^{-9} Torr) was back-filled with argon to a pressure of 5×10^{-7} Torr. The argon was obtained from a liquid argon source and passed through a reactive Matheson gas purifier.

An Ar^+ energy of 1.0 KeV was used with a rastered beam current of 1.7×10^{-7} amps. The rastered ion beam area exceeded the area examined by the x-ray beam. The sample was exposed to $\sim 10^{15}$ Ar^+ ions (one monolayer) between subsequent XPS spectra.

II. RESULTS AND DISCUSSION

A. Initial Substrate Surface

Control of the initial substrate surface prior to oxidation is of key importance in a study of oxide/substrate interfaces. Because all sample cleaning procedures reported in the literature are based on aqueous solutions and performed in laboratory air, there will necessarily remain some native oxide on the substrate surface. The exact nature and thickness of this oxide is difficult to control. In order to establish a reproducible surface after cleaning and prior to oxidation, samples were etched under N_2 with 100 microliters 10:1 ethanol:HCl and rinsed with ethanol using the spinner technique already described. This procedure was found to give highly reproducible surfaces with negligible oxygen and carbon. Figures 1 and 2 compare typical GaAs surfaces before and after the acid etch. The top spectra, (a), are obtained after a standard clean. The presence of arsenic and gallium oxides is indicated in Figure 1(a) by the chemically shifted peaks $\sim$3 eV and $\sim$1 eV upfield of the As 3d and Ga 3d substrate lines, respectively. There is also a large oxygen 1s signal as shown in Figure 2(a). The bottom spectra are obtained after the ethanol:HCl etch. The As and Ga oxide signals in Figure 1(b) as well as the oxygen signal in Figure 2(b) are no longer detectable.

Unlike Chang, et al[28], we did not find that an HCl etch left a highly contaminated surface. The only contaminant found was carbon and as shown in Figure 2(a) and 2(b), the amount detected before and after the etch remained essentially constant. If one assumes an escape depth of 15Å for a carbon overlayer, the carbon signal represents less than one monolayer on the surface. The ratio of As to Ga after the etch was 1.2.

B. X-Ray Induced Damage

An additional question that must be addressed before examination of the data is the effect of x-ray irradiation on oxide composition. This is particularly important for the GaAs oxide system because of the high vapor pressure of As_2O_3 ($\sim$6 torr at 200°C).[29] Despite the fact that several studies in the literature have demonstrated the GaAs oxide is severely perturbed by x-ray irradiation at room temperature, most profile studies reported by other workers

are obtained under such conditions. Iwasaki, et al, noted that not only was there a ~50% reduction in As oxide intensity after 85 minutes of irradiation, but also that the chemical shift of the As 3d oxide level decreased from 3.0 eV to 2.4 eV.[30] Such a perturbation of a system under study makes the conclusions drawn under such conditions untenable. We have found that by maintaining the sample temperature at 200°K the above problems can be avoided. Figure 3 shows the As 3d region of an oxidized GaAs substrate before and after 18 hours of x-ray irradiation. No chemical shift of the oxide is observed and the ratio of As oxide to As substrate has remained constant. The lack of observable x-ray damage can also be attributed in part to the fact that the total x-ray flux impinging on the sample in an HP ESCA spectrometer is several orders of magnitude lower than the flux in unmonochromated systems.

C. Profiling Experiments

Most surface analytical techniques have information depths on the order of 10-100 Å because of the limited mean free path from which electrons can escape. Consequently, depth profiling methods must be used to study interfacial regions and to examine compositions as a function of depth. The most widely used methods of profiling are ion sputtering and wet chemical etching. Ion sputtering typically utilizes Ar^+ ions at kinetic energies of 0.5-5 KeV and has been shown to induce chemical and compositional damage into the system due to the deposition of energy from the sputtering particles.[31-34] This point will be discussed in more detail later when ion milling results are presented. The second method of depth profiling, wet chemical etching, is usually performed by immersion of the sample in some aqueous etchant solution, thereby allowing etchant species and water molecules to penetrate the oxide layer. Again the probability of perturbation of the oxide by the profiling procedure is very high. However, we have found that by spinning the sample rapidly, 3600-80,000 rpm, and adding the etchant in microliter increments, the exposure of the oxide to the etchant system is minimized and damage to the oxide is confined to the first several surface layers. Thus, whereas ion sputtering and etchant submersion methods of profiling create damage to depths greater than the information depth of the spectroscopy, the spinning technique damages only the surface of the region probed by the photoelectrons. By comparing spectra from sequential etches, one may infer if damage is being introduced.

Initial profiling experiments which were undertaken to determine the feasibility and controllability of spin etching, used 0.1% bromine in methanol as the etchant. Six sequential etches were performed with 100 µl etchant followed by 100 µl methanol. The As 3d region obtained after each etch is shown in Figure 4. The z axis represents volume of etchant added. The data are plotted in such a way that one is looking from the initial oxide surface toward the oxide/substrate interface. The peak at 40.6 eV is due to the As from the GaAs substrate and increases rapidly because of the exponential dependence of substrate intensity on oxide overlayer thickness. The peak ~3.2 eV upfield of the substrate peak corresponds to As_2O_3 as determined by this work and others.[35,36] In Figure 4(b), the data are plotted on an expanded y axis and from the interface towards the initial oxide surface. Only 5-7 Å of oxide are removed per etch and in a uniform manner. The Ga 3d region is displayed in Figure 5 from the initial surface towards the oxide/substrate interface. The gallium oxide peaks fall only slightly upfield of the substrate line and thus appear as an unresolved shoulder. Again, the oxide removal appears to be uniform and controllable. Examination of other photoelectron lines indicate, however, that undesirable etchant residues remain on the oxide surface and obscure spectral interpretation. In particular, the oxygen 1s photoline shifted from 531.2 eV to 532.0 eV with a simultaneous buildup of a Br 3d signal as the etches proceeded. Obviously, one can not easily determine if this O 1s shift is due to an actual chemical change of the oxide with thickness or whether it is simply (and more probably) a reaction product of Br with the oxide that is not removed with the subsequent methanol rinse. Thus, this profile system serves only to demonstrate the feasibility and controllability of the spin technique and has only limited value as far as obtaining the desired chemical information. An etchant system that is less reactive (or at least leaves no reaction residues behind) is necessary.

Examination of the properties of arsenic and gallium oxide suggested the use of ammonia dispersed in ethanol as an etchant. One can see upon examination of the Pourbaix diagrams[37], that Ga_2O_3 is very soluble above pH = 11 and that As_2O_3 becomes increasingly soluble with pH above pH = 9. In addition, gallium

hydroxide is extremely soluble in ammonia solutions and the complexation of arsenic oxide by ammonia is quite favorable through the reaction[38]

$$4OH^- + As_2O_3(s) + 6NH_4OH\ (aq) \rightleftharpoons 2(NH_4)_3\ AsO_4\ (aq) + 5H_2O + 4e^-.$$

The free energy of formation, ΔG^o_{298}, for this reaction is less than -100 Kcal. Several etchant concentrations were tried and a solution of 10:1 ethanol: NH_4OH was found to give the most controllable etch rate. The ethanol/NH_4OH chemical depth profile of a 30-40 Å native GaAs oxide prepared as described previously is illustrated in Figures 6 and 7. Figure 6 displays a vertical plot of As 3d spectra. Only 7 of the 13 etches are displayed for simplicity. The peak at 40.6 eV corresponds to the GaAs substrate and that at ∿44 eV to As_2O_3. Note that the oxide intensity decreases monotonically as the etching proceeds and there is no substantial shift of the oxide peak relative to the substrate peak. (All chemical shifts will be referenced to the As 3d substrate binding energy to avoid ambiguities caused by charging effects.) The As 3d spin-orbit splitting of ∿0.65 eV is resolved only in the substrate region and is maintained throughout the profile. The relative intensities of the $3d_{3/2}$ and $3d_{1/2}$ spin-orbit components, however, vary as a function of oxide thickness. This strongly suggests the presence of As^o since arsenic metal is known to fall only 0.6 eV upfield of As in GaAs and, hence, it would manifest itself only as apparent changes in the intensity ratio of the As 3d doublet. The presence of arsenic metal in the oxide has also been suggested from ellipsometric studies.[39] XPS and AES studies by others[40,41] have suggested its presence, in addition, although since their published spectra indicate they do not resolve the spin-orbit splitting of the As 3d it is not clear upon what evidence they base their conclusion.

The Ga 3d spectra for the corresponding profile are plotted in Figure 7. The Ga 3d line from the GaAs substrate is observed at 18.7 eV. The gallium oxide, which appears as an unresolved shoulder, decreases monotonically. The oxide binding energy is consistent with Ga_2O_3.

Figure 8 displays a typical wide scan taken between subsequent etchants to monitor contamination. The only observable contaminant is carbon. It was monitored in detail during the profiling and found to remain essentially constant.

The nitrogen 1s signal, although difficult to monitor because of interference from a substrate Auger line, was not found to increase as the etching proceeded.

Note that in Figures 7 and 8, after ten etches, all arsenic oxide has been removed while substantial gallium oxide still remains. This is better illustrated in Figure 9 where the integrated oxide and substrate intensities for both As and Ga are plotted against the volume of etchant added. The integrated intensities were obtained by a least squares fit of an unconstrained Gaussian function to the oxide and substrate regions. The intensities have been normalized by the number of sweeps taken and the relative photoelectron cross-section. Two features of the intensity plot should be noted. The first is the sharp dip both the As and Ga substrate signals appear to take close to the oxide/substrate interface. The nature of this dip is not understood, but it is reproducible. The second feature is that the As oxide intensity goes to zero in advance of the gallium oxide. A similar observation was made by Wilmsen, et al, while studying anodic oxides or GaAs with argon ion sputter profiling.[42] There are two possible explanations for this intensity behavior: (1) the etchant solution preferentially etches As oxide over Ga oxide or (2) there exists a layer of essentially pure Ga oxide at the substrate/oxide interface. These possibilities are examined in more detail below. In Figure 10 are plotted the oxide to substrate ratios versus etchant volumes for the As 3d and Ga 3d regions. We see that initially the removal of the arsenic and gallium oxides parallel one another. After the addition of $\sim$300 μl of etchant, the gallium oxide etch rate levels off while the arsenic oxide intensity continues to decrease. This change in susceptibility to attack by the NH_4OH/ethanol etchant suggests there is a Ga oxide layer at the oxide/substrate interface that is chemically and/or structurally distinct from the Ga oxide near the air/oxide interface. This region is not purely gallium oxide since arsenic oxide continues to be extracted by the etchant solution.

It is possible to extract information about relative concentrations of arsenic and gallium in the various oxide regions using the XPS profile data. In analyzing the data, one must assume the x-ray beam remains essentially unattenuated over the region from which the photoelectrons emerge. The number

of photoelectronics of a given kinetic energy observed from an incremented layer of thickness x is given by

$$dI = F \alpha D K e^{-x/(\lambda \sin \theta)} dx \qquad (I.)$$

where

F = x-ray flux

α = photoionization cross section for a given level in a given atom

D = density of the given atom

K = spectrometer factor (includes detector counting efficiency and various geometrical factors)

λ = electron attenuation length

θ = electron ejection angle

Aside from the density, only two parameters in (I), α and λ, are sample dependant. The photoionization cross section is essentially an atomic property[43] and depends on the element and binding energy of the level under consideration. The attenuation length, λ, is a property of the sample matrix and depends strongly on the kinetic energy of the ejected electron. Because the binding energy for electrons from the As 3d and Ga 3d levels are very close, we may make the approximation that the attenuation length of a given layer is essentially the same for both.

Consider modeling the GaAs oxide as a multilayered system as shown in the insert in Figure 11. The number of layers, n, must be large enough that one can consider each individual layer as homologous. One must also assume that there are no large lateral nonuniformities. In the limit, we can consider as many layers as we have etch steps. Each layer is then equal to that amount of oxide removed in a single etch.

To illustrate the calculation consider a simple system. With no oxide present, the intensity of the As 3d line from the substrate can be found by integration of (I).

$$I_{As(sub)}^{\text{no oxide}} = F \alpha_{As} D_{As(sub)} K \int_0^{\infty} e^{-x/(\lambda_{sub} \sin \theta)} dx$$

where

α_{As} = photoionization cross-section for As 3d

$D_{As\,(sub)}$ = density of As in GaAs substrate

For a system with one oxide layer of thickness d_1, the intensity of the As 3d signal from the arsenic oxide is

$$I_{As\,(oxide\,1)} = F\alpha_{As}\, D_{As\,(oxide\,1)}\, K \int_0^{d_1} e^{-x/(\lambda_1 \sin\theta)}\, dx$$

$$= F\alpha_{As}\, D_{As\,(oxide\,1)}\, K\lambda_1 \left(1 - e^{-d_1/(\lambda_1 \sin\theta)}\right)$$

where

λ_1 = attenuation length for the oxide layer (oxide 1)

$D_{As\,(oxide\,1)}$ = density of As in the oxide layer

The 3d signal from the substrate is now attenuated by layer 1 and its intensity is

$$I^{\text{oxide 1}}_{As(sub)} = F\alpha_{As}\, D_{As(sub)}\, K \int_{d_1}^{\infty} e^{-d_1/(\lambda_1 \sin\theta)}\, e^{-(x-d_1)/(\lambda_{sub} \sin\theta)}\, dx$$

$$= F\alpha_{As}\, D_{As\,(sub)}\, K\lambda_{sub}\, e^{-d_1/(\lambda_1 \sin\theta)}$$

By taking the ratios of the various experimentally determined intensities, many of the difficult to evaluate constants cancel. Thus,

$$\frac{I^{\text{oxide 1}}_{As(sub)}}{I^{\text{no oxide}}_{As\,(sub)}} = e^{-d_1/(\lambda_1 \sin\theta)} \qquad \text{(II)}$$

and

$$\frac{I_{\text{As (oxide 1)}}}{I^{\text{oxide 1}}_{\text{As (sub)}}} = \frac{1 - e^{-d_1/(\lambda_1 \sin\theta)}}{e^{-d_1(\lambda_1 \sin\theta)}} \cdot \frac{D_{\text{As (oxide 1)}}\,\lambda_1}{D_{\text{As (sub)}}\,\lambda_{\text{sub}}} \qquad \text{(III)}$$

Substitution of the various experimentally obtained intensities into (II) and (III) thus yields a value for

$$\frac{D_{\text{As (oxide 1)}}\,\lambda_1}{D_{\text{As (sub)}}\,\lambda_{\text{sub}}}$$

For a system with two oxide layers on a GaAs substrate, one may calculate the As 3d substrate and oxide intensities by again integrating (I) with the appropriate integration limits. After taking the ratio of the calculated intensities one finds:

$$\frac{I_{\text{As (oxide 1 + oxide 2)}}}{I^{\text{(oxide 1 + oxide 2)}}_{\text{As (sub)}}} = \frac{D_{\text{As (oxide 1)}}\,\lambda_1}{\text{As (sub)}\,\lambda_{\text{sub}}} \cdot \frac{1 - e^{-d_1(\lambda_1 \sin\theta)}}{e^{-d_1(\lambda_1 \sin\theta)}\; e^{-d_2/(\lambda_2 \sin\theta)}}$$

$$+ \frac{D_{\text{As (oxide 2)}}\,\lambda_2}{D_{\text{As (sub)}}\,\lambda_{\text{sub}}} \cdot \frac{1 - e^{-d_2/(\lambda_2 \sin\theta)}}{e^{-d_2/(\lambda_2 \sin\theta)}} \qquad \text{(IV)}$$

and

$$\frac{I^{\text{(oxide 1 + oxide 2)}}_{\text{As (sub)}}}{I^{\text{no oxide}}_{\text{As (sub)}}} = e^{-d_1/(\lambda_1 \sin\theta)}\; e^{-d_2/(\lambda_2 \sin\theta)}$$

$$= \frac{I^{\text{(oxide 1 + oxide 2)}}_{\text{As (sub)}}}{I^{\text{oxide 2}}_{\text{As (sub)}}}\; e^{-d_1/(\lambda_1 \sin\theta)} \qquad \text{(V)}$$

where

d_2 = thickness of second oxide layer

λ_2 = attenuation length for the second oxide layer

Again, all intensity ratios may experimentally determined. Substitution of these intensities into (IV) and (V) yields the value of

$$\frac{D_{As\ (oxide\ 2)}\,\lambda_2}{D_{As\ (sub)}\,\lambda_{sub}}$$

Repeating the above calculations with the Ga 3d intensities yields analogously

$$\frac{D_{Ga\ (oxide\ 1)}\,\lambda_1}{D_{Ga\ (sub)}\,\lambda_{sub}} \quad \text{and} \quad \frac{D_{Ga\ (oxide\ 2)}\,\lambda_2}{D_{Ga\ (sub)}\,\lambda_{sub}}$$

Since $D_{Ga(sub)} = D_{As\ (sub)}$, one may take the ratio of the above quantities to get

$$\frac{D_{As\ (oxide\ i)}}{D_{Ga\ (oxide\ i)}}$$

These equations may be straightforwardly extended to the n layer system diagrammed in Figure 11.[44] The graph in the same figure displays the calculated density ratios of arsenic and gallium in the oxide as a function of etchant volume assuming seven layers. The atom density ratio As/Ga at the oxide/air interface averages ~0.5-0.6. As one progresses towards the oxide/substrate interface the As/Ga ratio falls to ~0.1-0.2. This drop in the arsenic content of the oxide occurs approximately at the same point as the decrease in the gallium oxide etch rate in Figure 10. The transition point in Figure 11 is somewhat abrupt rather than very gradual. A gradual transition would be expected if the composition change was due entirely to the etchant solution "leeching" the arsenic oxide from the gallium oxide layer. The calculations,

of course, ignore the small amount of arsenic metal that was suggested earlier as being present in the oxide. The photoelectron intensity from this As^{o} would be included in the substrate intensity. As a result, the calculated As/Ga ratios will be slightly lower than the actual ratios. The error from this is not expected to be large enough to change any of the qualitative conclusions. This aspect of the data analysis thus suggests there exists a region at the oxide/substrate interface 2-3 times richer in gallium oxide than arsenic oxide than the region at the oxide/air interface. This oxide/air interface region consists of approximately twice as much gallium oxide as arsenic oxide.

The existence of such a layering in the oxide is not unreasonable given the volatility of arsenic oxide. The GaAs substrate was oxidized over an extended period of time to allow the oxide to approach its equilibrium composition. Since the oxide growth rate falls off exponentially with time[45], the system will reach a state where the arsenic oxide is subliming faster than the substrate is oxidizing. This would produce a region near the oxide/substrate interface rich in gallium oxide. In addition, since the gallium oxide in this layer is no longer "disolved" in a vitreous arsenic oxide matrix, a different structural form could be stabilized. This structurally different gallium oxide would explain the observed change in etch rate with the NH_4OH/ethanol solution.

Ion Induced Damage

To compare the chemical etching technique with the more common Ar^+ ion milling method of depth profiling, two spectra of the As 3d region taken at approximately the same oxide thickness are plotted in Figure 12. The upper spectrum is obtained from a chemical profile with NH_4OH in ethanol, while the lower spectrum is obtained by ion milling with 1.0 KeV Ar^+. Notice that after ion bombardment the As oxide binding energy and linewidth have decreased. In addition the As 3d spin-orbit splitting is no longer resolvable. Since the positions and resolution in the chemical etch case agree with that obtained before any profiling was performed, the ion bombardment must generate reduced chemical species in the oxide. Such chemical changes of the sample oxidation state due to ion sputtering have been reported in the literature.[31-34, 46-48]

Though the theory for physical sputtering has been developed for monoelemental targets,[49-51] the mechanism by which chemical changes may occur in multicomponent systems is not understood.

The ion-milled profile does, however, reproduce the gallium oxide rich region near the oxide/GaAs interface. It would appear that the sputter yields may be determined by the chemical structure in much the same fashion as are the reactivities of the chemical etchant. Nevertheless, the original oxidation state of the oxide/GaAs interface is irreversibly modified by the use of such ion milling profiling techniques. This limits its usefulness for determination of chemical states in conjunction with XPS and AES.

Oxide Chemical Shifts

The chemical shifts reported here are all measured relative to the GaAs substrate As 3d line. This is to avoid any ambiguities due to charging of the sample surface during the photoemission experiments. In Figure 13 are plotted the differences in binding energy between various photoelection lines and the As 3d line of the substrate versus the number of chemical etches. The data in (a) represent the differences between the As 3d and Ga 3d lines of the substrate. Of course, the difference should be constant (unless charging occurs while the spectra are being accumulated) and the plot thus serves to determine the error in establishing peak positions. This error is, in fact, relatively small with the date having a standard deviation of 0.028 eV. Plots (b), (c), and (d) display the difference in binding energy between the substrate As 3d and the oxide Ga 3d, oxide As 3d, and oxygen 1s, photoelectrons, respectively. The binding energies remain essentially constant throughout most of the GaAs oxide. The gallium oxide is chemically shifted 1.25 $\pm$0.05 eV from the substrate Ga 3d. This is consistent with Ga_2O_3. The arsenic oxide shift relative to the substrate arsenic is 3.37 $\pm$0.05 eV. This is somewhat higher than is expected for As_2O_3 (3.2 eV) but lower than As_2O_5 (5.0 eV). As the oxide/GaAs interface is approached, the binding energies of the gallium oxide and arsenic oxide appear to shift several tenths of an eV toward lower binding energy. The oxygen is simultaneously shifted to higher binding energy. These shifts, though small,

have been reproducible. That the oxide As 3d and oxide Ga 3d shift to lower binding energy while oxygen is shifted to a higher binding energy suggests less charge transfer is occurring between oxygen and the As and Ga atoms at the interfacial region. Possible explanation for the shifts are:

1. There exists several unresolved oxide species under the broad As 3d and Ga 3d oxide envelopes whose relative intensities vary with thickness. The experimentally observed shifts toward lower binding energy would then reflect a higher concentration of lower oxidation state species at the interface.
2. There is a structurally induced charge transfer as bond angles within the oxide are strained in order to match the GaAs substrate lattice geometry. This has been suggested in the case of the SiO_2 oxide.[21]
3. The shifts are due to extra atomic relaxation effects which are attributed to electrons of the system relaxing towards the positive hole created during photoemission. This explanation is unlikely since the oxygen is shifted in a direction opposite to that of the gallium and arsenic oxide shifts.

Possibilities (1) and (2) will be further discussed later.

Spectral Deconvolution

Examination of the Fourier transforms of the As 3d and Ga 3d photoemission lines obtained in the profile experiments indicates substantial structural is contained within the broad oxide envelopes. To gain some insight into the nature of this structure, which has been obscured in the real space representation of the data because of various line broadening effects, deconvolution techniques were applied. Because the deconvolution method used here differs substantially from the usual Fourier transform and real space iterative procedures commonly found in the literature, a brief description of the procedure will be given. This is more easily accomplished by demonstrating the method with a test spectrum that will illustrate the salient features than by presenting a detailed consideration of the theory.

First, let us construct a test spectrum that duplicates the features found in a photoemission line. One can consider the observed XPS spectrum as being generated by the convolution and addition of a variety of functions. In Figure 14(a) is plotted an ideal spectrum of four chemical species with various

energy separations and intensities. Both the real space and frequency space representations of all plots will be shown so that one may easily see the effects various operations have on each domain. Of course, these idealized functions must be broadened by the natural line shape for the element (which is a Lorentzian function) and additionally by an instrumental response function (which is a asymmetric Gaussian). Other broadening effects due to such things as sample charging, photons, etc., are generally accepted to be gaussian and, for our purposes, they will be considered as part of the instrumental response function. The result of convolving the ideal spectrum (14a) with Lorentzian and gaussian broadening functions is shown in Figure 14(b). Notice that the individual species are no longer resolvable in real space, but that the transform stills shows rather detailed structure. Observe, however, that all frequency terms beyond the 50th term have been irretrievably lost. In addition, the spin-orbit splitting of the given electron level, which for a d level is a 2:3 doublet as shown in Figure 14(c), must be convolved into the test spectrum. This results in the spectrum shown in Figure 15(a). Finally, the addition of Poisson noise to a signal to noise ratio of 800 yields the experimentally observed spectrum shown in Figure 15(b). Notice that the addition of noise has caused the loss of all frequency terms higher than the 20th term. The phase spectrum also goes random at approximately this term.

Since the natural line shape, instrumental response function, and spin-orbit component are known with varying degrees of precision, one can attempt to retrieve the ideal spectrum by inversion of the above convolutions. This is known as deconvolution or resolution enhancement. The term deconvolution is often confused in the literature with non linear least squares fitting procedures which cannot yield correct solutions for overlapping and unresolved structures. Similarly, the iterative real space deconvolution techniques commonly found in the literature lead to non-unique solutions. The Fourier transform deconvolution methods differ basically in the manner in which they assign values to the higher frequencies. For example, Fourier truncation methods simply assign zero to all frequencies beyond some cufoff frequency. Sinc deconvolution and the other linear filter methods also assign zero to higher frequency but they approach zero more gently so as to avoid the oscillations in real space caused

by sharp truncation of the transform. The deconvolution method used here is a relatively new approach based on linear predictive filtering.[52] The procedure is to fit the well known low frequency terms of the transform with a linear predictor and then extrapolate this result to higher frequencies using a maximum entropy approach. (A maximum entropy approach is one that utilizes the available information but is maximally noncommittal with regard to unavailable information.[53] The only information we make available is that the data are real and positive definite.) The linear prediction algorithm also yields an estimate of the error in the final prediction. We have used this error prediction to develop heuristic procedures for determining the amount of gaussian component in the data and also for determining the splitting of the spin orbit components. Once these functions have been determined they can be removed from the Fourier transform by simple division. Linear prediction can then be applied to the resultant transform to yield an estimate of the chemical species present in the spectrum.

To illustrate the technique let us apply it to the test spectrum previously generated. In Figure 16(a), is plotted the result of removing the spin-orbit component from 15(b) by Fourier division. Notice that unlike the noiseless case in 14(b), still only the first 20 frequency terms are available. After removing an empirically determined gaussian line shape one obtains the plot in Figure 16(b). The high frequency terms are amplified because one has divided by a function whose high frequency terms have small amplitude. In Figure 17(a), (b), and (c) are shown the results of applying the linear prediction method to the transform in 16(b). In 17(a), the linear predictor has been given the first 10 frequency terms upon which to base its extrapolation to higher frequencies. In 17(b) and 17(c), it has been given the first 12 and 14 frequency terms, respectively. The top Fourier transform in each figure is the original transform from 16(a). The bottom transform is the predicted transform. Observe that the predicted transform agrees with the actual transform in both amplitude and phase up to approximately the 20th frequency term. Notice also that at least 14 frequency terms are required by the prediction algorithm to reproduce the closely spaced peaks at channels 184 and 192. The closer two peaks are in real space, the more frequency terms required to

reproduce them. The ultimate resolution obtainable is thus limited by the number of frequency terms available before the noise power interfaces. For comparison, two other common deconvolution methods are shown in Figure 18. The result we obtained with linear prediction using the first 14 frequency terms is plotted over the ideal spectrum in 18(a). The result is, of course, broader than the ideal since we did not remove any of the Lorentzian component. The predicted transform agrees remarkably well with the ideal transform. It has a downward slope because of the Lorentzian component still present. In 18(b) is the result of truncating the transform from 16(b) at frequency term 25. The peaks at 184 and 192 are not resolved and the structure that is present is made questionable by the extreme oscillations produced by the frequency truncation. In 18(c) one has gotten rid of the oscillations by rolling off the transform to zero with a (sin x)/x function. The oscillations are no longer present but the peaks still remain unresolved. Clearly, the linear predictor in 18(a) must correctly predict past the first 25-30 terms given only the first 14 terms. Extensive test cases (of much greater difficulty than the one illustrated here) have been attempted with this linear prediction method and it shows much potential.

Spectra of the Ga 3d and As 3d regions obtained at various oxide thicknesses during the chemical profiling of the native GaAs oxide were deconvolved using the prediction procedure described above. The results are shown in Figures 19 and 20. Plotted along with the deconvolved results are the original spectra with the spin-orbit component removed. In Figure 19, the deconvolution suggests that three gallium oxide species are present and that their relative intensities vary as a function of oxide thickness. In the lower spectrum one can see inflections in the original data that correspond to the peaks found by deconvolution. The peak 1.3 eV upfield (to the left) of the substrate corresponds to Ga_2O_3 and it appears to decrease relative to the peak 0.5 eV upfield. We have assigned the peak 1.9 eV upfield to the mixed oxide $GaAsO_4$. Since the oxidation state of As and Ga must average 4 in the mixed oxide, one would expect the Ga in $GaAsO_4$ to fall at a binding energy greater than that of Ga_2O_3. The mixed oxide also appears to decrease in intensity relative to the peak 0.5 eV upfield as the oxide thickness is reduced. The peak 0.5 eV upfield is more difficult to assign.

since Ga_2O_3 is known to exist with both octahedral and tetrahedral oxygen coordination[54], we suggest that the peak 0.5 eV upfield is the tetrahedral structure while the peak 1.3 eV upfield is the octahedral. The peak 0.5 eV upfield appears to be the dominant species present in the oxide layer that is resistant to the NH_4OH/ethanol etchant. The other two species, $GaAsO_4$ and Ga_2O_3 (octahedral), dominate in the thicker oxide. One can calculate the expected shift of the moment of the experimentally observed oxide peak as one goes from a thick to a thin oxide using the relative intensities and positions of the components determined by the deconvolution. The calculated expected shift is 0.4 eV towards lower binding energy. In figure 13 one observes an experimental shift of $\sim$0.3 eV. This is consistent with a multicomponent oxide model.

In Figure 20 are plotted the results of deconvolving the As 3d regions at various oxide thicknesses. The peak 0.7 eV upfield of the substrate corresponds to the binding energy for arsenic metal. Recall that the presence of As^o was also suggested earlier because of the variation in the intensity ratio of the spin-orbit components of the substrate 3d line. Its presence is also indicated from a shoulder on the low binding energy side of the substrate lines in the original data (spin-orbit component removed) plotted in Figure 20. The arsenic metal appears to be contained within or underneath the gallium oxide layer that is not removed by the etchant. The most intense oxide peak, which falls 3.6 eV upfield of the substrate, can be assigned to As_2O_3. As_2O_5, which is expected to appear $\sim$5 eV upfield, is present at a minor level. The mixed oxide, $GaAsO_4$, would be expected to fall between As_2O_3 and As_2O_5 and, thus, it is assigned to the peak 4.2 eV upfield. The peaks 2 eV and 3 eV upfield are unassigned at this point. Perhaps they represent other mixed oxide structures.

Very recently, it has come to our attention that the equilibrium phase diagram for gallium, arsenic, and oxygen has been calculated from thermodynamic considerations by B. Schwartz and G. Schwartz.[55] Their calculations predict that the equilibrium composition of the GaAs native oxide will consist of a layer of Ga_2O_3 and As metal at the oxide/substrate interface. The layer above this will be composed of a mixture of Ga_2O_3 and As_2O_3. The final layer at the

air/oxide interface will be composed of $GaAsO_4$. Our experimental results are in strong agreement with these predictions. This agreement can be interpreted as an indication that the native oxides used in our experiments had indeed reached their equilibrium compositions.

Summary

In this study we have examined the chemical structure of the thin native oxide formed on GaAs after a controlled room temperature oxidation with water saturated oxygen. We have carefully chosen experimental conditions that do not show evidence of X-ray beam damage of the oxide or loss of arsenic oxide to the vacuum. Chemical etching has been used to depth profile the oxide with a spinning technique that minimizes solvent contact with the sample.

The chemical profiling method has been compared to the more conventional argon ion milling technique of depth profiling. The ion generated profiles (1 keV Ar^+) reproduce the basic composition gradient found by chemical etching, but show substantial chemical degradation.

The key observation from the photoemission data is the extreme compositional complexity of the GaAs oxide. Evidence is found for the presence of Ga_2O_3, As_2O_3, and the mixed oxide $GaAsO_4$. Several other species have been found and possible assignments are discussed. The oxide has an arsenic oxide to gallium oxide ratio of $\sim$0.5 at the oxide/air interface region and a ratio of $\sim$0.1-0.2 at the oxide/substrate interface region. The gallium oxide present in this oxide/substrate interface region is chemically and/or structurally different from that found in the rest of the oxide. Arsenic metal is also found to be present in this anomalous gallium oxide layer at the oxide/GaAs interface. Figure 21 summarizes the above conclusions.

The width and exact nature of the gallium oxide layer at the oxide/GaAs interface region (as well as the arsenic oxide to gallium oxide ratios) should depend heavily on the sample processing and oxidation conditions. Parameters such as the percent of water saturation in the oxygen, for example, would effect the amount of oxide hydration and, hence, perhaps the volatility of the arsenic oxide species. Other conditions such as the flow rate of the oxidizing gas and

oxidation temperature, which clearly effect oxide growth rate, would also effect the interfacial structure. The study reported here lays only the ground work for understanding the native oxide of GaAs. A systematic study of the effect of various processing conditions on the oxide structure and composition is necessary for a complete understanding of this complex system.

REFERENCES

1. Zaininger, K.H., Revesz, A.G., J. Phys. Paris, 25 (1964) 208
2. Minden, H.J., J. Electrochem. Soc., 109 (1962) 733
3. Rubenstein, M., J. Electrochem. Soc., 113 (1966) 540
4. Dewald, J.F., J. Electrochem. Soc., 104 (1957) 244
5. Chang, L.L., Esaki, L., Jona, F., Appl. Phys. Lett., 9 (1966) 21
6. Schwartz, B., J. Electrochem. Soc., 118 (1971) 657
7. Schwartz, B., Sundburg, W.J., J. Electrochem. Soc., 120 (1973) 576
8. Spitzer, S.M., Schwartz, B., Kuhn, M., J. Electrochem. Soc., 120 (1973) 669
9. Weinreich, O.A., J. Appl. Phys. 37 (1966) 2924
10. Chang, R.P.H., Sinha, A.K., Appl. Phys. Lett., 29 (1976) 56
11. Chang, R.P.H., Sinha, A.K., Appl. Phys. Lett., 29 (1976) 56
12. Muraska, S.P., Appl. Phys. Lett., 26 (1975) 180
13. Navratil, K., Czech, J. Phys., B-18 (1868) 266
14. Poate, J.M., Silverman, P.J., Yaholom, Y., J. Electrochem. Soc., 120 (1973) 844
15. Aspnes, D.E., Schwartz, B., Stunda, A.A., Derick, L., Appl. Phys. Lett., 28 (1976) 631
16. Schwartz, B., Ermanis, F., Brasted, M.H., J. Electrochem. Soc., 123 (1976) 1089
17. Hasegawa, H., Hartnagel, H., J. Electrochem. Soc., 123 (1976) 713
18. Arora, B.M., Binkurkar, M.G., Solid State Electron., 19 (1976) 657
19. Muller, H., Eisen, F.H., Mayer, J.W., J. Electrochem. Soc., 122 (1975) 651
20. Ludeke, Phys. Rev. B16 (1977) 5598

21. Pianetta, P., Lindau, I., Garner, C., Spicer, W.E., Phys. Rev. Lett., 35 (1975) 1356

22. Chye, P.W., Pianetta, P., Lindau, I., Spicer, W.E., J. Vac. Sci. Technol., 14 (1977) 917

23. Spicer, W.E., Pianetta, P., Lindau, I., Chye, P.W., ibid. 14 (1977) 885

24. Lindau, I., Pianetta, P., Garner, C.M., Chye, P.W., Gregory, P.E., Spicer, W.E., Surf. Sci., 63 (1977) 45

25. Bauer, R.S., J. Vac. Sci. Technol. 14 (1977) 899

26. Grunthaner, F.J., Maserjian J., IEEE Trans., Nucl. Sci. NS-24, 2108 (1977)

27. Stirn, R.J., Yeh, Y.C.M., Wang, E.Y., Ernest, F.P., Wu, C.J., "Recent Improvements in AMOS Solar Cells", Technical Digest, 1977 IEEE IEDM, Washington, D.C., December 1977

28. Chang, C.C., Citran, P.H., Schwartz, B., J. Vac. Sci. Tech., Vol. 14, No. 4, July/Aug 1977, p??

29. Handbook of Chemistry and Physics, ed. R.C. Weast (The Chemical Rubber Publishing Company, Ohio 1973)

30. Iwasaki, H., Mizokawa, Y., Nishitami, R., Nakamura, S. Jap. J. of Appl. Phys., Vol 17, No. 2, Feb. 1978 p.315

31. Kim, K.S., Baitinger, W.E., Amy, J.W., Winograd, N., J. Elect. Spectros. 5, 351, (1974)

32. Holm, R., Storp, S., Appl. Phys. 12, 101 (1977)

33. Umezawa, Y., Reilley, C.N., Anal. Chem., 50 No. 9, Aug 1978, p. 1290

34. Chuang, T.J., Brundle, C.R., Wandelt, K., Thin Solid Films, 53, 19 (1978)

35. Bahl, M.K., Woodall, R.O., Watson, R.L., Irgolic, K.J., J. Chem. Phys. 64, 1210 (1976)

36. Leonhardt, G., Berndtsson, A., Hedman, J., Klasson, M., Nilsson, R., Nordling, C., Phys. Stat. Sol., (B), 60, 241 (1973)

37. Pourbaix, M., "Atlas of Electrochemical Equilibria in Aqueous Solution", Pergamon Press, New York, 1966

38. Schwartz, B., CRC Critical Reviews in Solid State Sciences, Nov. 1975, p.609

39. Aspenes, D., J. Vac. Sci. and Techn., 16 (1979) 0000

40. Wilmsen, C.W., Kee, R.W., J. Vac. Sci. Technol., 16 (1979) ØØØØ

41.

42. Wilmsen, C.W., J. Vac. Sci. Technol. 16 (1978)

43. Wagner, C.D., Anal. Chem. 49 (1977) 1282

44. Vasquez, R., Private communication

45. Stirn, R.J., Yeh, Y.C.M., IEEE Trans. Electron. Dev. ED-24 (1977) 476

46. Yin, L.I., Ghose, S., Adler, I., Appl. Spectrose. 26 (1972) 355

47. Murti, D.K., Kelly, R., Thin Solid Films, 33 (1976) 149

48. Grunthaner, F.J., Grunthaner, P.J., Vasquez, R.P., Lewis, B.F., Maserjian, J., Madhukar, A., Submitted to J. Vac. Sci. Techn.

49. Sigmund, P., Phys. Rev. 184 (1969) 383

50. Sigmund, P. J. Mater. Sci., 8 (1973) 1545

51. Winters, H.F., Adv. Chem. Sci., 158 (1976) 1

52. Klein, J.D., Barton, J.J., Grunthaner, F.J., To be published.

53. Ulrych, T.J., Bishop, T.N., Reviews of Geophysics and Space Physics 13 (1975) 183

54. Cotton, F.A., Wilkinson, G., Advanced Inorganic Chemistry (John Wiley & Sons, Inc.) 1972, p. 263

55. Schwartz, B., and Schwartz, G., Bell Laboratory, private communication

FIGURE CAPTIONS

Figure 1. (a) spectra correspond to the As 3d and Ga 3d signals after a standard clean. (b) spectra were obtained after etching with 1:10 HCl:ethanol.

Figure 2. (a) spectra are the C 1s and O 1s signals obtained after a standard clean. (b) spectra are obtained after etching with 1:10 HCl:ethanol.

Figure 3. Comparison of the As 3d region before and after 18 hours of exposure to x-rays. Top spectrum is the initial signal. The lower spectrum was obtained after the x-ray exposure.

Figure 4a. 3-D plot of the As 3d spectra obtained between the sequential etches with 0.1% Br in methanol. Spectra are plotted from the oxide surface toward the interface.

Figure 4b. Expanded version of 4a, plotted from the interface towards the oxide surface.

Figure 5. Ga 3d spectra corresponding to the As 3d signals in figures 4a and 4b. Spectra are plotted from the oxide surface towards the interface.

Figure 6. Vertical plot of the As 3d regions obtained between sequential etches with 10:1 ethanol:NH_4OH.

Figure 7. Ga 3d spectra corresponding to the As 3d spectra in figure 6.

Figure 8. Typical wide scan obtained between the chemical etch steps.

Figure 9. Plot of the integrated intensities for the As 3d and Ga 3d substrate and oxide signals as a function of the volume of etchant used.

Figure 10. Plot of the oxide to substrate ratios vs. the volume of etchant used for the As 3d and Ga 3d regions.

Figure 11. Plot of the calculated As/Ga density ratios as a function of the etchant volume used. The insert diagrams the multilayered model used for the oxide.

Figure 12. Comparison of the chemical etching technique to Ar^+ ion bombardment. The top curve is obtained from a profile with NH_4OH/ethanol. The lower curve is from a profile using ion sputtering.

Figure 13. (a) The difference in binding energy between the As 3d substrate signal and the Ga 3d substrate signal vs. the number of chemical etches performed. (b)- the difference in the binding energy between the As 3d substrate signal and the Ga 3d oxide signal. (c)- the difference in binding energy between the As 3d substrate signal and the As 3d oxide signal. (d)- the difference in binding energy between the As 3d substrate signal and the O 1 signal.

Figure 14. (a) an ideal instrumental output, (b) result of the convolution of (a) with Lorenztian and Gaussian broadening functions, (c) the 2:3 spin-orbit doublet for the As 3d level.

Figure 15. (a) the convolution of 14(b) and 14(c), (b) the addition of Poisson noise

Figure 16. (a) the result of removing the spin-orbit component from 15(b), (b) the result of removing the derived gaussian broadening function from 16(a)

Figure 17. (a),(b), and (c) display the results of applying the linear predictor method to 16(b) using 10,12,and 14 frequency terms, respectively. The top FT is from 16(b). The lower FT is the predicted FT.

Figure 18. Comparison of the linear predictor method, (a), to Fourier truncation, (b), and sinc deconvolution, (c). The lower spectrum in each case is the ideal instrument output. The top FT in each case is the FT of the ideal output. The lower FT is the FT obtained by each of the various deconvolution methods.

Figure 19. The deconvolution results for the Ga 3d spectra taken at various points during the depth profiling. The deconvolved results are plotted over the original data with the spin-orbit component removed.

Figure 20. The deconvolution results for the As 3d region. The results are plotted over the original data with the spin-orbit component removed.

Figure 21. Diagram of the chemical species found and their distribution in the GaAs native oxide.

Figure 1

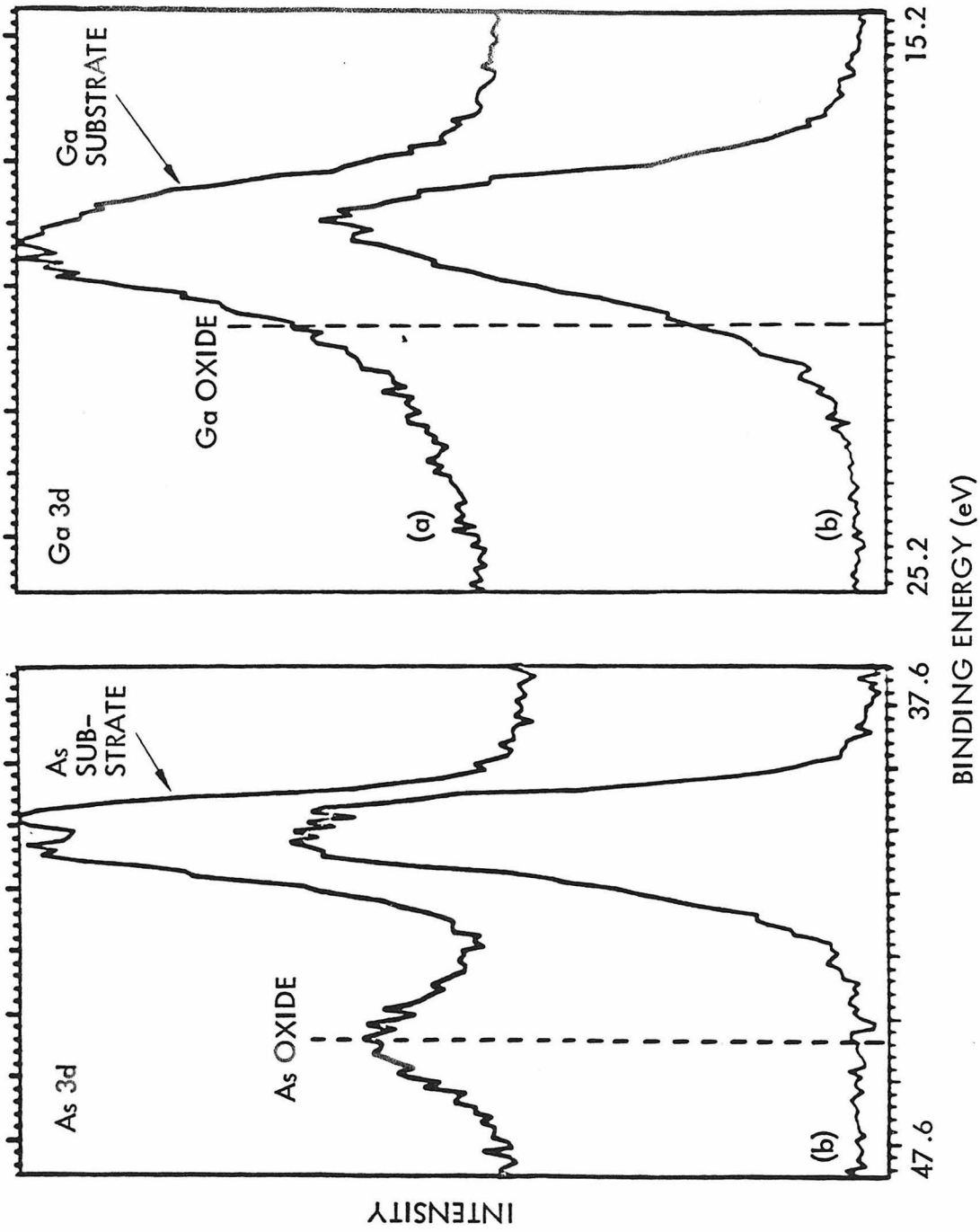
As 3d
As SUB-STRATE
As OXIDE
(b)
47.6
37.6
Ga 3d
Ga SUBSTRATE
Ga OXIDE
(a)
(b)
25.2
15.2
INTENSITY
BINDING ENERGY (eV)

Figure 2

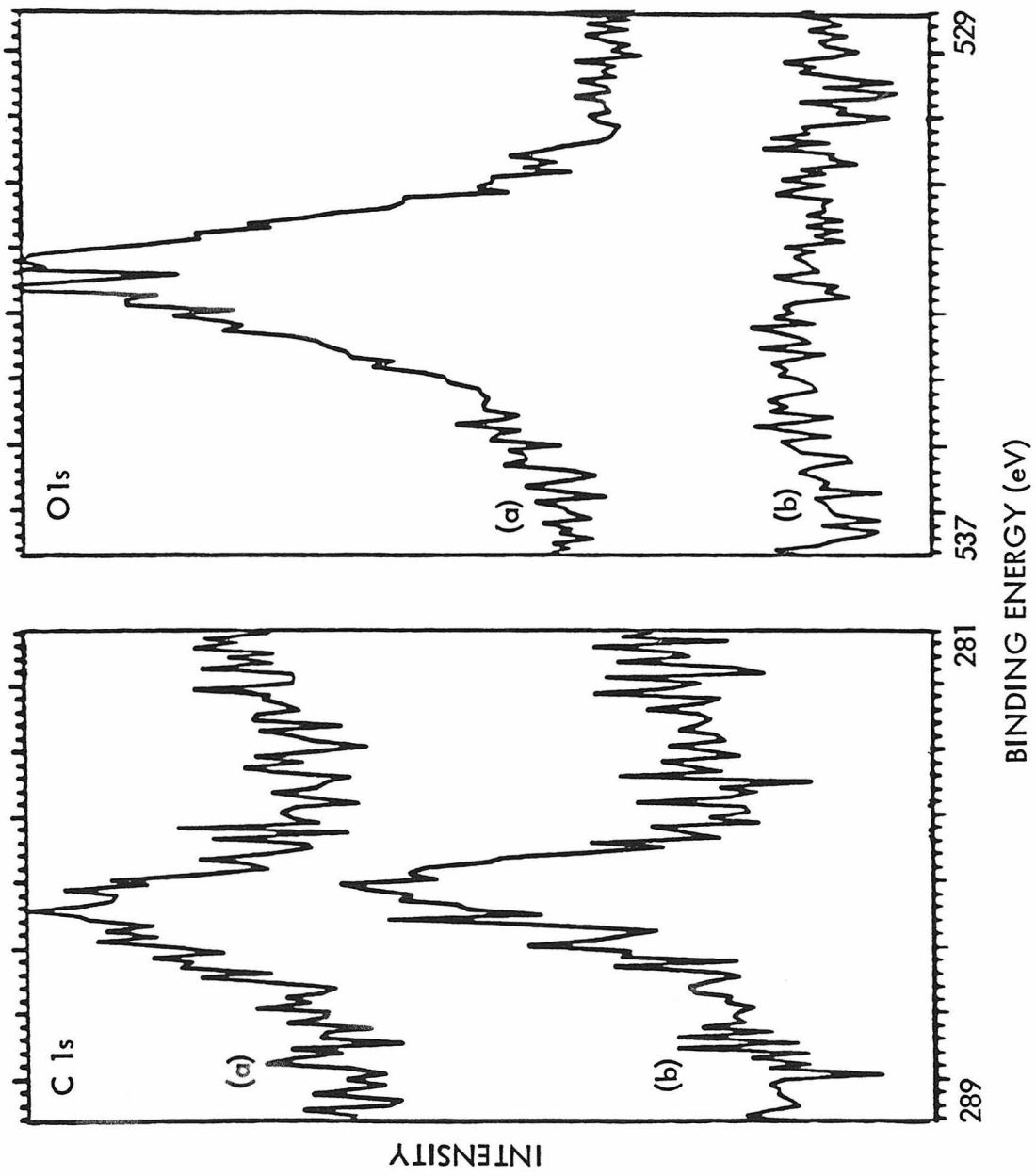

Figure 3

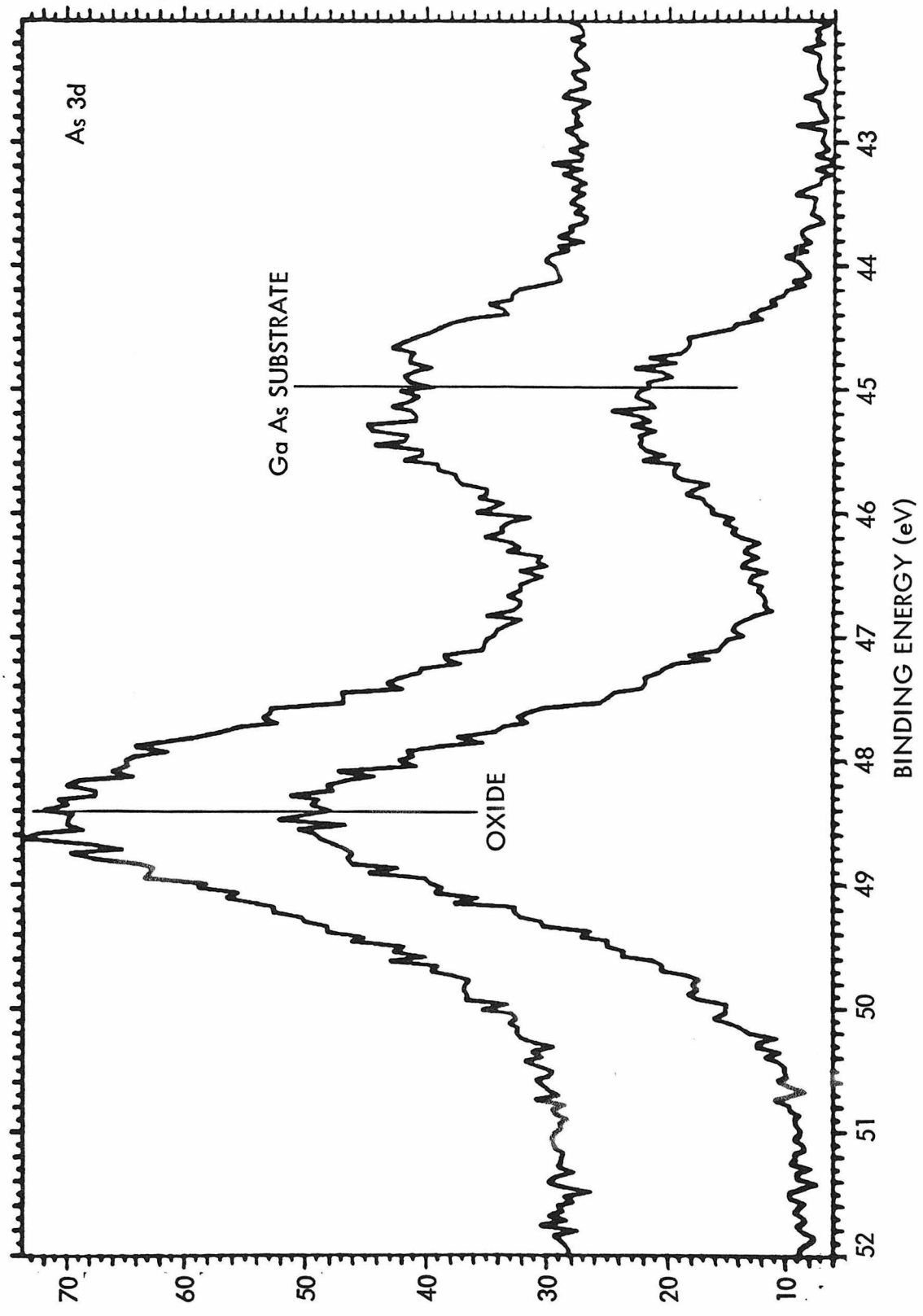
As 3d
Ga As SUBSTRATE
OXIDE
70
60
50
40
30
20
10
52
51
50
49
48
47
46
45
44
43
BINDING ENERGY (eV)

Figure 4a

As 3d REGION
COUNTS (x 10³)
40
20
BINDING ENERGY (eV)
40
42
44
46
ETCH #
0
2
4
6
INTERFACE
OXIDE SURFACE

Figure4b

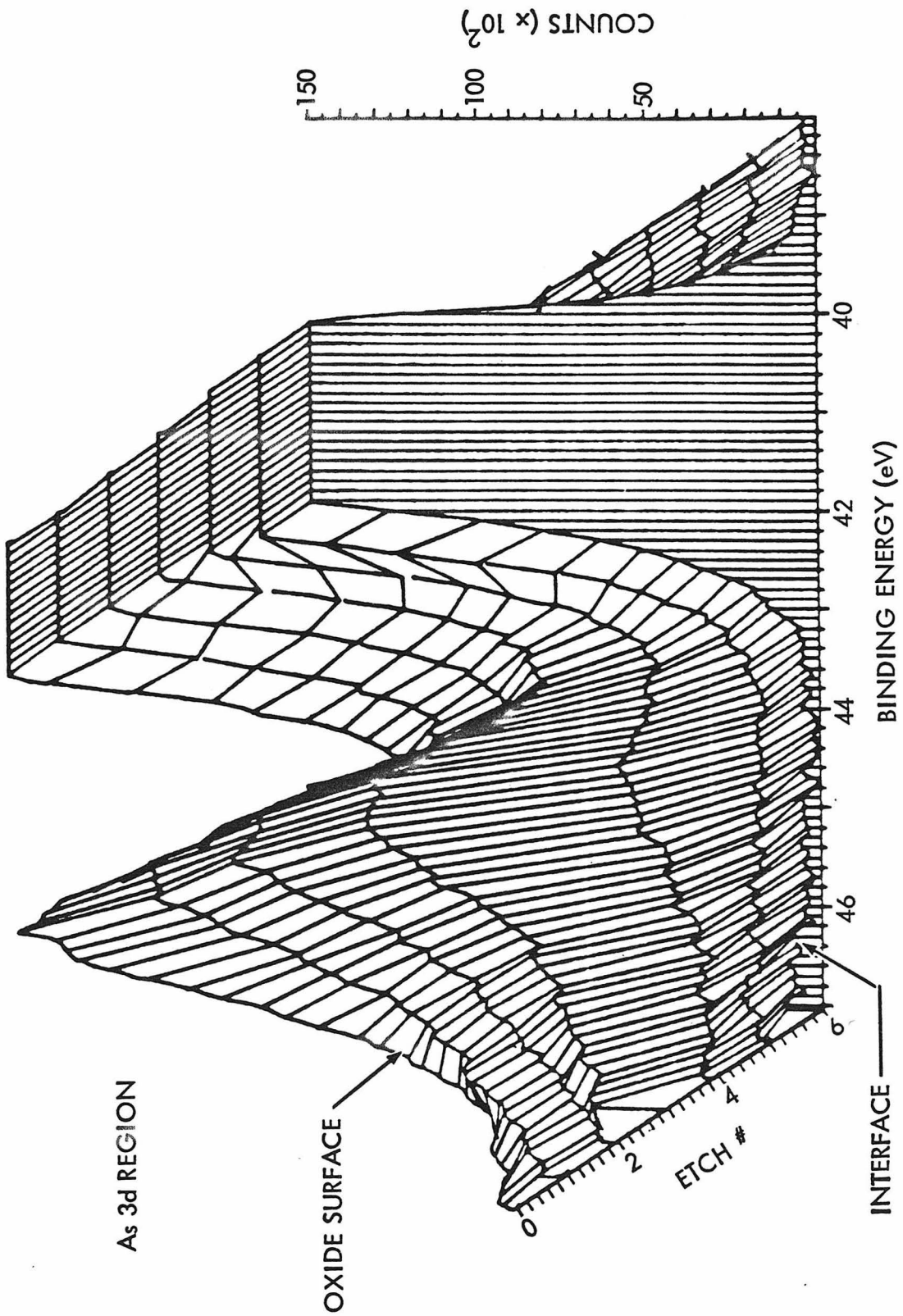
COUNTS (x 10²)
150
100
50
40
42
44
46
BINDING ENERGY (eV)
As 3d REGION
OXIDE SURFACE
INTERFACE
0
2
4
6
ETCH #

Figure 5

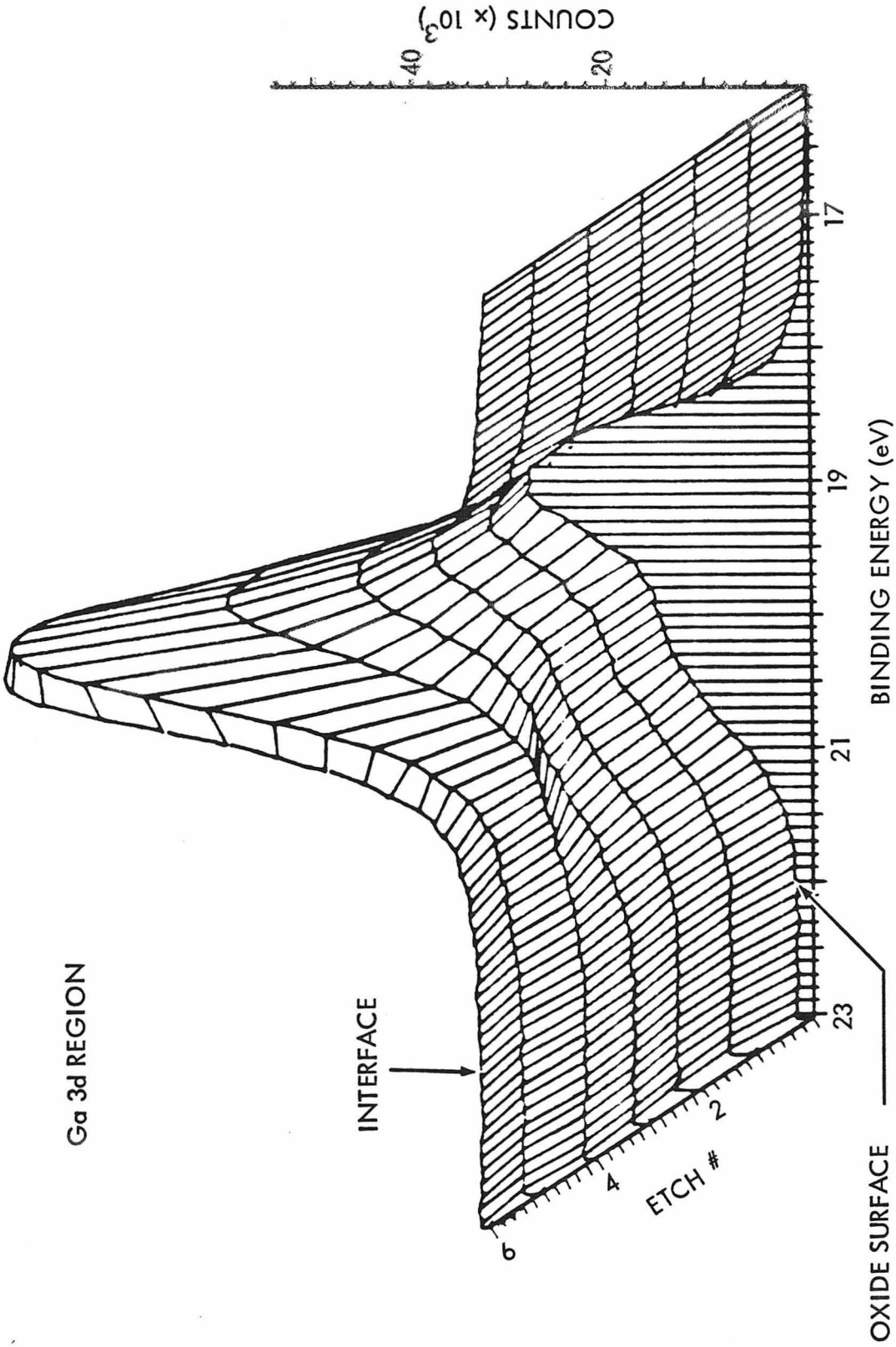
COUNTS (x 10³)
40
20
17
19
21
23
BINDING ENERGY (eV)
Ga 3d REGION
INTERFACE
OXIDE SURFACE
ETCH #
6
4
2

Figure 6

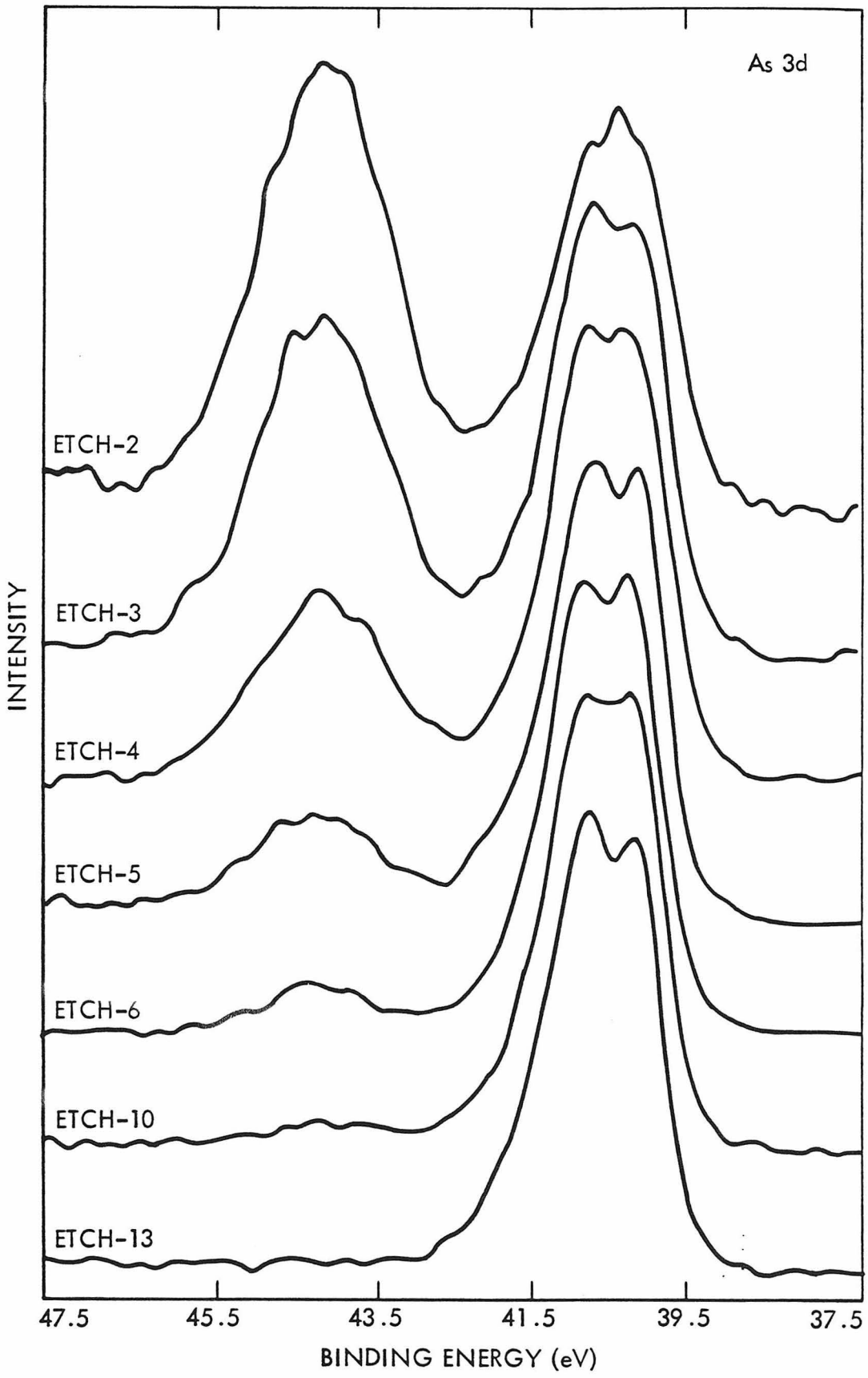
As 3d
ETCH-2
ETCH-3
ETCH-4
ETCH-5
ETCH-6
ETCH-10
ETCH-13
INTENSITY
47.5
45.5
43.5
41.5
39.5
37.5
BINDING ENERGY (eV)

Figure 7

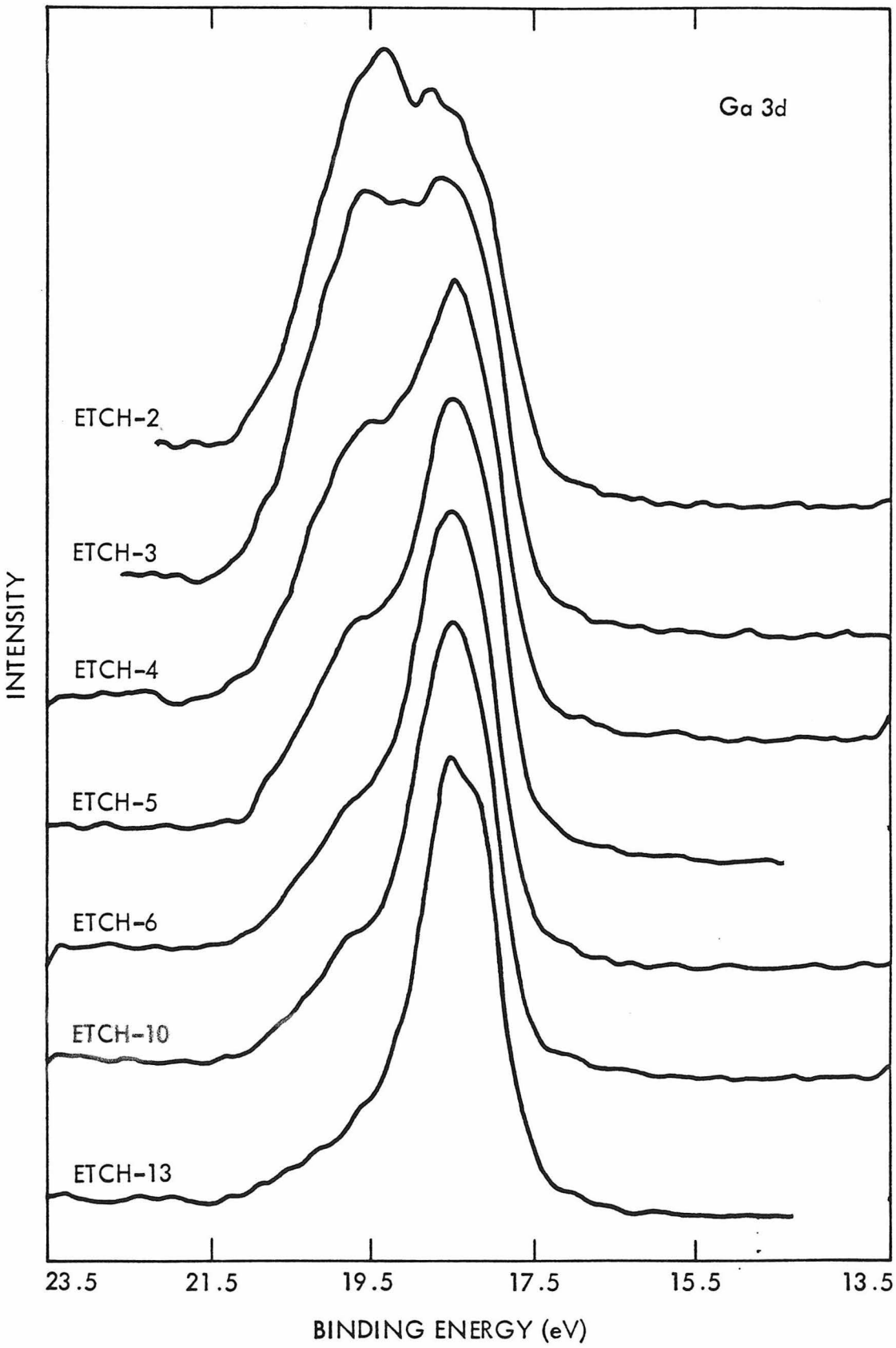
Ga 3d
ETCH-2
ETCH-3
ETCH-4
ETCH-5
ETCH-6
ETCH-10
ETCH-13
INTENSITY
23.5
21.5
19.5
17.5
15.5
13.5
BINDING ENERGY (eV)

Figure 8

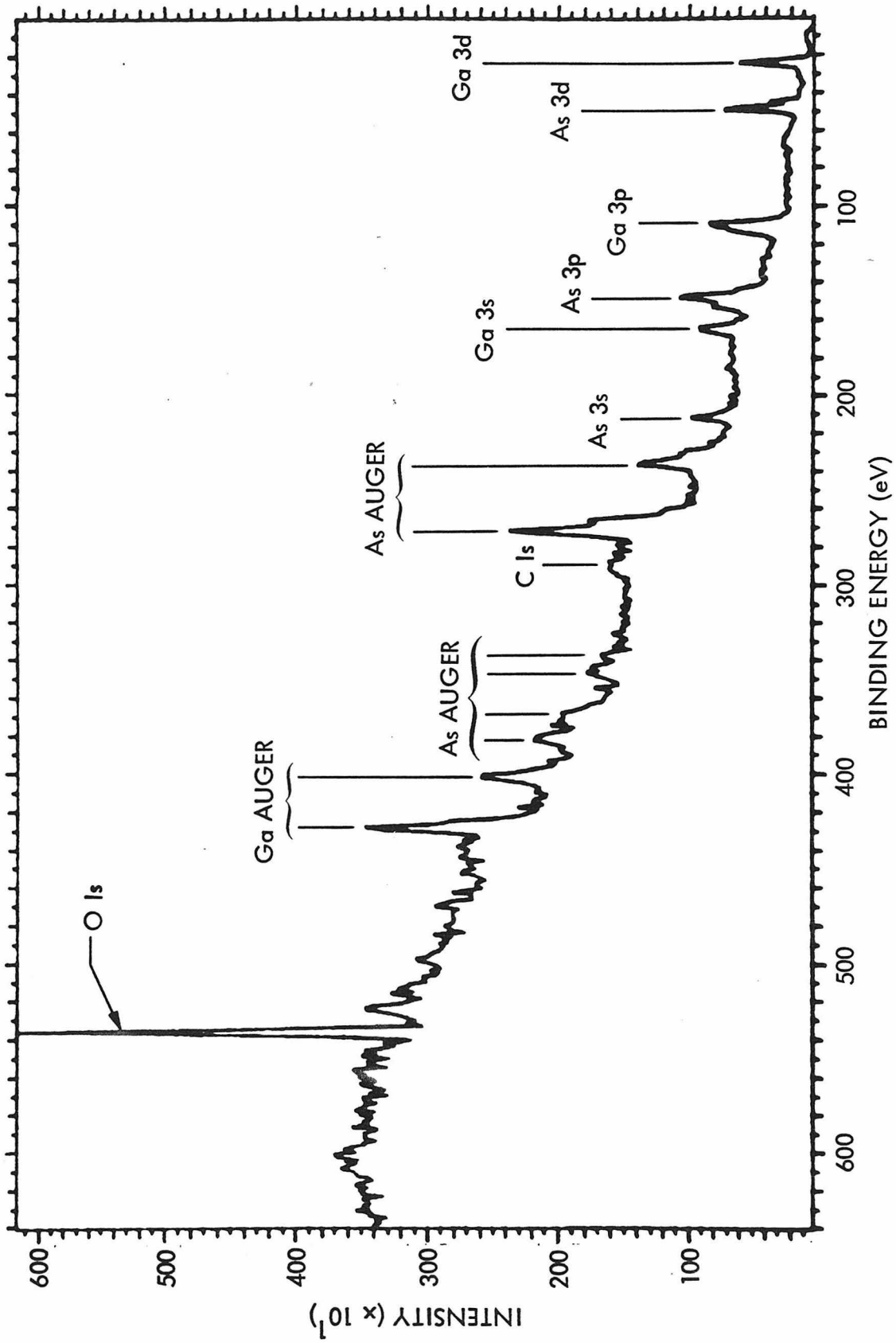
O 1s
Ga AUGER
As AUGER
As AUGER
C 1s
Ga 3s
As 3p
Ga 3p
As 3s
Ga 3d
As 3d
INTENSITY (x 10¹)
BINDING ENERGY (eV)
600
500
400
300
200
100
600
500
400
300
200
100

Figure 9

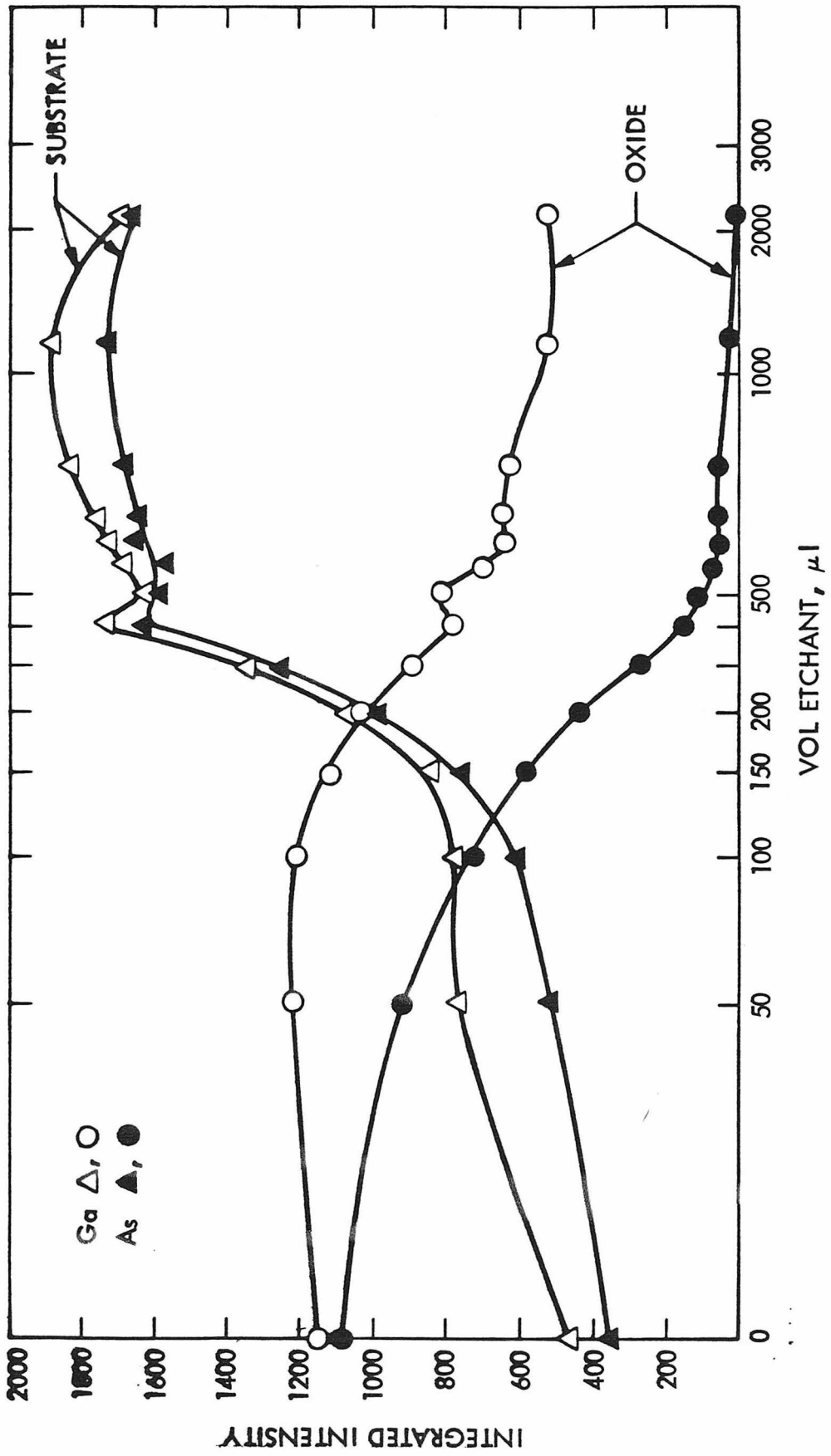
SUBSTRATE
OXIDE
Ga △, ○
As ▲, ●
INTEGRATED INTENSITY
VOL ETCHANT, μl
2000
1800
1600
1400
1200
1000
800
600
400
200
0
50
100
150
200
500
1000
2000
3000

Figure 10

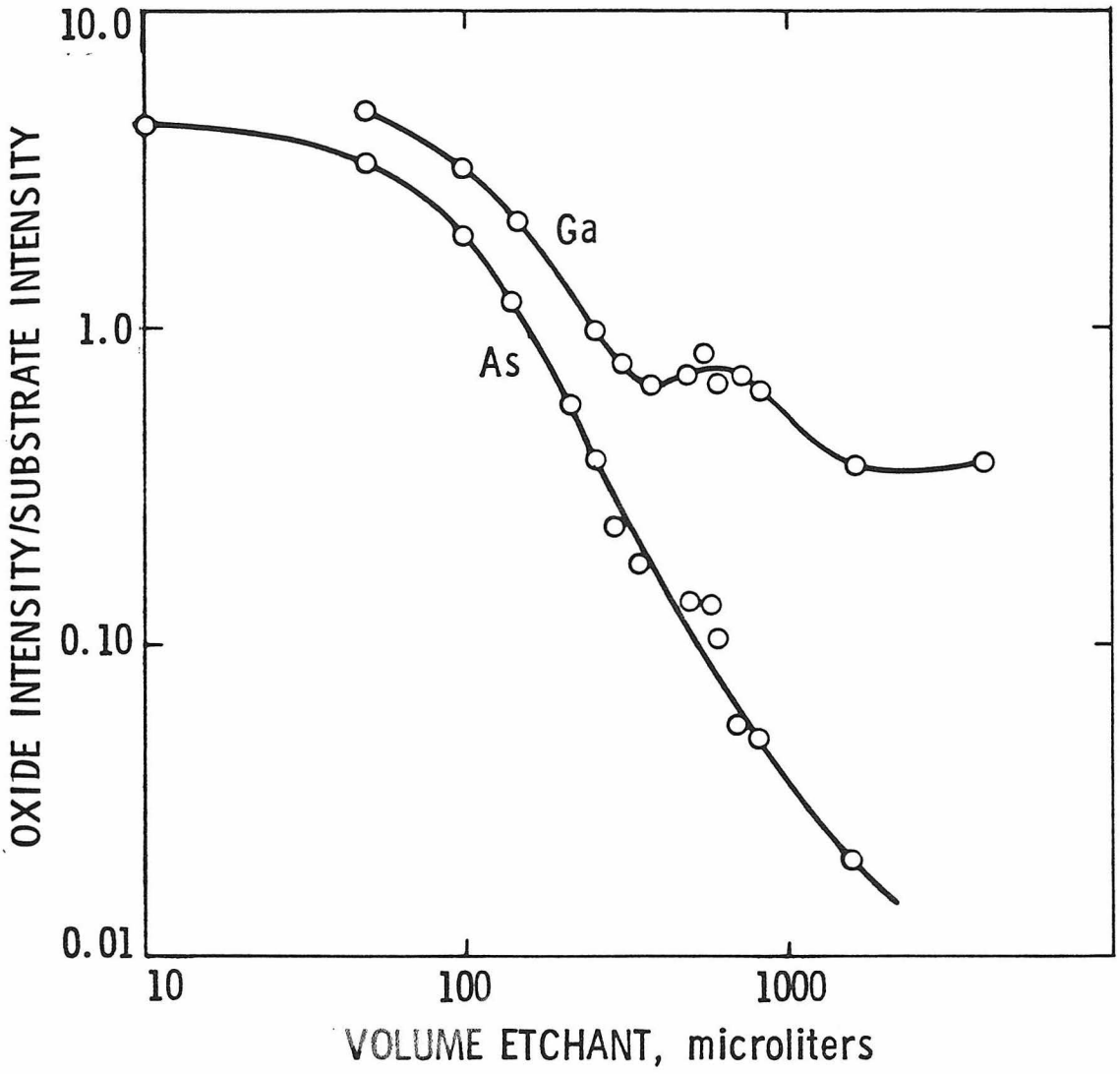
10.0
1.0
0.10
0.01
OXIDE INTENSITY/SUBSTRATE INTENSITY
Ga
As
10
100
1000
VOLUME ETCHANT, microliters

Figure 11

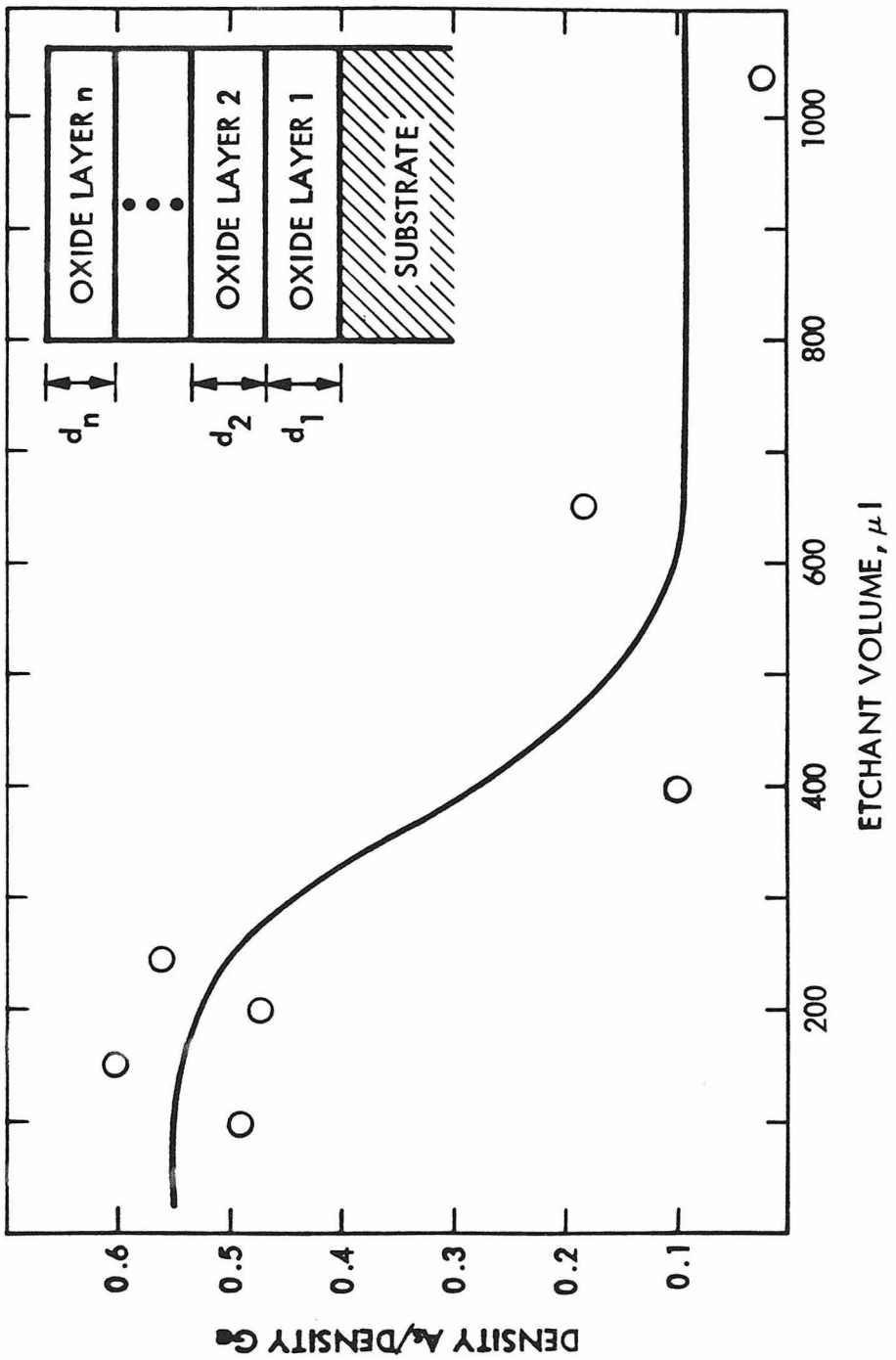
OXIDE LAYER n
OXIDE LAYER 2
OXIDE LAYER 1
SUBSTRATE
d_n
d_2
d_1
DENSITY A_s/DENSITY G_s
0.6
0.5
0.4
0.3
0.2
0.1
200
400
600
800
1000
ETCHANT VOLUME, μl

Figure 12

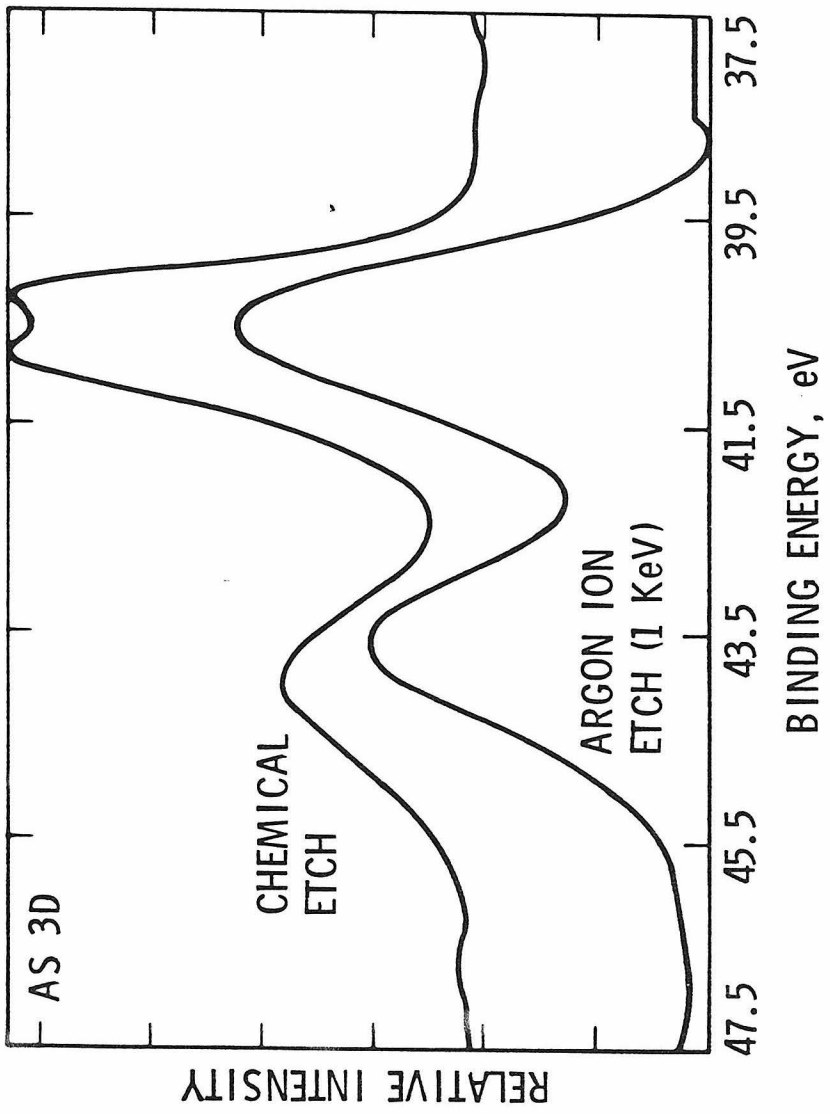
AS 3D
CHEMICAL ETCH
ARGON ION ETCH (1 KeV)
RELATIVE INTENSITY
47.5
45.5
43.5
41.5
39.5
37.5
BINDING ENERGY, eV

Figure 13

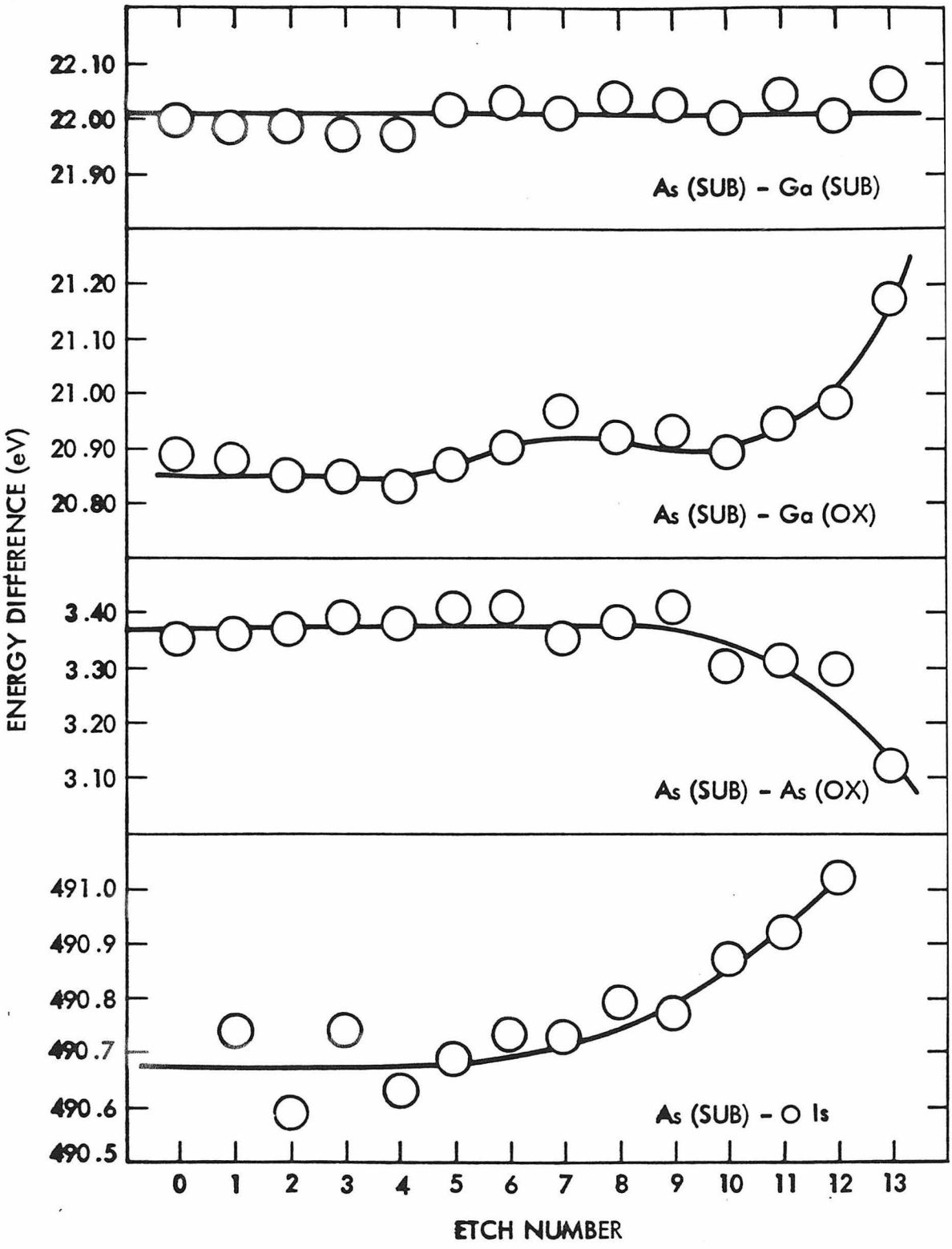
22.10
22.00
21.90
As (SUB) - Ga (SUB)
21.20
21.10
21.00
20.90
20.80
As (SUB) - Ga (OX)
3.40
3.30
3.20
3.10
As (SUB) - As (OX)
491.0
490.9
490.8
490.7
490.6
490.5
As (SUB) - O 1s
ENERGY DIFFERENCE (eV)
0 1 2 3 4 5 6 7 8 9 10 11 12 13
ETCH NUMBER

Figure 14

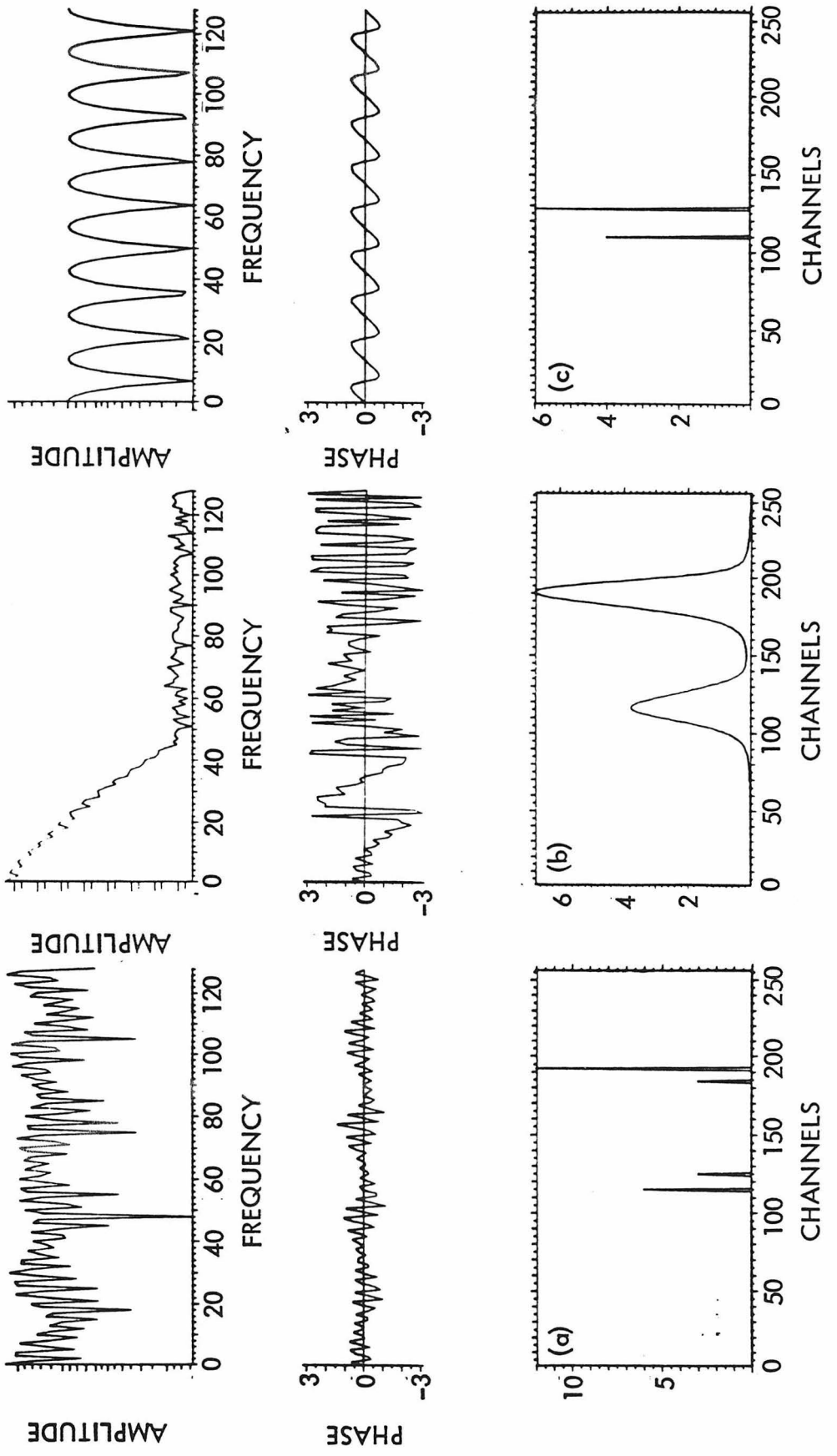

Figure 15

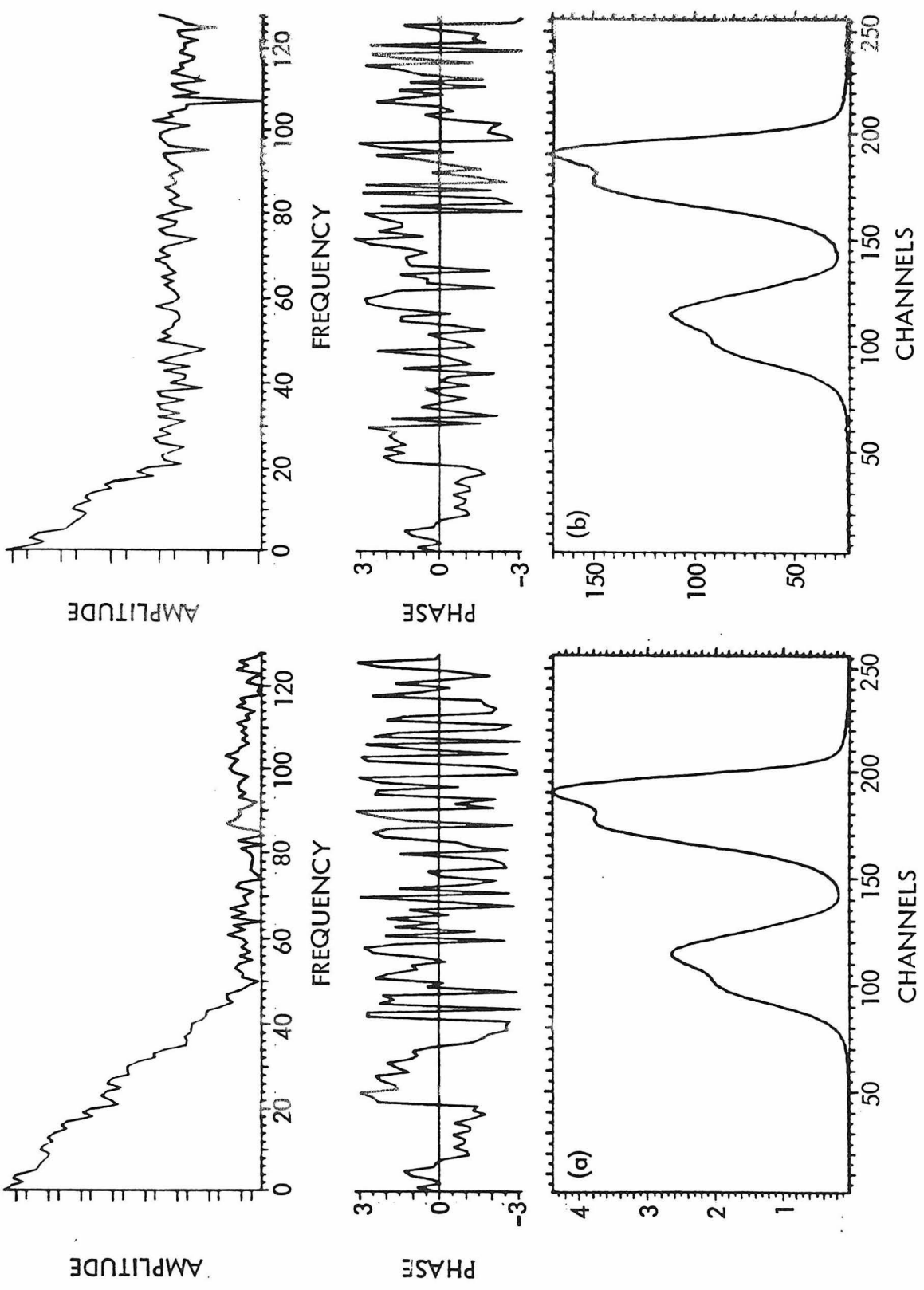

Figure 16

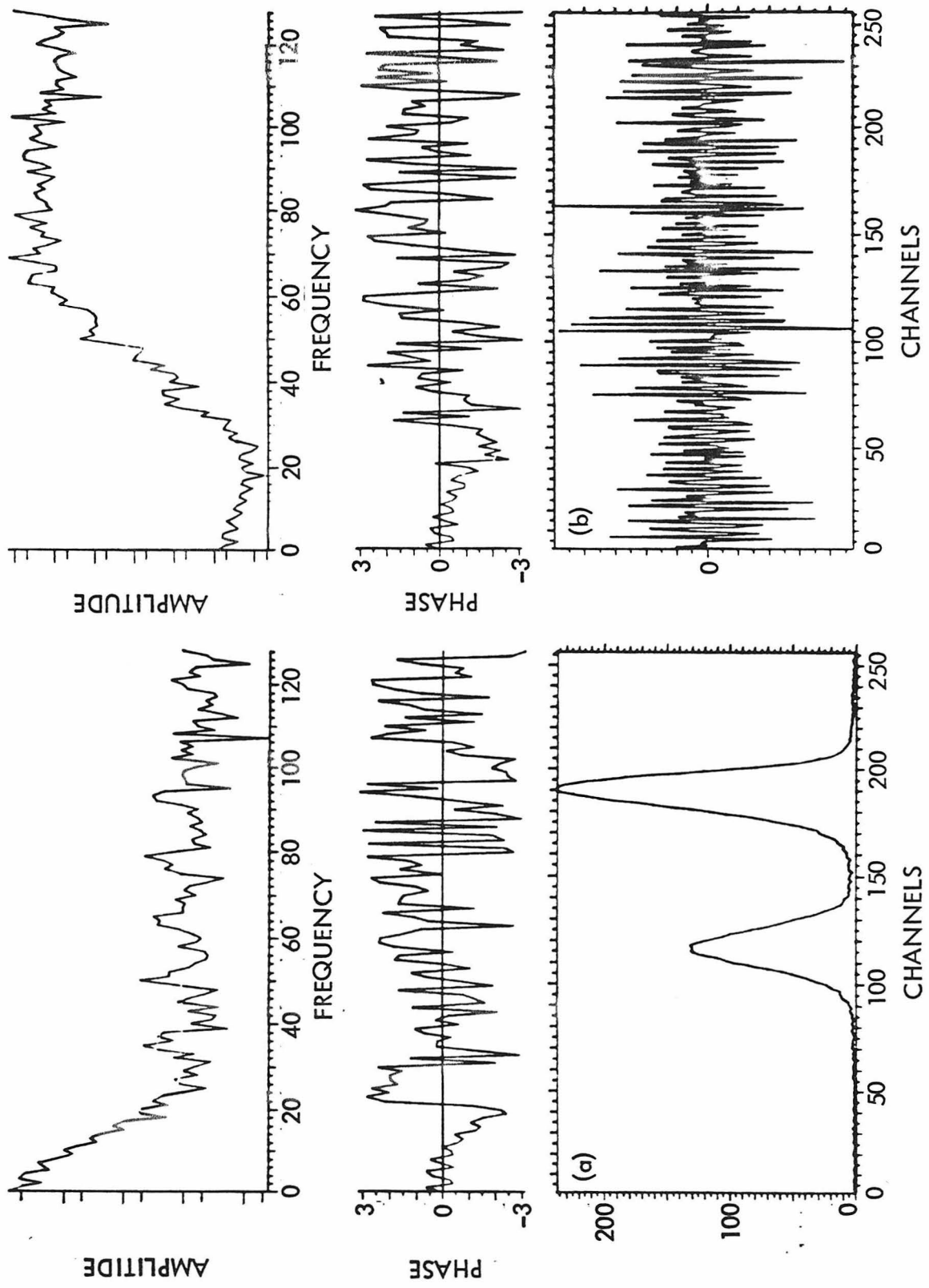

Figure 17

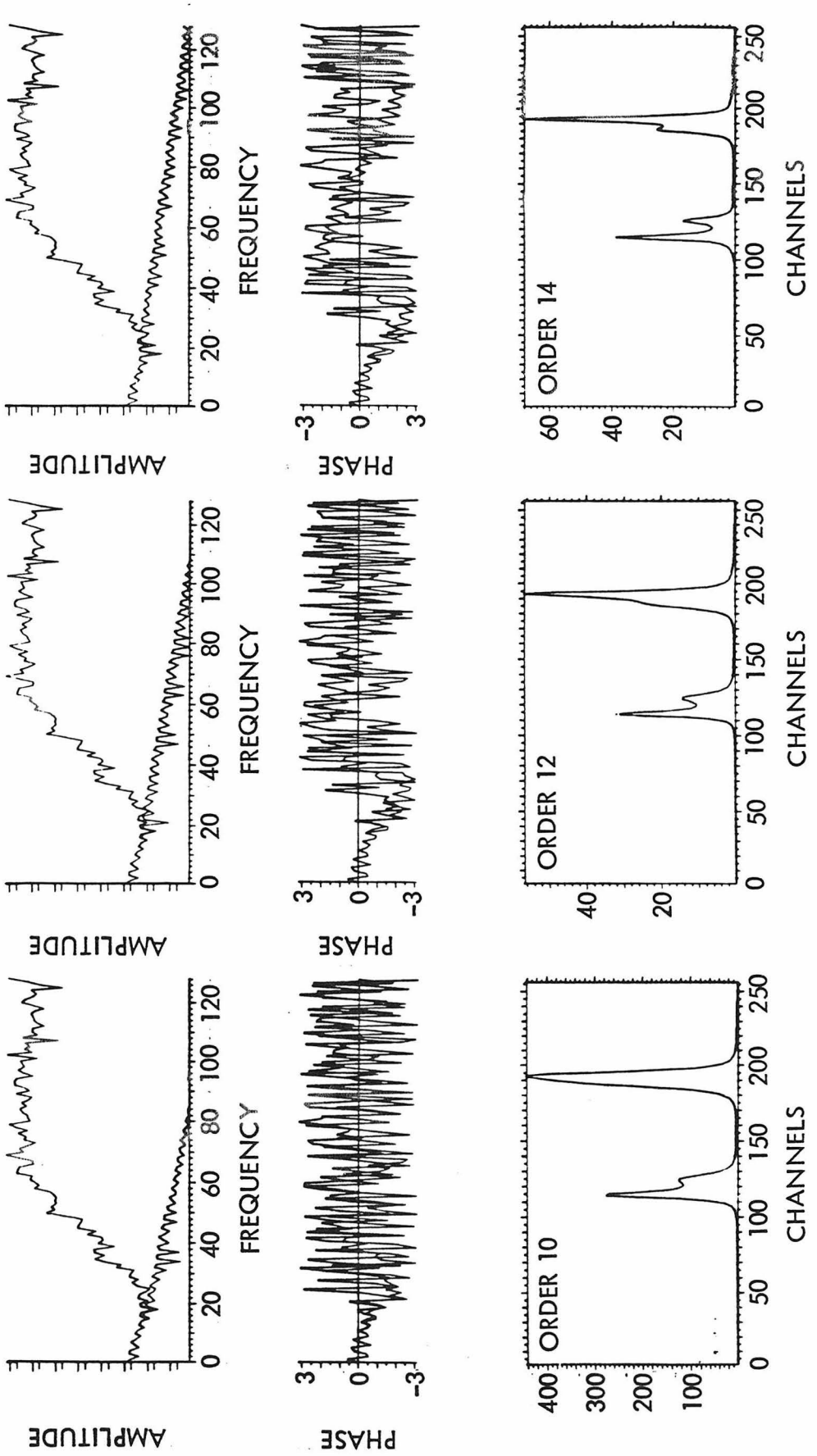
AMPLITUDE
FREQUENCY
PHASE
ORDER 10
ORDER 12
ORDER 14
CHANNELS

Figure 18

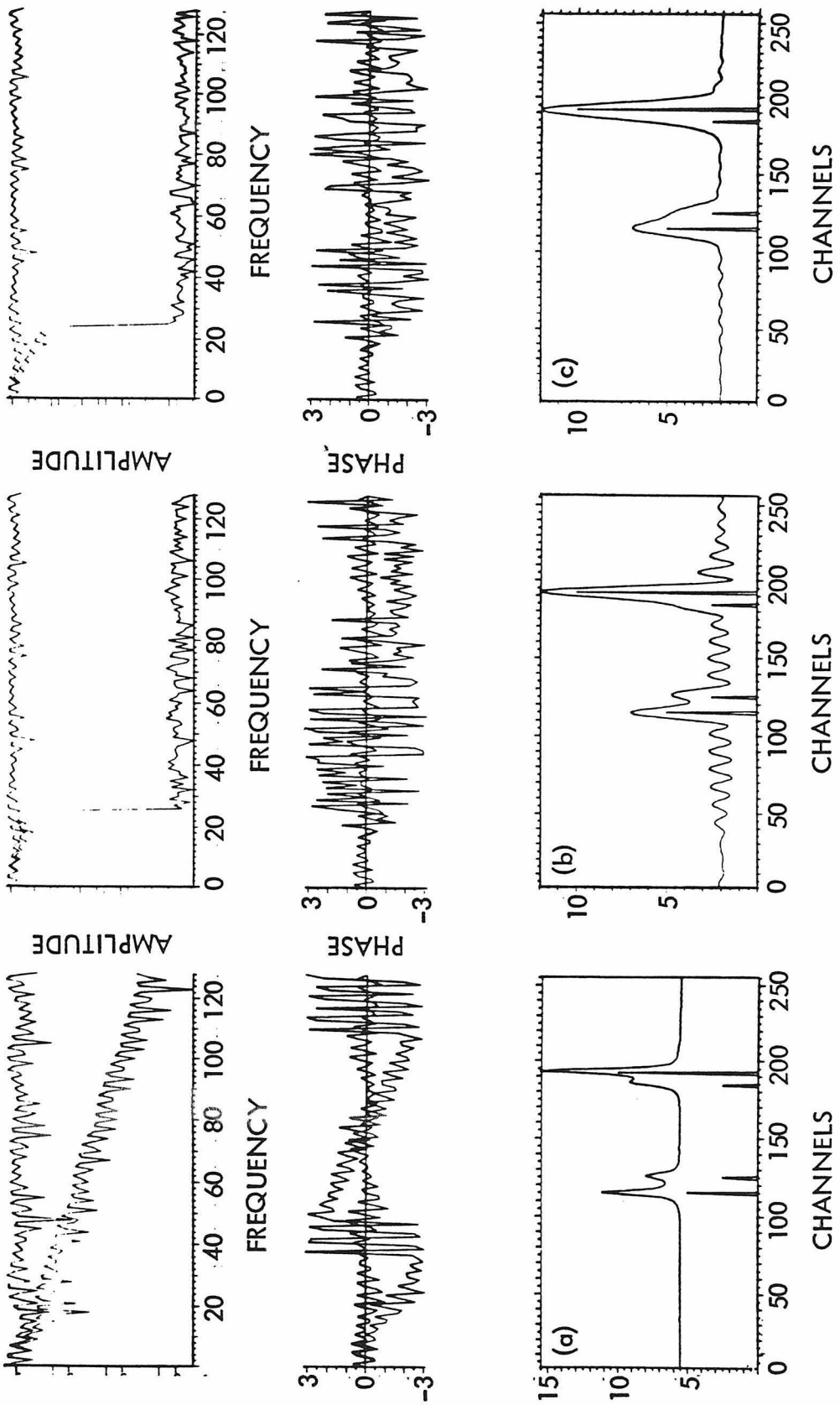
AMPLITUDE
FREQUENCY
PHASE
FREQUENCY
AMPLITUDE
FREQUENCY
PHASE
FREQUENCY
AMPLITUDE
FREQUENCY
(a)
CHANNELS
(b)
CHANNELS
(c)
CHANNELS

Figure 19

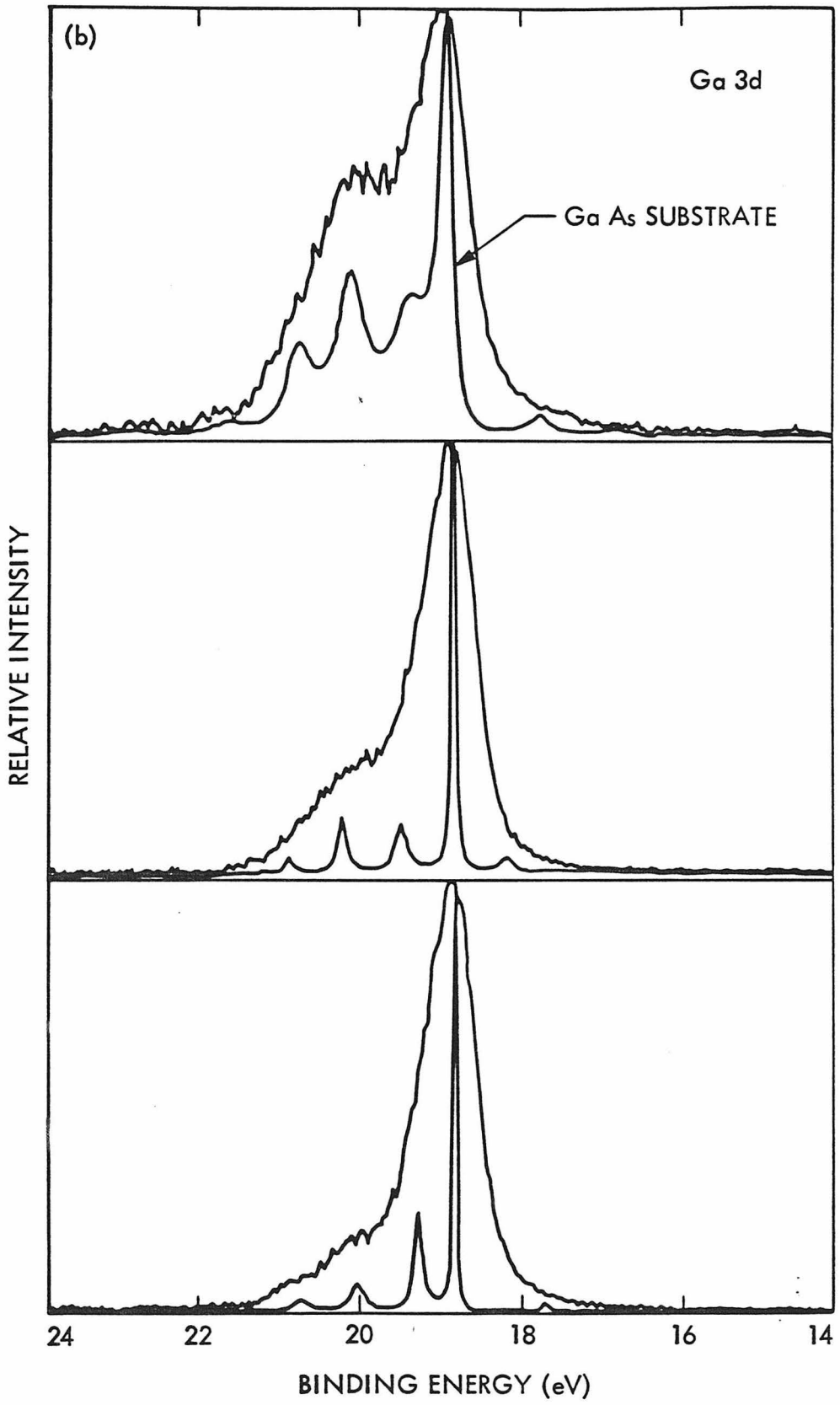
(b)
Ga 3d
Ga As SUBSTRATE
RELATIVE INTENSITY
24
22
20
18
16
14
BINDING ENERGY (eV)

Figure 20

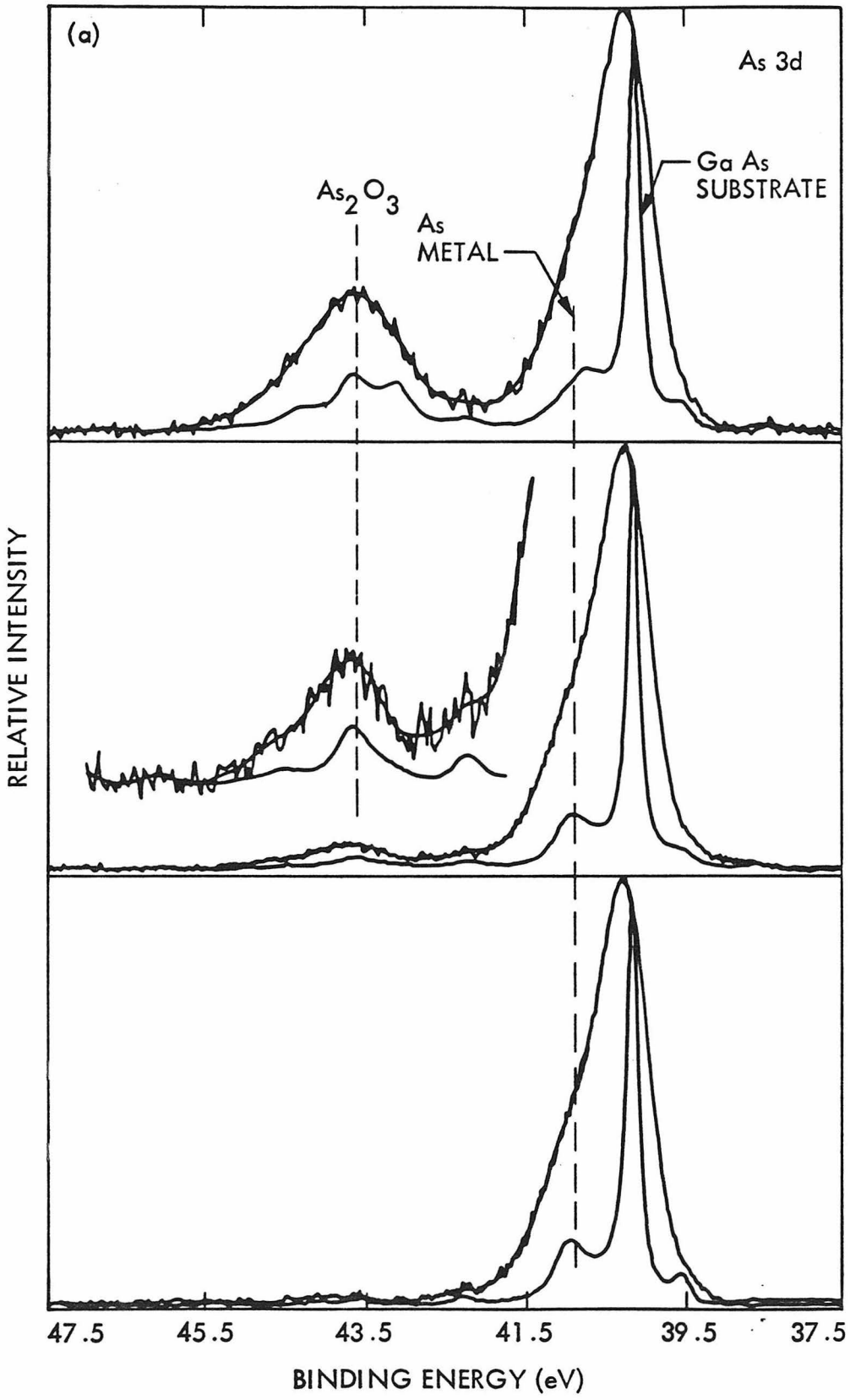
(a)
As 3d
Ga As
SUBSTRATE
As_2O_3
As
METAL
RELATIVE INTENSITY
47.5
45.5
43.5
41.5
39.5
37.5
BINDING ENERGY (eV)

Figure 21

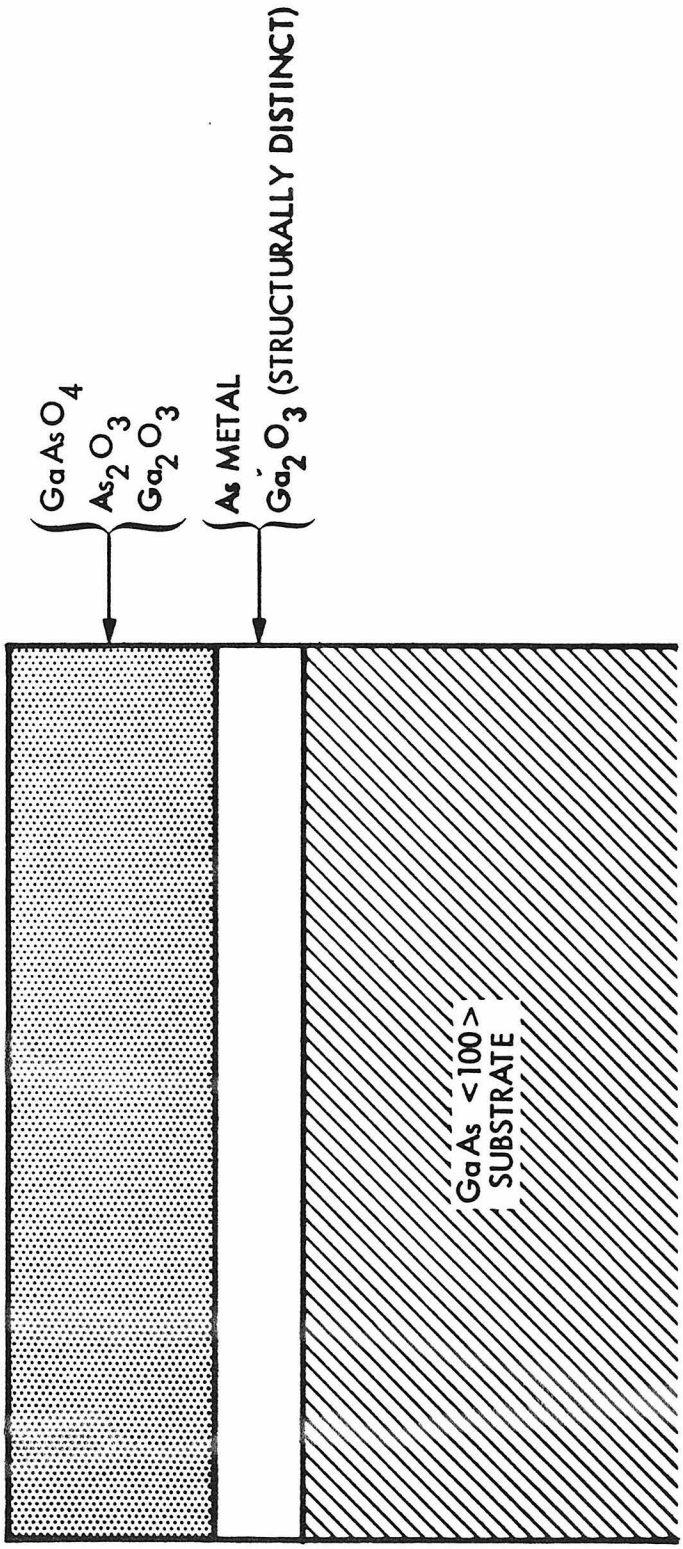
GaAsO4
As2O3
Ga2O3
As METAL
Ga2O3 (STRUCTURALLY DISTINCT)
GaAs <100>
SUBSTRATE

III. CHEMICAL BONDING CHARACTERISTICS OF TRANSITION METAL SILICIDES ON SILICON

CHEMICAL BONDING CHARACTERISTICS OF TRANSITION METAL SILICIDES ON SILICON

ABSTRACT

A systematic investigation of the bonding properties of selected transition metal silicides on single crystal Si substrates is proposed. $^{4}He^{+}$ backscattering, XPS, and x-ray excited AES will be used to characterize both the bulk and interfacial bonding properties. Initial experiments are presented to demonstrate the feasibility of the approach.

Introduction

The solid phase reactions of metal films with silicon have attracted a great deal of attention, both experimental and theoretical, in recent years. This great interest in metal silicide formation is due to their wide use in integrated circuit technology where they play a primary role in ohmic contacts and Schottky barrier formation in devices. Transition metal silicides provide the most reliable and reproducible metal-semiconductor contact of technological importance and thus have been thoroughly studied in terms of their formation kinetics and solid state reaction products. In addition, theorists are quite interested in the silicide/silicon interface since the extreme variety of different silicides provides a systematic variation of interface properties against which the theories of metal/semiconductor interfaces and Schottky barrier formation can be tested.

Adequate studies concerned with the fundamental nature of the chemical bonds within the silicides are lacking. It has become increasing clear that any theoretical treatment of metal/semiconductor interfaces will require consideration of the microscopic chemical properties of that interface.[1-2] Of equal importance is an understanding of the chemical features of the bulk silicides. Several studies have provided evidence of a connection between the bulk silicide bonding tendencies and interfacial properties. In particular, the work of Andrews and Phillips[3] has shown that the Schottky barrier heights of transition metal silicides on n-type silicon vary linearly with their enthalpy of formation. That the heat of formation is a bulk thermodynamic property while the Schottky barrier height is an interfacial property suggests ilucidation of the silicide/silicon interface will require an understanding of the chemical features and structure of the silicides themselves. Additional evidence for the connection between interface and bulk properties was provided in a study by Roth[4] using Auger spectroscopy. He observed that the predominant emission attributed to silicide/silicon interface states occurred at the same energy as one of the bulk silicide subpeaks. This suggested that the highest lying silicon-metal bonding states are a common feature linking the bulk and interface characteristics.

An increasing number of experiments continue to emphasize the need for inclusion of chemical bond information in theoretical models of metal/semiconductor junctions. Yet, aside from the Auger study by Roth, no other spectroscopic data is available on the silicides and the fundamental understanding of their chemical properties remains very primative.

Moreover, apart from the technological significance of the silicides, a study of such solid state reactions is of interest in its own right. Silicon reacts with almost every transition metal to form an extensive variety of different silicides and many of these can be obtained in different stable phases. Such an array of chemically related compounds presents the opportunity to investigate the bonding in metal-nonmetal systems because it allows many different avenues of approach to the problem. A systematic variation of the transition metal across a row or down a group of the periodic table would allow one to investigate the effects of metal d-orbital occupation or spatial distribution of the d orbitals on the bonding characteristics. Though potentially a very complex subject, the variety of silicides should allow for sufficient compilation of data to identify trends and correlations in the bonding tendencies.

Thus two compelling justifications exist for an examination of the solid phase reaction of metal films on silicon — (1) they are technologically important and (2) they are of academic interest. These two reasons provide the primary motivation for undertaking a systematic spectroscopic investigation of the bulk as well as the interfacial bonding characteristics of transition metal silicides on silicon.

APPROACH AND OBJECTIVES

INSTRUMENTAL TECHNIQUES

The investigation proposed here will employ three complementary instrumental techniques to probe the chemical structure of the transition metal silicides and their interfaces. These techniques are Rutherford backscattering spectroscopy (RBS), photon induced Auger electron spectroscopy (AES), and X-ray photoelectron spectroscopy (XPS). Any scientific study has much to gain from a combination of tools since any given technique can only yield information peculiar to the particular physical phenomenon that it monitors. Each technique will have its limitations and only through a combination of tools can a system be fully characterized. The three techniques mentioned above will be only briefly described here so that one may understand the basic kind of information available from each. Excellent detailed treatments of RBS[8], XPS[9], and AES[10] may be found elsewhere.

RBS is ideally suited to complement the information obtained from XPS and AES. It provides quantitative information on the depth distribution of atomic species through a kinematic consideration of the scattering of incident mono-energetic ions off atoms within a solid. Through an analysis of conservation of energy and mass equations, different atomic masses can be easily determined from the different backscattered energies. The capacity for depth perception is due to the fact that, in addition to the energy loss suffered from elastic collisions with atoms in a solid, ions traversing a solid lose energy through electronic interactions. In thin films, this energy loss is approximately linear with thickness. Quantitative analysis of atomic composition is possible since extensive compilations of scattering cross section data now exist. These scattering cross sections measure the probability that an elastic two-body collision between a projectile and a target nucleus will occur. Thus, through analysis of the scattered ion energy, and a knowledge of the relevant scattering and stopping cross sections, one may quantitatively determine the atomic

composition of a solid as a function of depth. The limitation of RBS is the total absence of any chemical information. In this aspect, however, XPS and AES have much to offer.

In XPS, one analyses the kinetic energy of electrons ejected when a solid is irradiated with monochromatic photons. To a first approximation this kinetic energy is a measure of the energy with which the electron was bound in the solid. The exact value of the binding energy for a given element depends on the chemical environment of that element. The reason for this is easy to understand. If we consider a core level, the energy of an electron in this core state is determined by the repulsive core Coulomb interaction with the other electrons and the attractive potential of the nuclei. Any change in the chemical environment of the element will involve a spacial redistribution of the valence charges of this particular element and the creation of a different potential from the electrons and nuclei of the other elements around it. Thus, XPS directly supplies information about the chemical nature of atoms within a solid. It is a surface technique, however, in that it probes only the first 10-100 Å of a sample.

The Auger effect monitored in AES is the radiationless de-excitation of an atom initially ionized in one of its inner shells. This initial ionization can be accomplished either by electron impact (this is normally how it is done) or by X-ray excitation. The study proposed here will use photon excitation since it can be performed with the same instrument as the XPS and because it will circumvent some of the problems encountered with electron impact ionization that will be discussed later. The ionization of an inner shell of an atom can produce a transition wherein an electron from a higher lying orbital fills the inner core hole. The energy liberated during this process ejects a second electron from the atom and this electron is termed an Auger electron. Normally AES is used in a "fingerprint" fashion to identify the kinds of elements present in a sample, but recently Roth[4] has demonstrated that at least in the case of the transition metal silicides there is some chemical information contained in the lineshape of the Si_{LVV} Auger line. The Auger lines also display chemical shifts and, in some cases, it has been shown that the chemical shift of the Auger peak is greater than the chemical shift of the XPS peak. Thus, the inclusion of AES

will provide valuable chemical information to supplement the XPS and allow a comparison to and extension of the results of Roth.

The major limitation in both XPS and AES is their inability to provide quantitative information. As discussed earlier RBS will fill this gap and allow one to avoid the ambiguities that arise from not knowing how far the solid state reaction has progressed or what stoichiometic phase is present. This will become particularly important later where one proposal is to dynamically monitor the reaction interface.

Characterization of Bulk Silicides

The chemical characterization of the bulk transition metal silicides will involve examination of core and valence electron binding energies with XPS as well as the metal derived and silicon derived valence band Auger transitions. As explained earlier, the binding energy of core level states respond to the changes of electron density around the atom and thus sense the charge transfer between atoms. In addition to the core states it is possible to monitor electron emission from the occupied valence levels and this yields information on the energy distribution of electrons participating in the chemical bonds. It is important to monitor the valence level in addition to the core levels since small changes in the energy distribution of the valence electrons can be sensed which may not cause significant enough spacial redistribution of charge to cause core level shifts.

The only spectroscopic study of the chemical nature of the silicides has been that by Roth, as previously mentioned. By examining the lineshape of the Si_{LVV} Auger transition in a variety of transition metal silicides he concluded that significant chemical state effects may be seen in the silicon derived valence band transitions. In particular, he observed that the silicides formed with transition metals from Group VIII of the Periodic Table produced Si_{LVV} lineshapes least like that found in pure silicon. This suggests the metal-silicon bonds within these compounds are different from the Si-Si sp^3 hybridized bonds of pure Si. In contrast he found little difference between the Si_{LVV} from

Nb, Ti, V and Zr (Groups IVB and VB) and pure Si, suggesting these metal-silicon bonds must be very similar to the covalent Si-Si bond. He also noted identical Si_{LVV} lineshapes for the two phases PtSi and Pt_2Si. This is somewhat unexpected given that Si exists in different site geometries in the two phases. Perhaps the finer detail of atom arrangements and chemical shifts in the Groups IVB and VB silicides are beyond the scope of an Auger lineshape analysis because of the averaging caused by the self-convoluting nature of the Si_{LVV} Auger line. XPS lines do not suffer from such a self-convolution and thus will hopefully be able to provide more detailed chemical information.

Roth also attempted to study the metal derived Auger transitions (that is, those transitions where the initial ionization occurs in a metal core level). Workers in the past[11-12] have reported that no significant chemical effects are observable on such metal derived lines. This, however, seems unreasonable in the light that such effects are seen on the silicon derived Auger lines and, in fact, Roth was able to find observable differences in the Pd and Pt Auger lines. The differences are difficult to observe, however, since the metal derived lines (which occur in the 15-35 eV range) lie close to a large slow secondary electron peak. He suggests that this possibly accounts for his inability (as well as the inability of the earlier workers) to observe chemical effects. By using X-ray excitation to produce the initial ionization instead of electron impact, we avoid the problem of the large secondary electron peak. Consequently, the metal derived valence Auger transitions may be used for additional chemical information.

Considering the above, this study proposes to characterize the chemical bonding tendencies in selected silicides through an examination of the core and valence spectra obtained from XPS in addition to the silicon and metal derived Auger transitions. All measurements may be made in the same instrument under UHV conditions, thus avoiding ambiguities that arise from contamination because of sample transfer. The silicides themselves will be prepared by e-beam deposition of metal films on single crystal silicon and then grown "in situ" under UHV conditions. This provides control over ambient contamination. After analysis with the electron spectroscopies, samples will be characterized with RBS for identification of the silicide phase. X-ray diffraction will also be utilized

for positive compound identification. Based on the results of Roth, it is proposed that the study initially concentrate on those silicides formed from the transition metals from the last column of Group VIII (Ni, Pd, Pt) and those in Group IV (Ti, Zr, Hf). The study will be extended to additional transition metals as time permits.

Interface Characterization

After characterization of the bulk silicide properties it is desirable to extend the analysis to those chemical bonds formed in the vicinity of the metal/silicide and semiconductor/silicide interfaces. This is largely motivated by the growing body of experimental and theoretical results suggesting that the chemical nature of the interface plays a role in formation of the Schottky barrier at metal/semiconductor interfaces.[1-3,5-7,13] It is proposed in this study that two fundamentally different approaches be used to investigate the silicide/silicon interface.

(1) Thin Metal Film Deposition

The first approach is to perform sequential in situ depositions of thin metal films on single crystal silicon and monitor the chemical development of the interface with XPS/AES. Prior to deposition the initial silicon surface may be cleaned by sputter etching with argon ions and subsequently annealed to yield an essentially contaminant free surface. (It would be interesting, time permitting, to repeat these deposition experiments with silicon surfaces that had been purposely and controllable contaminanted in situ with, say, oxygen to determine the effect of contamination on the kinetics of silicide formation.) Since the mean free path of electrons from the Si 2p photoemission line is approximately 20 Å in metals, one can still monitor the chemical state of the silicon after as much as perhaps 50 Å of metal have been deposited. Electrons from the Si_{LVV} and low energy metal derived Auger lines have mean free paths of 5-7 Å and thus they can be monitored only up to approximately 15-20 Å of metal. This ability to "look through" the metal layer is quite significant. It allows one to examine the silicon/metal interface not only when there are just a few monolayers of the metal present, but also when there is a substantial amount of the silicide present. This is important, since the presence of a

silicide (or metal film) may impose different bonding restrictions on the interface atoms than the presence of a vacuum. The entire deposition experiment can be performed with the sample at room temperature to monitor the "as deposited" metal/silicon interface or at elevated temperatures to monitor the silicide/silicon interface.

The limitation to this approach is that the metal must be amenable to tungsten filament evaporation because of instrumental technicalities. The Ni, Pd, and Pt silicides may be examined with the thin film approach but not the Ti, Zr, and Hf silicides since these metals require boat or e-beam evaporation.

(2) Dynamic Monitoring of the Interface

The "look through" feature of XPS and AES discussed above makes possible a second and perhaps procedurally simpler approach for the investigation of the interfacial bonding regions. It involves continually monitoring a metal film on single crystal silicon while it is being heated to form the silicide. To illustrate the procedure, consider the reaction of a nickel film on silicon. RBS studies[14] have shown that silicide formation generally proceeds as diagrammed in Figure 1. The first phase, Ni_2Si in this case, forms at the metal/silicon interface as shown in 1(a). With continued heating, the width of the silicide region increases and the width of the Ni region decreases correspondingly (Figure 1(b)). Once the nickel film has been completely consumed, a second (less metal rich) phase can develop at the Ni_2Si/Silicon interface (Figure 1(c)). Formation of this next phase generally requires a higher temperature than the initial phase. The second phase continues to increase in width at the expense of the first phase (Figure 1(d)) until the first phase is entirely consumed (Figure 1(e)). A third silicon rich phase $NiSi_2$ may begin to develop at the NiSi/Si interface if the temperature is elevated even further and this phase will also proceed as above to consume the NiSi phase. During the various phase growths, two phases coexist but usually as discrete layers as shown in the figure.

This progression of phases allows one to examine the various interfacial regions by utilizing the finite information depth of XPS and AES. This finite information depth is due to the mean free path of electrons in solids as

discussed previously. Assume, for example, that the maximum depth from which electrons can emerge is as indicated in Figure 1. Then, in the situation diagrammed in 1(a) only the metal signal will be observed. Eventually, as the reaction proceeds, the silicide layer will come within the information depth, as in 1(b). The first silicon photoelectron signal will be observable at this point and it will necessarily be from those silicon atoms present at the metal/silicide interface. The sample may be cooled at this time to prevent the reaction from continuing during data acquisition. By reheating the sample and repeating the above procedure, XPS and AES spectra may be obtained from each of the regions shown in Figure 1 (a-e).

Not all of the metals to be initially studied form as many stable phases as Ni.[16] Zr forms only the disilicide phase, $ZrSi_2$. Ti and Hf both first form the monosilicide phase, MSi, and convert to the disilicide MSi_2 phase with extended heating. $HfSi_2$, however, grows in random islands throughout the HfSi instead of in a uniform layer, making its study unfeasible. The metals Pt and Pd form first as M_2Si. Pt_2Si may be converted to PtSi with heating, but Pd_2Si breaks into islands when PdSi is formed.[17] Thus, only the phases Ni_2Si, NiSi, $NiSi_2$, $ZrSi_2$, TiSi, $TiSi_2$, HfSi, Pt_2Si, PtSi, and Pd_2Si are suitable for study.

In exactly the same fashion as described above, one may also examine the silicon/silicide interfaces by spectroscopically viewing the reaction through the silicon layer instead of the nickel. This is made possible by a procedure that allows one to obtain single crystal silicon that is only $\sim$2000 Å thick.[15]

The major advantage of this method of dynamically monitoring the interface is that all measurements are made on the same sample and thus one avoids the referencing problems that plague XPS. It also allows examination of the interface in its "native habitat"; that is, with an extended solid on each side. And, finally, it allows examination of the interface without the perturbation caused by any of the commonly used depth profiling methods such as ion sputtering or chemical itching.

The disadvantage to the approach is the unknown roughness of the interface. Any interfacial study suffers from this unknown unless extensive TEM studies are made. However, Roth examined the silicide/silicon interface with Auger sputter

profiling and thin film deposition and found evidence of distinctive interface chemical bonding.[4] It would appear, then, that the interface regions formed with at least the Group VIII, IV, and V metals are defined enough that one does not lose the interface signal due to spatial averaging over a large area.

INITIAL EXPERIMENTS

Initial experiments have been performed to demonstrate the feasibility of examining the interfacial bonding regions by dynamically monitoring the thin film reactions as described above. Amorphous Si films rather than crystalline Si substrates were used for these requirements.

Experimental

Thermally oxidized Si wafers ($\sim$1000 Å SiO_2, 1000°C) were used as substrates for the deposition of thin Ni and Si films. Prior to being loaded into the vacuum system for evaporation, the SiO_2 substrates were cleaned with TCE, acetone, and methanol and then rinsed in deionized H_2O. A vacuum of better than 5×10^{-7} Torr was maintained during evaporation. $\sim$1500 Å of Si followed by $\sim$1000 Å Ni was deposited on one substrate (Si/Ni sample). The remaining substrate received $\sim$1500 Å Ni followed by $\sim$1000 Å Si (Ni/Si sample)

Prior to examination by XPS, the nickel oxide that formed on the surface of the Si/Ni sample during transport was removed. This oxide layer was etched off under a N_2 atmosphere by spinning the sample at 3600 rpm and then adding dropwise 500 µl of 1:1 HCl in ethanol, followed by 500 µl of ethanol. The SiO_2 layer that formed on the Ni/Si sample was removed by 1:10 HF in ethanol using the same spinning procedure.

The samples were heated to 275°C in the analyzer chamber of the XPS spectrometer to grow the silicides. The vacuum inside the chamber during heating was better than 2×10^{-9} Torr. The samples were cooled to 298°C at various intervals to allow for extended data accumulation periods.

Results

Nickel/Silicide Interface

By monitoring the Si/Ni sample as a function of time during silicide formation, one is able to examine the Ni/silicide interface as it advances forward. The initial removal of the contaminant NiO overlayer is extremely important since not only does it attenuate the Ni metal photoelectron signal, it will also obscure any chemical shifts that occur upon silicide formation. Figure 2 compares the nickel surfaces before and after the HCl/ethanol etch. Notice in 2(b) that there is negligible NiO remaining and that the Ni metal signal has increased ∿2-1/2 times in intensity. A small amount of carbon and residual oxygen were the only detectable contaminants.

After establishing an oxide free nickel surface, various Si and Ni core and valence levels were monitored as the sample was heated to 275°C. In Figures 3 and 4 are plotted the Si 2p and Ni $2p_{3/2}$ spectra, respectively, obtained at the various stages of silicide formation. In 3(a), the silicide/nickel interface front has not advanced far enough for the Si to be within the sampling depth of the spectroscopy. Thus, no Si 2p signal is observed at this point. The corresponding Ni $2p_{3/2}$ signal (pure Ni metal) is shown in 4(a). With continued heating, the reaction front advances far enough that the first Si 2p photoelectrons may be detected as shown in 3(b). Continued heating produces the Si 2p spectra 3(c) - 3(e), with the corresponding Ni $2p_{3/2}$ spectra 4(c) - 4(e). In the final spectra, 3(e) and 4(e), the thin film has completely reacted and consumed all the nickel metal to form Ni_2Si, as determined from the $^4He^+$ backscattering spectrum in Figure 5. Some NiSi has formed at the Si/silicide interface but the layer is not thick enough to be within the XPS sampling depth. Notice that the first Si 2p signal appears approximately 0.6 eV lower in binding energy than the Si 2p from Ni_2Si. The signal progressively shifts to higher binding energy until it reaches the bulk Ni_2Si binding energy of 99.3 eV. The Ni $2p_{3/2}$ signal concurrently shifts 0.8 eV upfield from its value of 852.5 eV in Ni metal to 853.3 eV in the bulk silicide Ni_2Si. The satellite structure accompanying the Ni $2p_{3/2}$ line also decreases in intensity and appears to shift to higher binding energies relative to the main Ni line.

One would expect the Si 2p binding energy to decrease in the order $Si > NiSi_{x>2} > NiSi_2 > NiSi > Ni_2Si > Ni_{x>2}$ Si. The Ni 2p should decrease in the order $NiSi_{x>2} > NiSi_2 > NiSi > Ni_2Si > Ni_{x>2}$ Si $> Ni^{o}$. The fact that the first Si 2p signal detected appears at a low binding energy and gradually shifts upfield as the bulk Ni_2Si is formed suggests that the interfacial silicon atoms are in a more Ni rich coordination environment than the Si atoms in Ni_2Si. This is what one would expect intuitively. The apparently continuous shifts of the Ni 2p and Si 2p lines are more suggestive of a compositional gradient than an abrupt boundary. This gradient appears to occur over $\sim$20 Å.

Silicon/Silicide Interface

The advance of the Si/silicide interface may be examined by monitoring the silicide reaction through the Si film of the Ni/Si sample. After establishing an essentially contaminant free Si surface, the sample was heated in situ to 275°C and monitored with XPS as described for the previous sample. In Figures 6 and 7 are plotted wide energy scans displaying many of the Ni and Si core lines from the Ni/Si sample obtained at various intervals during silicide formation. These spectra illustrate the progression from bulk Si to bulk silicide. In 6(a) only pure Si is present. The signal at 686 eV is from a fluorine residue from the HF/ethanol etch that was used to remove the SiO_2 from the sample surface. This residue desorbs when the sample is heated. As the heating continues, the Ni eventually comes within the information depth of the spectroscopy and the first Ni 2p signal becomes detectable as shown in 6 (b). The increase in the background at high binding energies is due to the large number of scattered electrons from Ni. In 6(c) through 7(a) and 7(b), the progression to the nickel silicide is indicated by the continuous increase in the Ni signals and concurrent decrease in the Si signals.

In Figure 8, the progression of the Ni $2p_{3/2}$ line may be examined in more detail. The first Ni signal appears at a binding energy of 853.7 eV. As the heating continues, a shoulder appears on the low binding energy side at 853.0 eV and grows in intensity until it dominates completely. The corresponding Si 2p spectra show only a slight shift, $\sim$0.2 eV, toward lower binding energy when the

Ni first appears. The Si 2p signal then decreases in intensity while maintaining an essentially constant binding energy. The advancing silicide front was identified as Ni_2Si from the $^4He^+$ backscattering spectra in Figure 9. 9(a) is the spectra obtained before heating, while 9(b) was obtained when the first Si 2p photoemission signal was detected. Figure 9(c) is representative of the spectra obtained after no further changes in the intensities of the Ni and Si photoemission lines could be detected.

The fact that the first Ni signal appears at a higher binding energy than the bulk Ni_2Si suggests that the nickel in the interfacial region is in a more Si rich coordination environment than Ni in Ni_2Si. This agrees with what one would expect intuitively. This peak at 853.7 eV dominates up to 8(d) and perhaps may be due to those Ni atoms that have diffused into the Si ahead of the silicide front.

Of course, detailed interpretation of the chemical shifts observed for the Ni/Si and Si/Ni samples is not possible at this time. Factors such as doping of the Si by the Ni atoms and final state relaxation affects need to be considered.

Valence Structure

The evolution of the valence electronic structure can be followed in exactly the same fashion as the various core levels were followed above. The progression of the valence bands as the thin film evolve from Ni to Ni_2Si and from Si to Ni_2Si are displayed in Figures 10 and 11, respectively. Notice in Figure 10 that as one gradually progresses from pure Ni to bulk Ni_2Si, the density of states at the Fermi level decreases. The 3d band begins in Ni with its upper edge above the Fermi level and gradually shifts to higher binding energies as the Ni_2Si develops. There are also substantial changes in the shape of the d band as the film progresses from Ni to Ni_2Si, as well as the loss of the small peak at $\sim$6 eV.

The origin of the small peak at 6 eV has been a subject of controversy in the literature. This peak (as well as the small peak 6 eV upfield of the other Ni core lines) has been attributed to various many electron effects in the final state. Some of the detailed explanations of these structures have

suggested multiplet splitting[18] and shake-up structure.[19] It has recently been proposed that this additional structure is the result of a 3d hole created during photoemission of a core electron.[20] If the scattered d electron is from the same ion as the core electron, it will produce a two hole final state which is lower in energy than the one hole final state by ∿6 eV. This explanation predicts that the satellite intensity should therefore be related to the density of states at the Fermi level. This is exactly what we observe experimentally in Figure 10. In addition, the exact energy of the two hole state should depend on the multiplet coupling between the 3d shell and core hole. Since the multipet coupling is effected by chemical bonding[18], this may also explain the apparent shift in the satellite position in Figure 4.

In Figure 11, the evolution of the valence structure as the Ni_2Si/Si interface advances toward the surface is shown. Here the density of states at the Fermi level decreases as the film progresses from pure Si to Ni_2Si. Work in the future will be directed toward understanding the variations observed in the valence band spectra in terms of d level occupation and splittings. A systematic variation of the transition metal should aid interpretation and provide insight into the evolution of valence electronic structure as one progresses from a semiconductor to a metal.

Impurity Effects in Thin Films

The in situ monitoring of the advancing planar silicide front as described earlier may be particularly suited for an investigation of impurity effects in thin film reactions. Auger studies[21] and $^4He^+$ backscattering studies[22] have shown that oxygen impurities introduced into thin metal films on silicon, either accidently during deposition or by ion implantation, can change the growth kinetics of the silicide formation. These experiments have shown that the advancing silicide reaction front sweeps the oxygen into the metal until a diffusion barrier is formed. When this occurs, the silicide formation stops, leaving a layer of unreacted metal on the surface.

Very little is known about the nature of this diffusion barrier that is created as a result of rejected oxygen impurities. The initial in situ silicide formation experiments using XPS/AES already described suggest that this

experimental approach may yield information concerning the chemical nature of the barrier by monitoring photoemission from the impurity atoms as well as the Ni and Si atoms. Figure 12 plots the oxygen 1s photoemission lines obtained at various stages during silicide formation for the Si/Ni sample. 12(a) shows the oxygen detected before any silicide formation. This oxygen is due to the small amount of NiO remaining of the surface after the HCl/ethanol etch as well as the oxygen impurities in the Ni film. As the Si/Ni sample is heated and the silicide/Ni interface advances toward the Ni surface, the O 1s signal is found to gradually increase. Figure 12(b) shows the O 1s obtained when the interface is $\sim$50 Å from the Ni surface, while 12(c) was obtained after the reaction had completely consumed the Ni. By the end of the reaction, the oxygen signal has increased by a factor of four. The Si 2p photoemission signals corresponding to these oxygen 1s signals are shown in Figure 13. There is no observable silicon in 13(a), as expected. 13(b) and 13(c) show the development of a small peak $\sim$3 eV upfield of the main Si 2p peak at 99 eV. This small peak gradually increases in intensity as the silicide front advances and appears to correlate with the increase in the O 1s peak. This peak, which is too low in binding energy to be due to SiO_2 (Si^{+4}), falls approximately where one expects a Si^{+2} subcxide signal to occur. There is no observable development of Ni oxide.

The same behavior of the oxygen and silicon photoemission lines are observed in the Ni/Si sample. The O 1s increases in intensity with the concurrent development of a silicon suboxide peak, shown in Figure 14, as the silicide/silicon interface advances toward the silicon surface.

These experiments suggest that the formation of the diffusion barrier from the oxygen swept forward by the advancing silicide front is related to the formation of silicon suboxides. Since the energy required to break a Si-O bond is $\sim$192 kcal while a Si-Si bond requires only $\sim$76 kcal, a boundary of silicon suboxides could prevent the forward diffusion of the Ni atoms by blocking the interstitial bond breaking mechanism that has been proposed for low temperature silicide formation.[23] No evidence is found for the involvement of Ni in the barrier. Further experiments are necessary to eliminate the possibility that the increase in the O 1s and the Si suboxide are due to residual oxygen in the XPS analysis chamber. This can be accomplished by ion implanting various

concentrations of oxygen into the Ni and Si films. If the increase in the oxygen and Si suboxide species is due to oxygen being rejected by the advancing silicide front, then the photoemission intensities will correlate with the oxygen implantation dosages. This work will be done in collaboration with D. Scott.

The carbon 1s photoemission intensity was also found to increase in intensity as the silicide front advanced. It would appear that the general phenomenon of impurity rejection by silicides lends itself well to in situ studies with XPS. This experimental approach should be particularly useful in establishing the chemical roles of not only carbon and oxygen but dopant impurities as well in the control of thin film properties.

SUMMARY

The current understanding of the bonding within the silicides is very primative despite increasing numbers of theoretical and experimental studies that emphasize the need for additional chemical bond information for these systems. In this chapter, a systematic investigation has been proposed to examine the bonding properties of selected transition metal silicides on single crystal silicon substrates. The study will initially concentrate on the silicides formed with the Group VIII (Ni, Pd, Pt) and the Group IV (Ti, Zr, Hf) transition metals.

The investigation will utilize three complementary spectroscopic techniques to fully characterize the silicide structures. $^{4}He^{+}$ backscattering will be used to follow the progression of the thin film reactions and to provide quantitative information on atomic composition. XPS and x-ray excited AES will be used to obtain chemical bonding information. The core and valence electron levels will be examined as well as both the metal and silicon derived Auger valence transitions.

In addition to characterization of the bulk silicides, the interfacial bonding properties will be examined as well. Two fundamentally different approaches to the study of the Si/silicide and metal/silicide interfaces are proposed. One approach follows the development of the interface using thin

metal depositions on Si substrates. This may be used to study the "as deposited" metal/Si interface as well as the reacted silicide/Si interface. The second approach examines the advancing planar silicide front by dynamically monitoring the *in situ* formation of the silicides. This approach is procedurally simple and allows examination of the interface with an extended solid on either side.

Initial experiments were presented to demonstrate the feasibility of monitoring the advancing interfacial regions with the second approach described above. The Si/Ni_2Si interface as well as the Ni/Ni_2Si interface was examined. Significant shifts in the core binding energies of Si and Ni were observed as the reaction front approached the surface. The evolution of the valence electron structure was also monitored. Changes in the shape of the d band, the satellite structure, and density of states at the Fermi level were observed. The detailed interpretation of this data is not possible at this time. The key to interpretation is to examine a variety of silicides with a systematic variation of the transition metal. Trends and correlations in the bulk and interfacial bonding characteristics may be identified in this fashion.

The initial experiments also suggest that the *in situ* monitoring of the advancing silicide front may provide information concerning the effect of of impurities in thin film reactions of metal on silicon. The results suggest that Si-O bonding is involved in the formation of a growth barrier for the case of oxygen impurities.

REFERENCES

1. Rowe, J. E., Margaritondo, G., Christman, S. B., Phys. Rev. B., 15 (1977) 2195

2. Margaritondo, G., Rowe, J. E., Christman, S.B., Phys. Rev. B, 14 (1976), 5396

3. Andrews, J. M., Phillips, J.C., Phys. Rev. Lett., 35 (1975) 56

4. Roth, J. A., Thesis, University of Southern California, Materials Science Dept.

5. Gregory, P.E., Spicer, W.E., Phys. Rev., B12 (1975) 2370

6. Eastman, D.E., Freeouf, J.C., Phys. Rev. Lett., 35 (1976) 1471

7. Margaritondo, G., Christman, S.B., Rowe, J.E., J. Vac. Sci. Technol., 13 (1976) 329

8. Chu, W., Mayer, J.W., Nicolet, M-A., Backscattering Spectrometry, (Academic Press, New York) 1978

9. Cardona, M., Ley, L., ed., Topics in Applied Physics, Vol. 26 "Photoemission in Solids, I", (Springer-Verlag, New York) 1978

10. Chang, C.C., in "Characterization of Solid Surfaces," ed. by Kane, P.F., Larrabee, G.B., (Plenum Press, New York) 1974

11. Thomas, S., Terry, L.E., Appl. Phys. Lett., 26 (1975) 433

12. Thomas, S., Terry, L.E., J. Appl. Phys., 47 (1976) 301

13. Mele, E.J., Joannopoulos, J.D., J. Vac. Sci. Technol., 15 (1978) 1370

14. Tu, K.N., Alessandrini, Chu, W.K., Kräutle, H., Mayer, J.W., Jap. J. Appl. Phys. Suppl. 2, Pt. 1, 669 (1974)

15. Feldman, L., Silverman, P.J., Stensgaard, I., J. Vac. Sci. Technol., 16 (1979) ØØØØ

16. Poate, J.M., Tu, K.N., Mayer, J.W., editors in "Thin Films — Interdiffusion and Reactions," (John Wiley and Sons) 1978, p. 359

17. Hutchins, G.A., Shepela, A., Thin Solid Films, 18 (1973) 343

18. Fadley, C.S., Shirley, D.A., Phys. Rev. A, 2 (1970) 1109

19. Andrews, P.T., Collins, T., Johnson, C.E., Weightman, P.J., Electron. Spect. 15, (1979) 39

20. Hüfner, S., Wertheim, G.K., Phys. Lett., 51A (1975) 299

21. Bindell, J.B., Colby, J.W., Wonsidler, D.R., Poate, J.M., Conley, D.K. Tisone, T.C., Thin Solid Films, 37 (1976) 441

22. Scott, D., Tsaur, B.Y., Nicolet, M-A,, Mayer, J.W., to be published

23. Tu, K.N., Appl. Phys. Lett., 27 (1975) 221

FIGURE CAPTIONS

Figure 1. Illustration of the progression of the silicide phases.

Figure 2. The top spectrum is obtained from a Ni film with a NiO overlayer. The lower curve is obtained after etching with HCl/ethanol.

Figure 3. Si 2p spectra obtained as the Ni_2Si/Ni interface approaches the surface.

Figure 4. Ni $2p_{3/2}$ spectra corresponding to the Si spectra in figure 3.

Figure 5. The $^4He^+$ backscattering spectra obtained after no further changes in the Ni and Si signals could be detected with XPS.

Figures 6 and 7. Illustration of the progression of the various core levels of Ni and Si as the Ni_2Si/Si interface approaches the surface.

Figure 8. Ni $2p_{3/2}$ spectra obtained as the Ni_2Si/Si interface approached the surface.

Figure 9. The $^4He^+$ backscatting spectra obtained at various stages during the growth of Ni_2Si. The top curve is from the virgin sample. The middle curve was obtained when the first Ni signal was detected with XPS. The lower curve was obtained when no further changes in the Ni or Si XPS signal could be detected.

Figure 10. The evolution of the valence spectra as the Ni_2Si/Ni interface approaches the surface.

Figure 11. The evolution of the valence spectra as the Ni_2Si/Si interface approaches the surface.

Figure 12. The O 1s spectra obtained at various stages as the Ni_2Si/Ni interface approached the surface.

Figure 13. The Si 2p spectra obtained at the same stage in the silicide formation as the O 1s spectra in figure 12.

Figure 14. The Si 2p spectra obtained at various stages as the Ni_2Si/Si interface approached the surface.

Figure 1

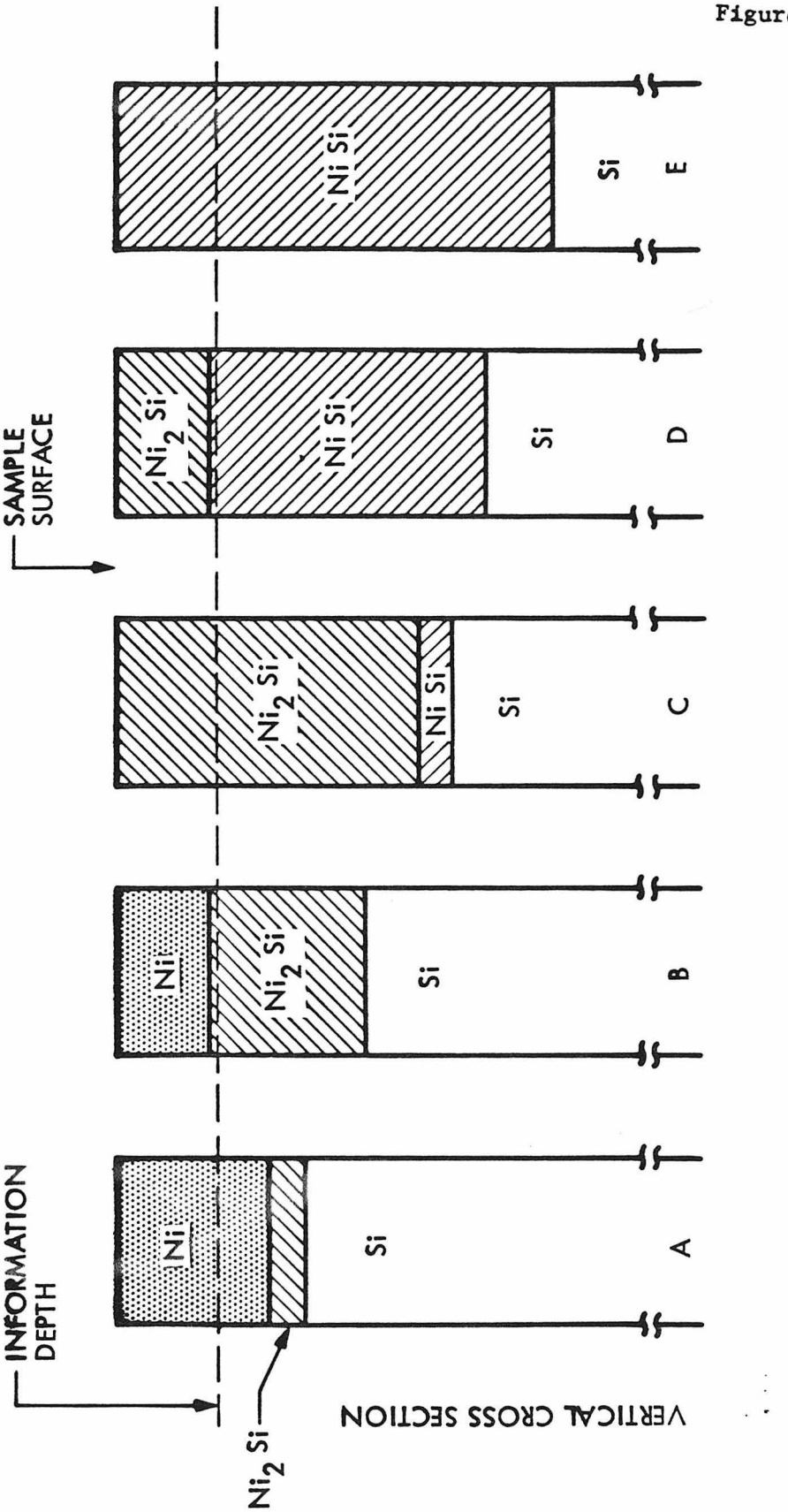
VERTICAL CROSS SECTION
INFORMATION DEPTH
SAMPLE SURFACE
Ni
Si
A
Ni
Ni2 Si
Si
B
Ni2 Si
Ni Si
Si
C
Ni2 Si
Ni Si
Ni Si
Si
D
Ni Si
Si
E
Ni2 Si

Figure 2

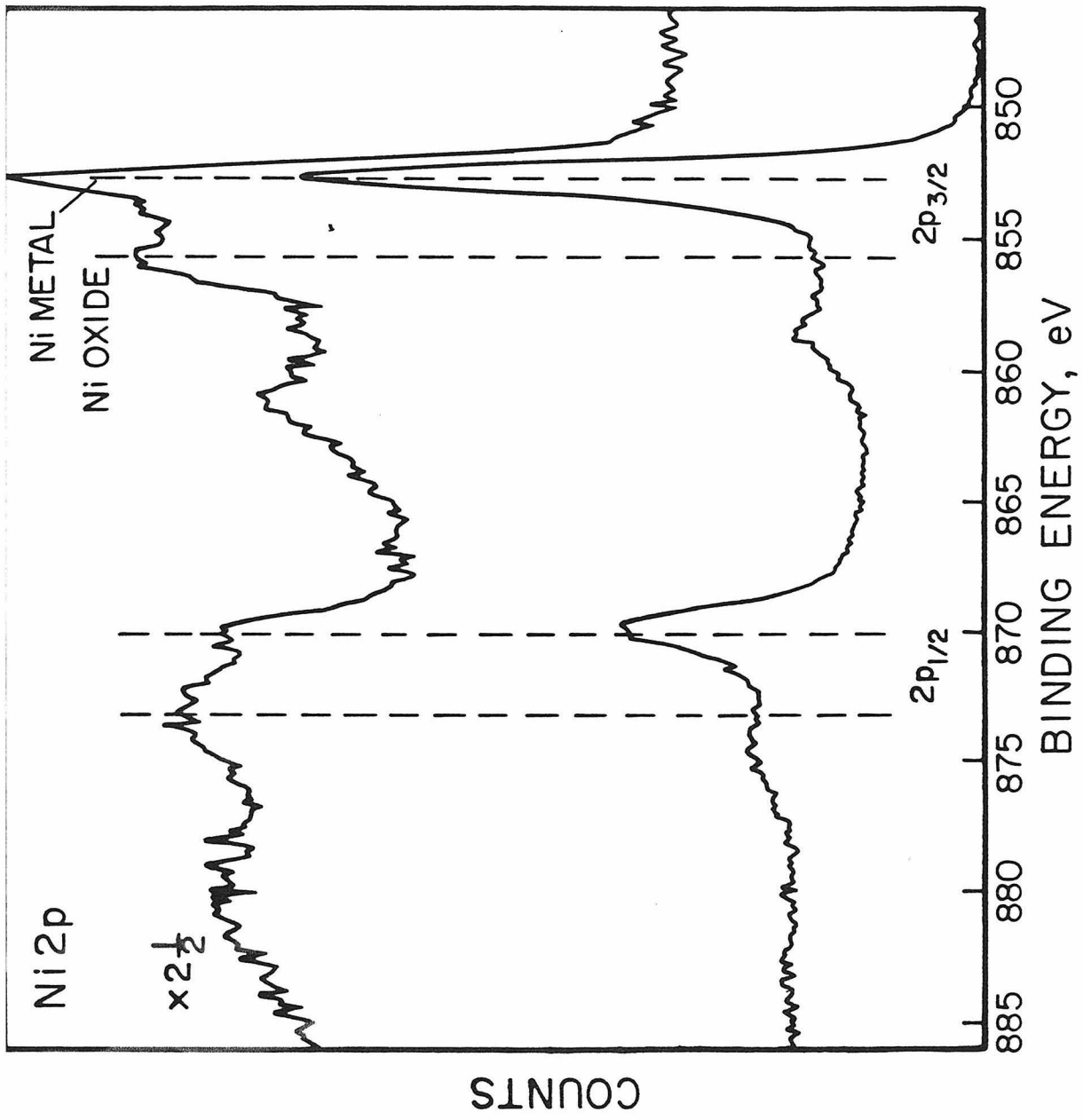
Ni 2p
x2½
Ni METAL
Ni OXIDE
$2p_{3/2}$
$2p_{1/2}$
885
880
875
870
865
860
855
850
BINDING ENERGY, eV
COUNTS

Figure 3

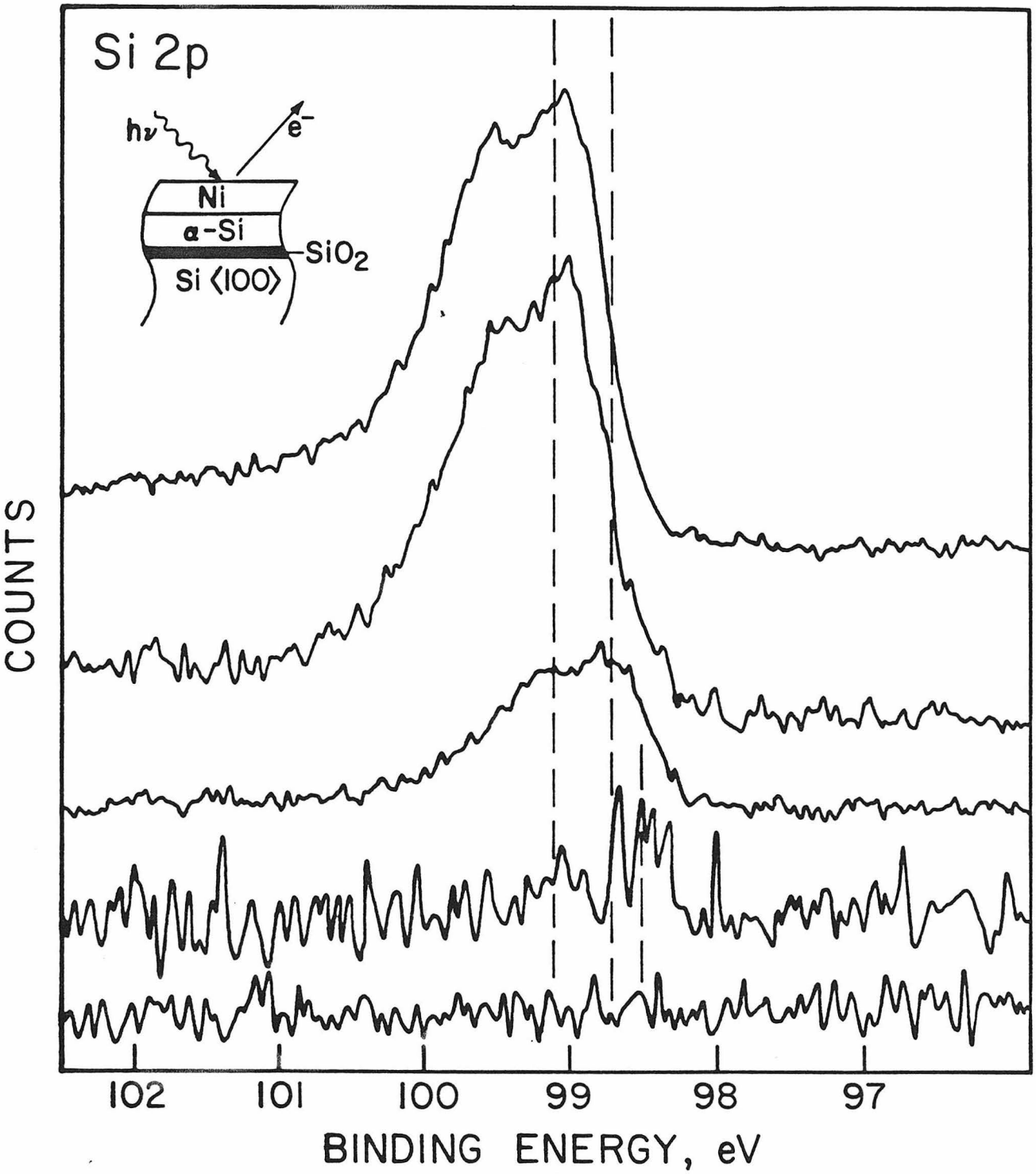
Si 2p
hν
e⁻
Ni
α-Si
SiO2
Si ⟨100⟩
COUNTS
102
101
100
99
98
97
BINDING ENERGY, eV

Figure 4

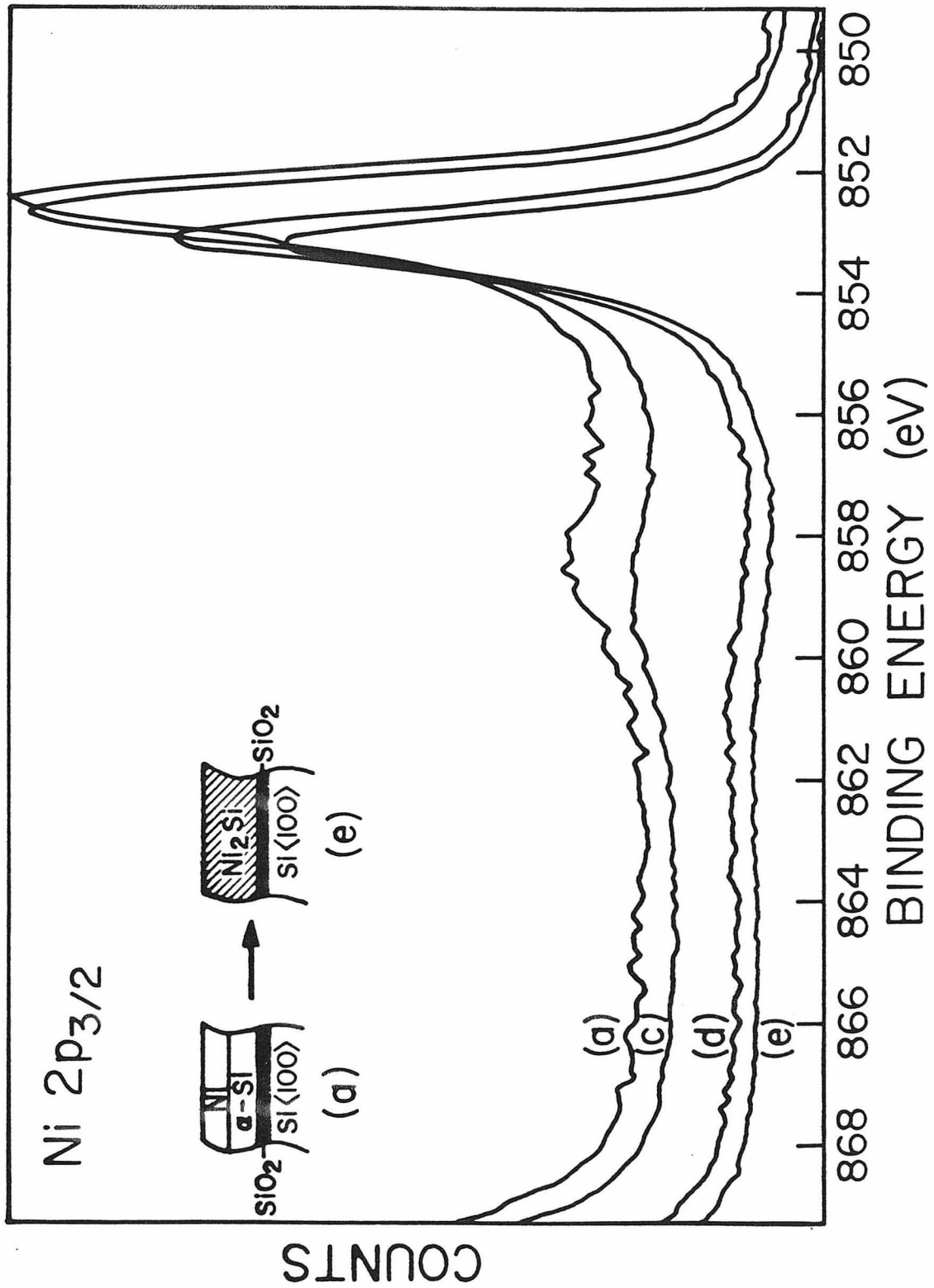
Ni 2p3/2
SiO2
Ni
a-Si
Si⟨100⟩
(a)
Ni2Si
SiO2
Si⟨100⟩
(e)
(a)
(c)
(d)
(e)
COUNTS
868 866 864 862 860 858 856 854 852 850
BINDING ENERGY (eV)

Figure 5

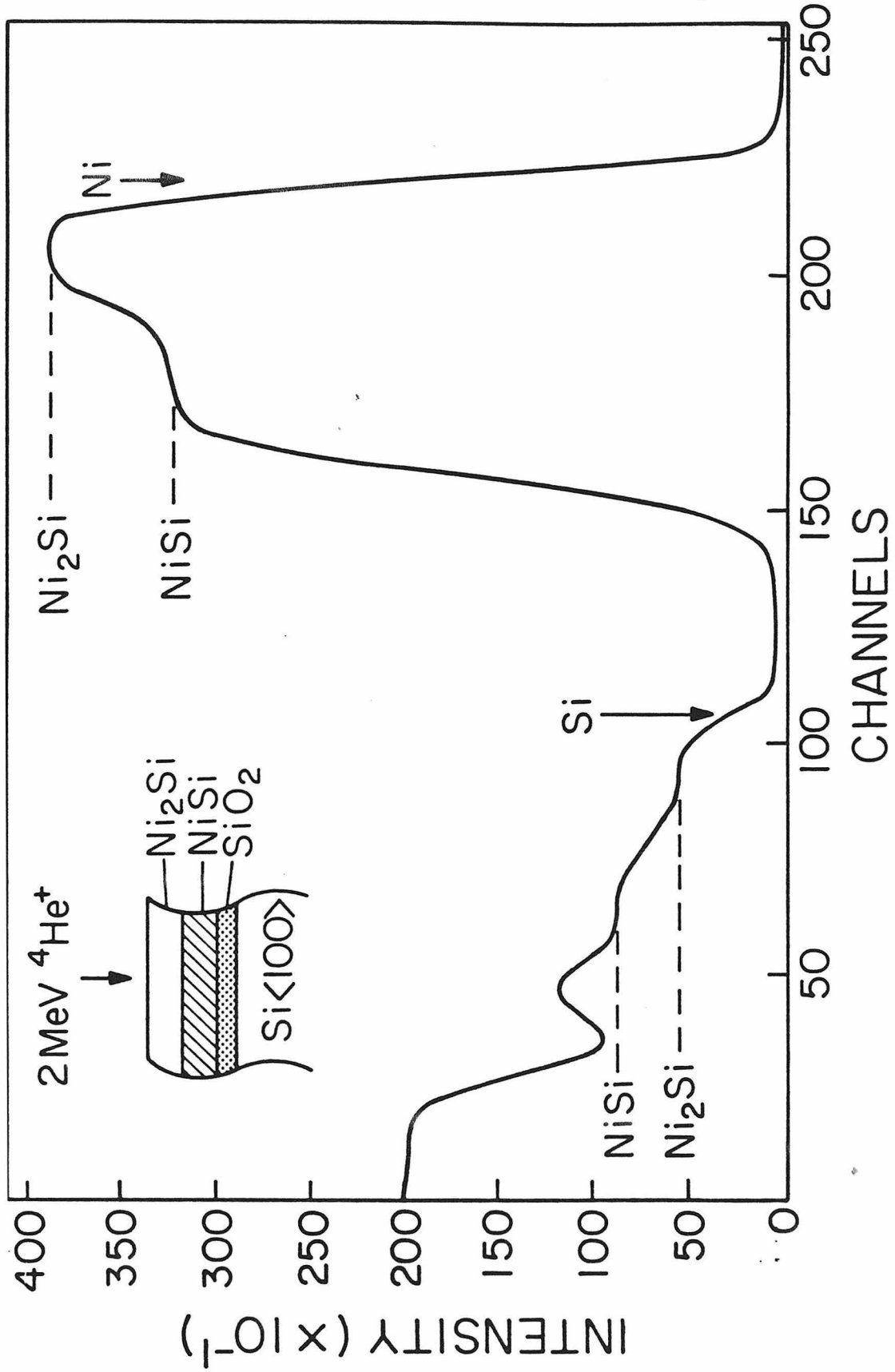
INTENSITY (x 10⁻¹)
CHANNELS
Ni
Ni₂Si
NiSi
Si
NiSi
Ni₂Si
2MeV ⁴He⁺
Ni₂Si
NiSi
SiO₂
Si<100>

Figure 6

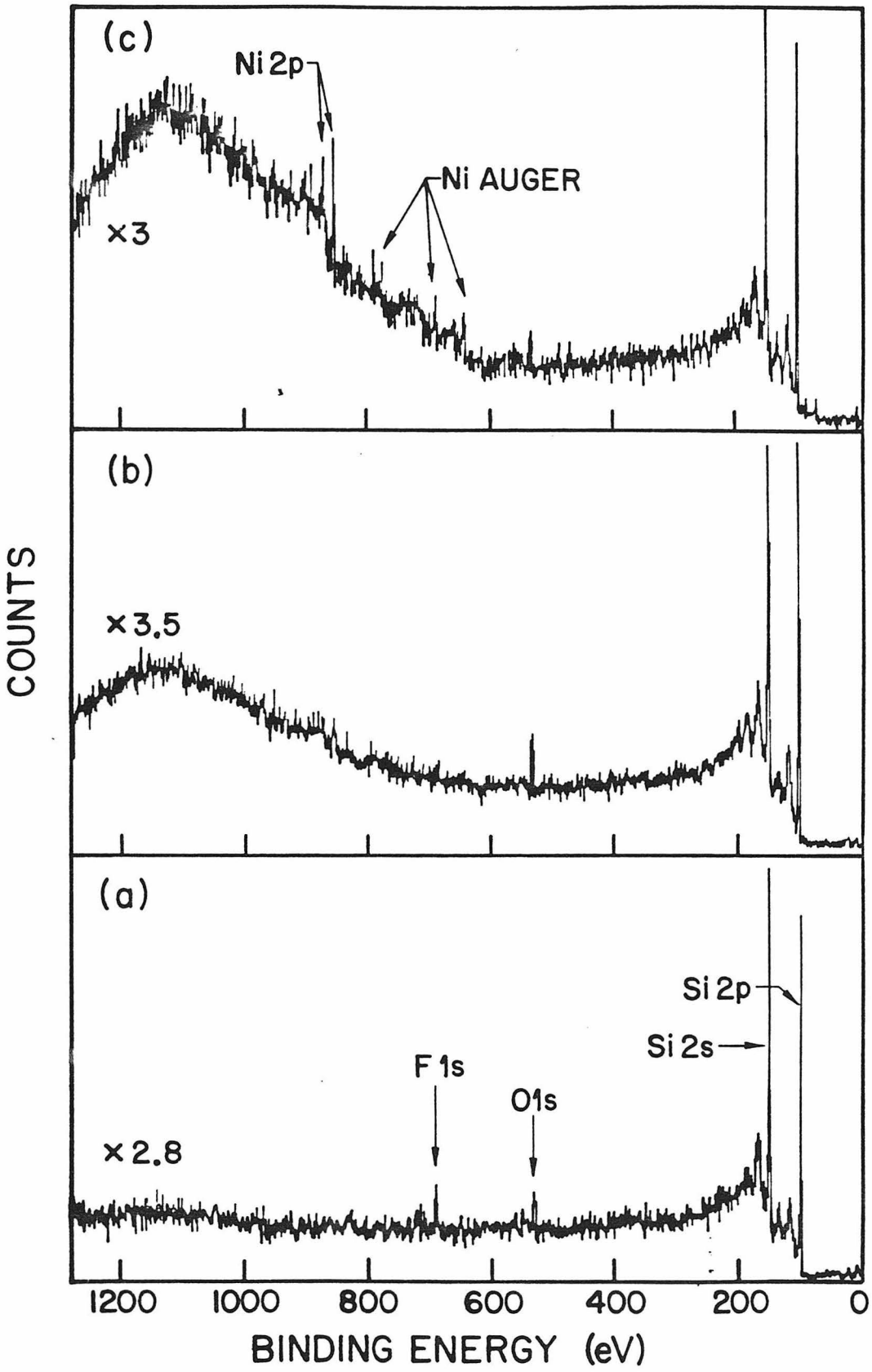
(c)
Ni 2p
Ni AUGER
×3
(b)
×3.5
(a)
Si 2p
Si 2s
F 1s
O1s
×2.8
COUNTS
1200
1000
800
600
400
200
0
BINDING ENERGY (eV)

Figure 7

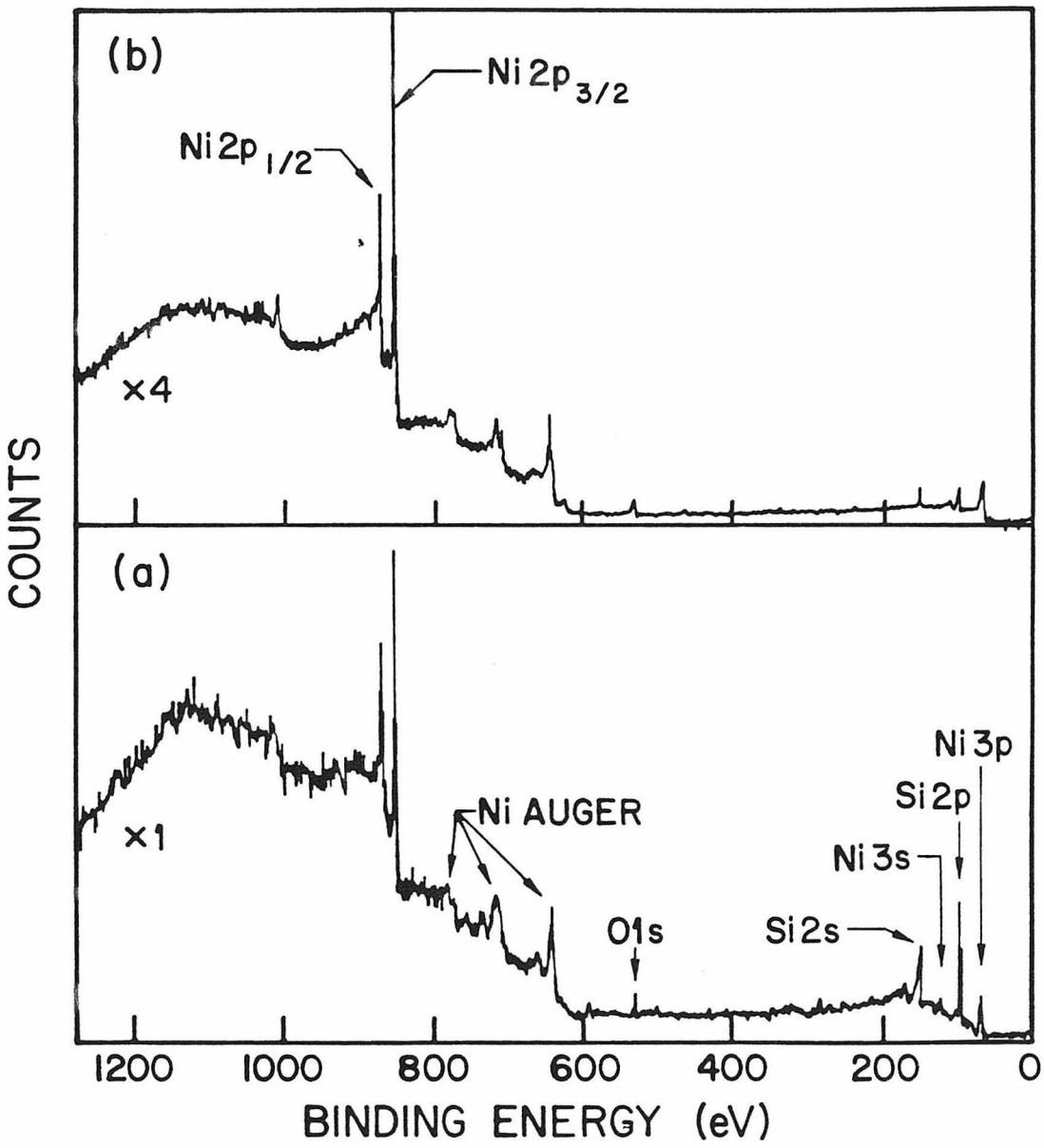
(b)
Ni 2p 3/2
Ni 2p 1/2
×4
(a)
×1
Ni AUGER
O1s
Si 2s
Ni 3s
Si 2p
Ni 3p
COUNTS
1200
1000
800
600
400
200
0
BINDING ENERGY (eV)

Figure 8

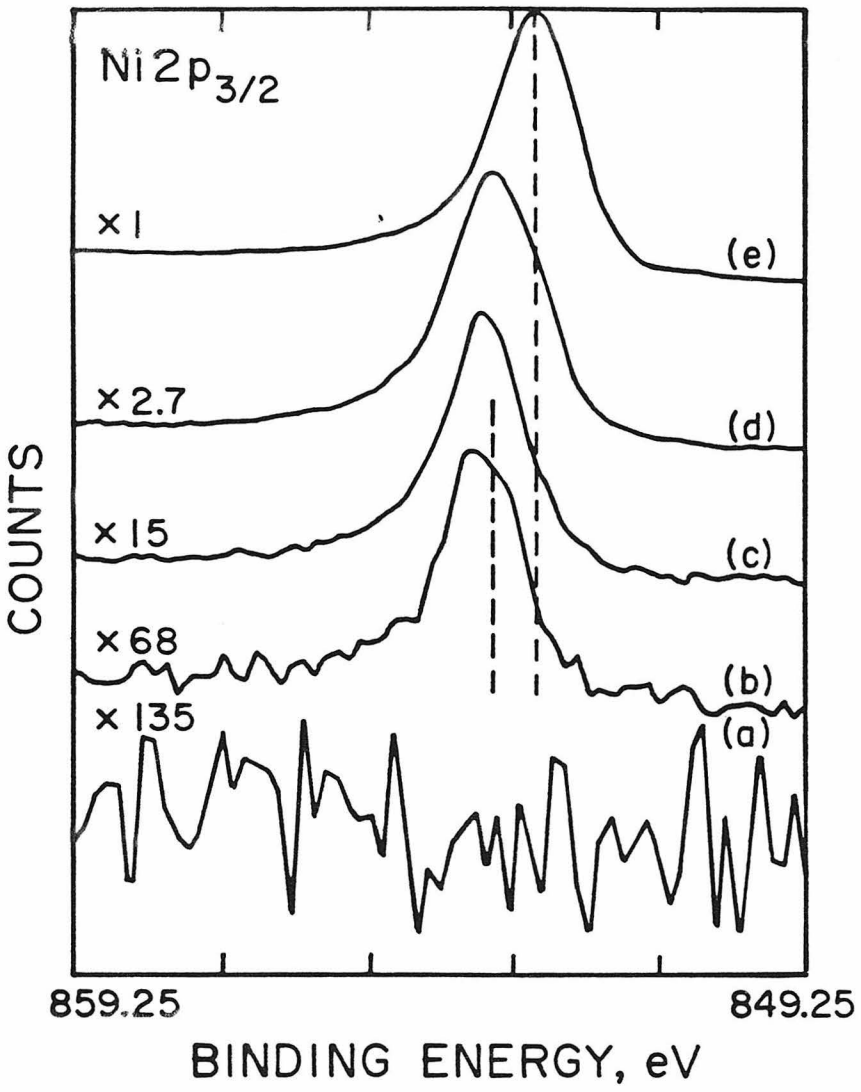
Ni 2p3/2
×1
(e)
×2.7
(d)
×15
(c)
×68
(b)
×135
(a)
COUNTS
859.25
849.25
BINDING ENERGY, eV

Figure 9

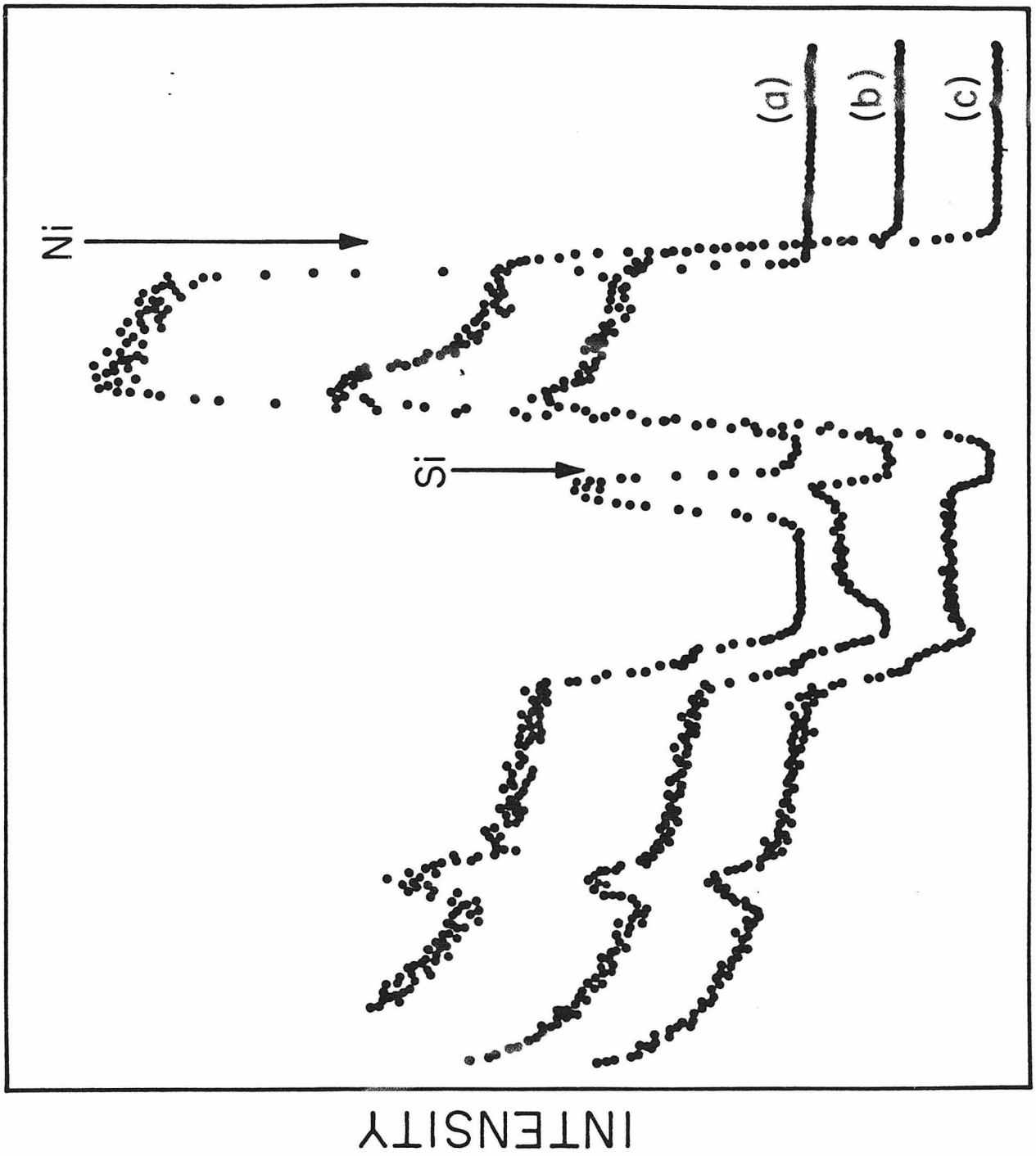

Figure 10

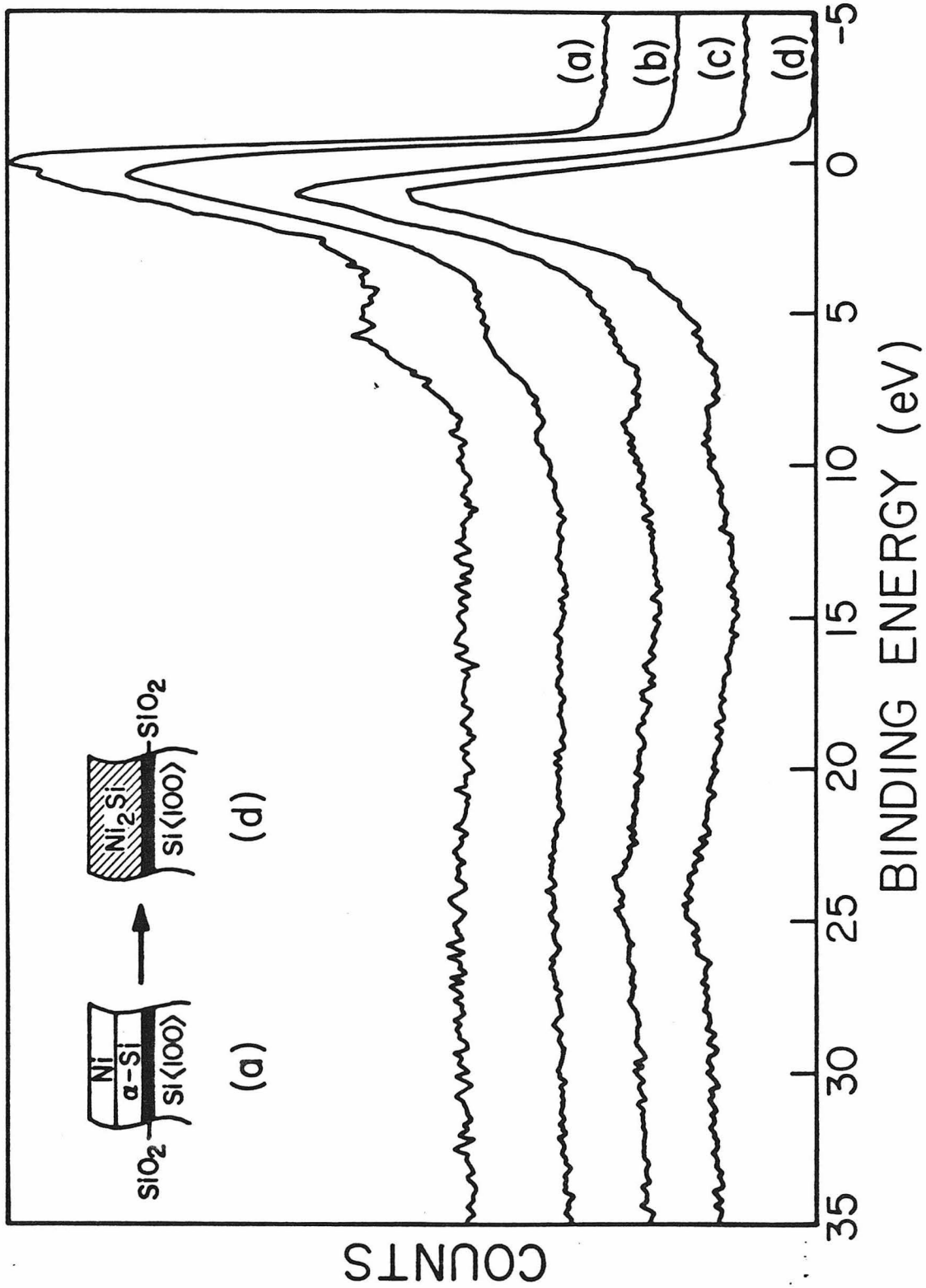
COUNTS
BINDING ENERGY (eV)
-5
0
5
10
15
20
25
30
35
(a)
(b)
(c)
(d)
Ni
a-Si
Si⟨100⟩
SiO2
(a)
Ni2Si
Si⟨100⟩
SiO2
(d)

Figure 11

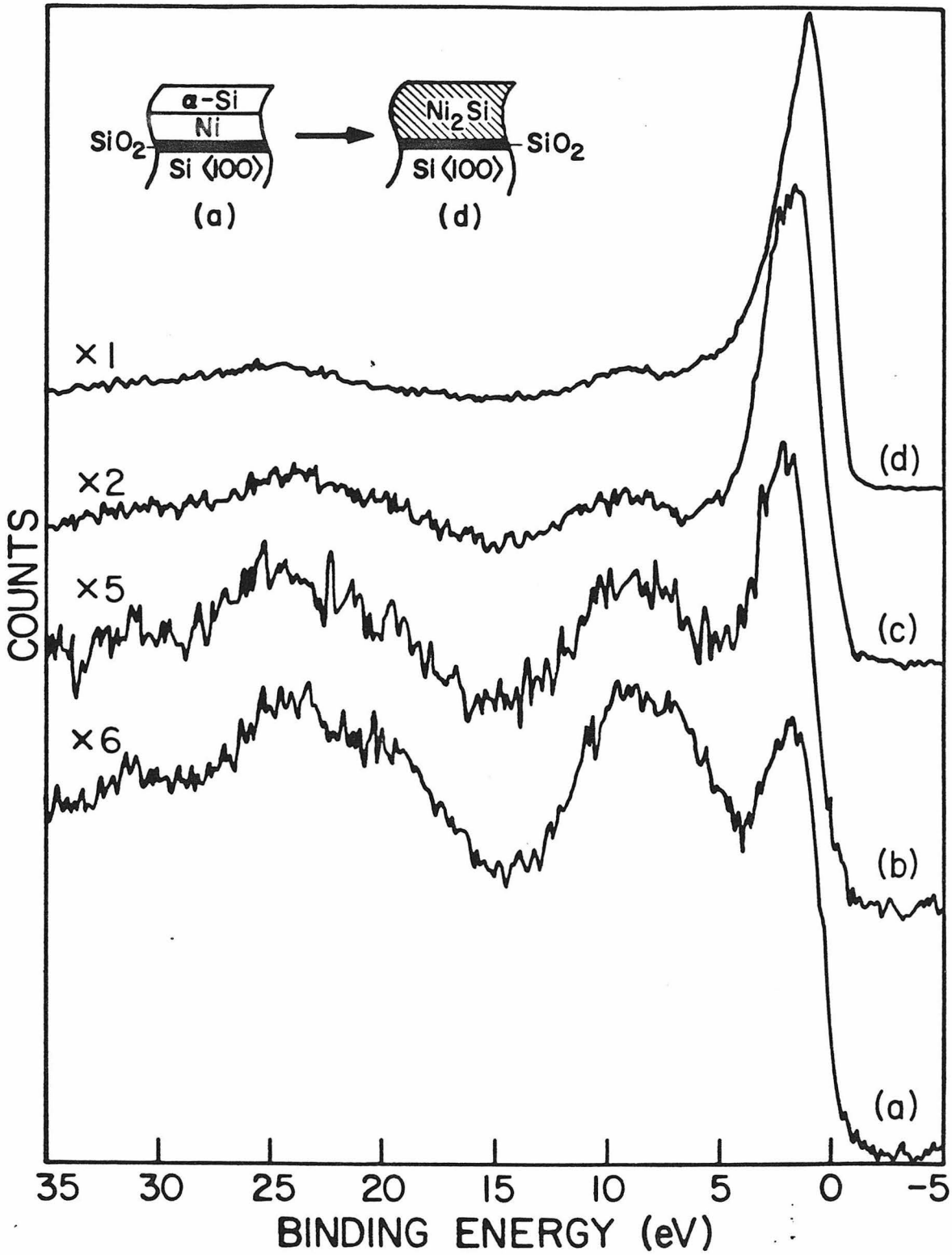
a-Si
Ni
SiO2
Si ⟨100⟩
(a)
Ni2Si
SiO2
Si ⟨100⟩
(d)
×1
×2
×5
×6
(d)
(c)
(b)
(a)
COUNTS
35
30
25
20
15
10
5
0
-5
BINDING ENERGY (eV)

Figure 12

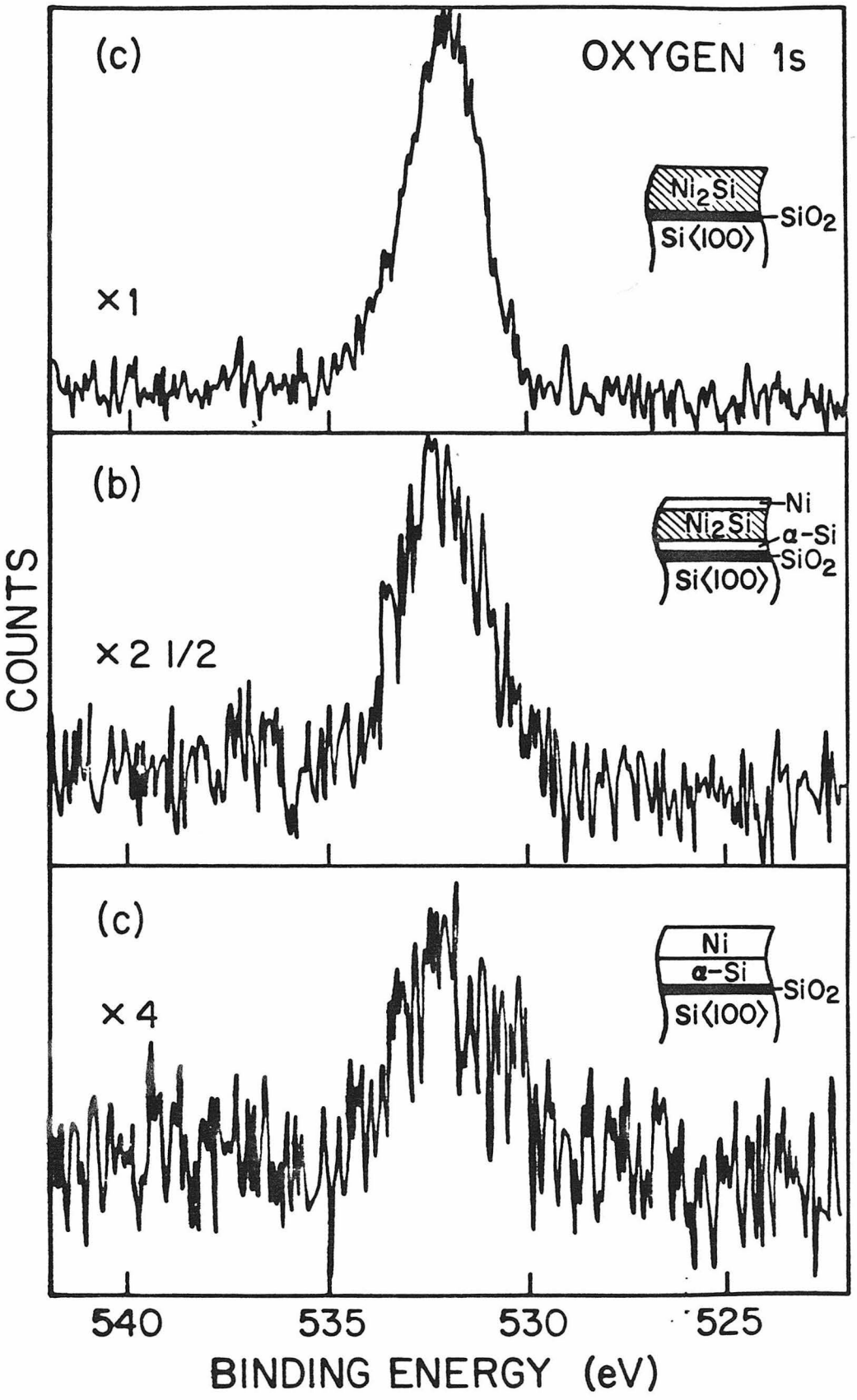
(c)
OXYGEN 1s
Ni2Si
SiO2
Si⟨100⟩
×1
(b)
Ni
Ni2Si
α-Si
SiO2
Si⟨100⟩
×2 1/2
(c)
Ni
α-Si
SiO2
Si⟨100⟩
×4
COUNTS
540
535
530
525
BINDING ENERGY (eV)

Figure 13

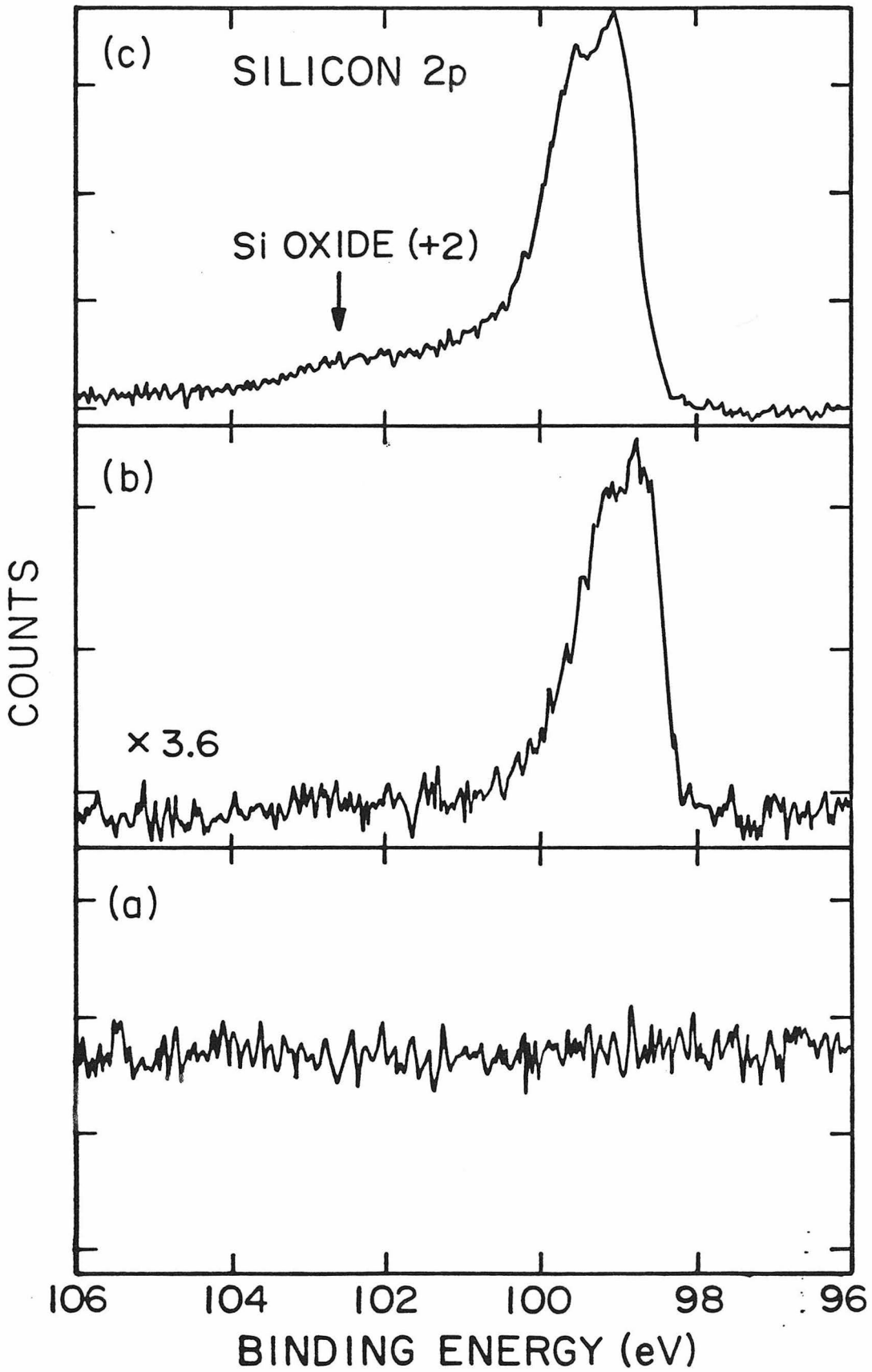
(c)
SILICON 2p
Si OXIDE (+2)
(b)
× 3.6
(a)
COUNTS
106
104
102
100
98
96
BINDING ENERGY (eV)

Figure 14

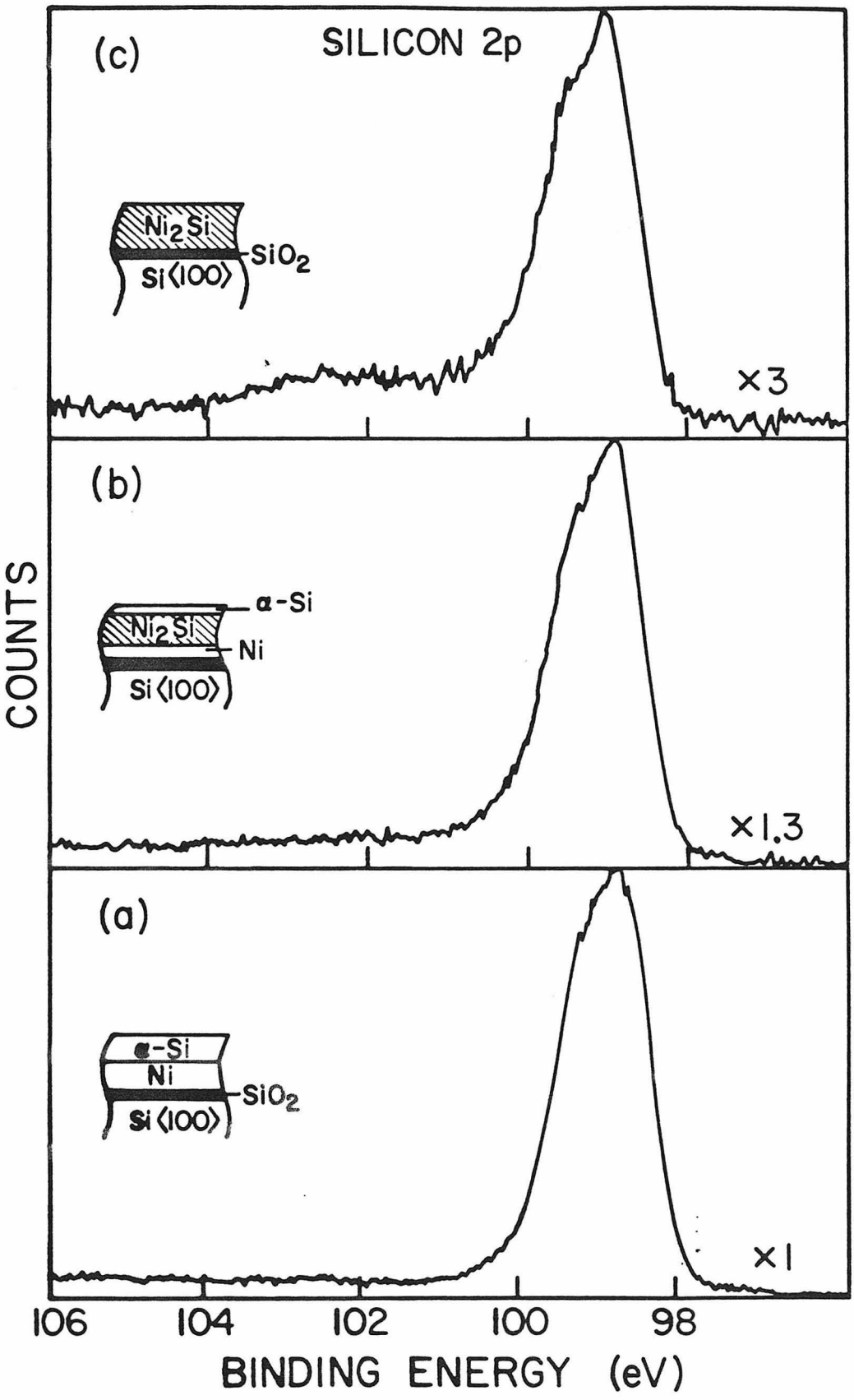
(c)
SILICON 2p
Ni2Si
SiO2
Si⟨100⟩
×3
(b)
α-Si
Ni2Si
Ni
Si⟨100⟩
×1.3
(a)
α-Si
Ni
SiO2
Si⟨100⟩
×1
COUNTS
106
104
102
100
98
BINDING ENERGY (eV)